



Norwegian University of  
Science and Technology

# Ultrafast Optical and Magneto-Optical Kerr Effect Spectroscopy on Condensed Matter

**Erik Nikolai Lysne**

Master of Science in Electronics

Submission date: September 2017

Supervisor: Ulf Lennart Østerberg, IES

Norwegian University of Science and Technology  
Department of Electronic Systems



---

---

---

---

---

# Summary

In this masters project, an ultrafast optical spectroscopy system has been constructed and tested. The system was built as an extension to an existing spectroscopy system, centered around a mode-locked Ti:Sapphire femtosecond laser, optically amplified by a Q-switched, frequency-doubled Nd:YLF laser. The previous system was based on principles of nonlinear optics, and was used to measure third-order nonlinear effects. The goal of the project was to create a system that could perform measurements of magnetic and third-order nonlinear properties in condensed matter. The work led to improvements in detection and signal analysis, and inclusion of magneto-optical measurements based on the longitudinal magneto-optical Kerr effect. The functionality of the system was experimentally verified through measurements on permalloy ( $\text{Ni}_{0.8}\text{Fe}_{0.2}$ ) grown on fused silica ( $\text{SiO}_2$ ), optically coated with zirconium dioxide ( $\text{ZrO}_2$ ). Optical demagnetization was also tested, and the demagnetization and recovery transients were resolved in time, using ultrafast optical measurement techniques. This proved to be feasible with the current system. Further work is however required to gain a detailed analysis of the time-resolved measurements.

The ultrafast nonlinear optical capabilities were also tested through measurements on deionized water ( $\text{H}_2\text{O}$ ) and acetone ( $(\text{CH}_3)_2\text{CO}$ ). Several samples with films of iron-doped zinc sulfide ( $\text{Fe:ZnS}$ ) on sapphire ( $\text{Al}_2\text{O}_3$ ) substrate were characterized, on request from another group of researchers. The third-order nonlinear susceptibility was calculated based on these measurements, and was found to conform well with values obtained by others. The Raman spectrum of water was also calculated based on nonlinear measurements, to test the possibility of retrieving spectral information from the time-resolved measurements. The bandwidth of the laser was 14 THz, and it is believed that spectral features as high as 12 THz could be resolved in the analysis of the Raman spectrum.

---

# Sammendrag

I dette masterprosjektet har et ultraraskt spektroskopisystem blitt konstruert og testet. Systemet ble bygget som en utvidelse til et eksisterende spektroskopisystem, sentrert rundt en mode-låst Ti:Sapphire femtosekund laser, optisk forsterket av en Q-svitsjet, frekvensdoblet Nd:YLF laser. Det tidligere konstruerte systemet var basert på prinsipper fra ikkelineær optikk, og ble brukt til å måle tredjeordens ikkelineære effekter. Målet med prosjektet var å lage et system som kunne utføre målinger av magnetiske og tredjeordens ikkelineære egenskaper i kondensert materie. Dette arbeidet førte til forbedringer innen deteksjon og signalanalyse, og inkludering av magneto-optiske målinger basert på longitudinell magneto-optisk Kerr effekt. Funksjonaliteten til systemet ble testet eksperimentelt, ved målinger på permalloy ( $\text{Ni}_{0.8}\text{Fe}_{0.2}$ ) grodd på substrat av kvarts ( $\text{SiO}_2$ ), belagt med zirkonium dioksid ( $\text{ZrO}_2$ ). Optisk demagnetisering ble også testet og demagnetisering og gjenoppretting av magnetismen ble målt i tid, ved hjelp av ultrarask optiske målemetoder. Dette viste seg å være gjennomførbart med det nåværende systemet. Videre arbeid er derimot nødvendig for å oppnå en detaljert analyse av tidsmålingene.

De ultrarask, ikkelineære måleegenskapene ble også testet, ved målinger gjort på deionisert vann ( $\text{H}_2\text{O}$ ) og aceton ( $(\text{CH}_3)_2\text{CO}$ ). Flere prøver med filmer av jerdopet sink sulfid ( $\text{Fe:ZnS}$ ) på safir ( $\text{Al}_2\text{O}_3$ ) substrat ble karakterisert, etter ønske fra en annen forskningsgruppe. Den tredjeordens ikkelineære susceptibiliteten ble beregnet ut ifra disse målingene, og ble funnet til å stemme overens med tidligere målinger gjort av andre. Basert på ikkelineære målinger ble også Ramanspekteret til vann beregnet, for å teste muligheten for å utvinne spektralinformasjon fra tidsmålinger. Båndbredden til laseren var målt til 14 THz, og det er antatt at spektralegenskaper så høyt som 12 THz kunne hentes ut fra Ramanspekteret.

---

# Preface

This masters project has been carried out in the Ultrafast Optics Laboratory at the Norwegian University of Science and Technology (NTNU) in the year 2017. In the past year, I have been given the opportunity to study advanced topics in photonics, and work on scientific research that is state-of-the-art. For this, I am truly grateful. I would like to extend my most sincere thanks to my supervisor Prof. Ulf Österberg, who has made this journey inspiring and fun, and whose knowledge has been my most important resource. I would also like to thank Prof. Ursula Gibson for providing unique assistance and insight, and for granting me access to her laboratory. I would like to thank Prof. Thomas Tybell for contributing with his enthusiasm and knowledge, and Dr. Reza Zamiri for teaching me about nonlinear optics. I would also like to thank Kjell Mølster for engaging discussions and for providing great companionship in the laboratory. Lastly, I would like to thank my parents for always being there for me, and my brother Christian for supporting me no matter what.

This thesis has been written in  $\LaTeX$ . All figures without an explicit reference have been created by me, using the packages `TikZ` and `PGF` for  $\LaTeX$ .

# Table of Contents

<b>Summary</b>	<b>i</b>
<b>Summary</b>	<b>i</b>
<b>Preface</b>	<b>ii</b>
<b>Table of Contents</b>	<b>vi</b>
<b>List of Tables</b>	<b>vii</b>
<b>List of Figures</b>	<b>xiv</b>
<b>Abbreviations</b>	<b>xv</b>
<b>1 Introduction</b>	<b>1</b>
1.1 Project Work and Motivation . . . . .	1
1.2 What is Spectroscopy? . . . . .	3
1.3 Outline of the Thesis . . . . .	4
<b>2 Theory</b>	<b>5</b>
2.1 Introduction . . . . .	5
2.2 Electromagnetism . . . . .	6
2.2.1 Introduction . . . . .	6
2.2.2 The Electromagnetic Wave Equation . . . . .	8
2.3 Polarization Optics . . . . .	11
2.3.1 Introduction . . . . .	11
2.3.2 Jones Vectors and Jones Matrices . . . . .	11
2.3.3 Ellipticity . . . . .	13
2.3.4 The Kerr Effects - Overview . . . . .	14
2.4 Linear and Nonlinear Optics . . . . .	15
2.4.1 Introduction . . . . .	15
2.4.2 Linear Optics . . . . .	15



---

2.4.3	Nonlinear Optics . . . . .	17
2.4.4	Second-Order Effects . . . . .	19
2.4.5	Third-Order Effects . . . . .	22
2.4.6	Intensity-Dependent Refractive Index (IDRI) and the Optical Kerr Effect (OKE) . . . . .	24
2.4.7	Nonlinear Optics in the Time-Domain . . . . .	27
2.5	Quantum Mechanics . . . . .	28
2.5.1	Introduction . . . . .	28
2.5.2	Basic Concepts . . . . .	28
2.5.3	The Two-Level System . . . . .	29
2.5.4	Higher-Order Processes . . . . .	32
2.5.5	The Stimulated Raman Effect . . . . .	35
2.6	Magnetism in Materials . . . . .	38
2.6.1	Introduction . . . . .	38
2.6.2	Types of Magnetism . . . . .	39
2.6.3	Domains and Hysteresis . . . . .	40
2.7	Magneto-Optics . . . . .	42
2.7.1	Introduction . . . . .	42
2.7.2	The Magneto-Optical Kerr Effect . . . . .	42
2.7.3	Optical Rotation and Ellipticity of Circularly Polarized Waves . . . . .	43
2.7.4	The Complex Voigt Vector . . . . .	47
2.7.5	Longitudinal MOKE . . . . .	48
2.7.6	Nonlinear Magneto Optics . . . . .	50
<b>3</b>	<b>The OKEMOKE System</b> . . . . .	<b>51</b>
3.1	Overview . . . . .	51
3.1.1	Introduction . . . . .	51
3.1.2	Capabilities of the System . . . . .	51
3.2	Pump-Probe Spectroscopy . . . . .	53
3.2.1	Introduction . . . . .	53
3.2.2	Sampling with THz Resolution . . . . .	53
3.2.3	Signal, Noise and Dynamic Range . . . . .	55
3.3	OKE Spectroscopy . . . . .	57
3.3.1	Introduction . . . . .	57
3.3.2	Measurement . . . . .	57
3.3.3	Analysis of the OKE Signal . . . . .	58
3.3.4	The Third-Order Susceptibility . . . . .	62
3.4	MOKE Spectroscopy . . . . .	63
3.4.1	Introduction . . . . .	63
3.4.2	Measurement . . . . .	63
3.4.3	Time-Resolved MOKE Spectroscopy . . . . .	66
3.5	The OKEMOKE System . . . . .	68
3.5.1	Introduction . . . . .	68
3.5.2	Overview . . . . .	68
3.5.3	The Laser Source . . . . .	68
3.5.4	Pump-Probe Generation . . . . .	69

---

3.5.5	The Chopper Wheels . . . . .	70
3.5.6	OKE/MOKE Mode Selection . . . . .	72
3.5.7	The Sample Holders . . . . .	73
3.5.8	Balanced Detection . . . . .	75
3.5.9	Lock-In Detection . . . . .	76
3.6	Practical Experimental Considerations . . . . .	83
3.6.1	Introduction . . . . .	83
3.6.2	Separation of Signal and Noise . . . . .	83
3.6.3	The Chopper-Reprate Mismatch . . . . .	83
3.6.4	Anti-Reflection Coating . . . . .	84
3.6.5	Kerr Defocusing . . . . .	84
<b>4</b>	<b>Results</b>	<b>87</b>
4.1	Bandwidth of the Laser . . . . .	87
4.2	OKE Spectroscopy . . . . .	87
4.2.1	Overview . . . . .	87
4.2.2	Deionized Water - H <sub>2</sub> O . . . . .	89
4.2.3	Acetone - (CH <sub>3</sub> ) <sub>2</sub> CO . . . . .	89
4.2.4	Iron-Doped Zinc Sulfide on Sapphire Substrate - Fe:ZnS/Al <sub>2</sub> O <sub>3</sub> . . . . .	90
4.2.5	OKE Signal vs Pump Power . . . . .	92
4.3	MOKE Spectroscopy . . . . .	93
4.3.1	Overview . . . . .	93
4.3.2	Hysteresis of Permalloy - Ni <sub>0.8</sub> Fe <sub>0.2</sub> . . . . .	93
4.3.3	Ultrafast Demagnetization and Recovery of Permalloy . . . . .	94
<b>5</b>	<b>Analysis</b>	<b>99</b>
5.1	Bandwidth Limit vs Nyquist Limit . . . . .	99
5.2	Analysis of OKE Data . . . . .	100
5.2.1	Overview . . . . .	100
5.2.2	The Instrument Function . . . . .	101
5.2.3	The Third-Order Susceptibility . . . . .	104
5.2.4	Dark Noise and Dynamic Range . . . . .	105
5.3	Analysis of MOKE Data . . . . .	107
5.3.1	Overview . . . . .	107
5.3.2	Hysteresis . . . . .	108
5.3.3	Time-Resolved MOKE . . . . .	109
<b>6</b>	<b>Conclusion</b>	<b>111</b>
6.1	Concluding Remarks . . . . .	111
6.2	Further Work . . . . .	112
	<b>Bibliography</b>	<b>115</b>
	<b>Appendix</b>	<b>119</b>
	<b>Appendices</b>	<b>121</b>

---

---

<b>A Numerical Solution of the Nonlinear Wave Equation</b>	<b>123</b>
<b>B The Density Matrix</b>	<b>125</b>
<b>C Lorentz Model of Magneto-Optical Interactions</b>	<b>129</b>

# List of Tables

2.1	Summary of the electromagnetic fields and charge fields with SI-units. Multiple names exist for some of the fields - the one listed in the table follow the nomenclature used by Kong [10]. . . . .	8
2.2	Some important polarization states and associated Jones vectors. Jones vectors taken from [11]. . . . .	12
2.3	Jones matrix for linear polarizer and wave retarder. The coordinate transformation matrix can be applied to transform a Jones matrix in a given coordinate system to another coordinate system rotated by an angle $\theta$ . This can be done by the transformation $T' = R(\theta)TR(-\theta)$ , and back again by $T = R(-\theta)T'R(\theta)$ . If the angle $\Gamma$ in the wave retarder matrix is $\pi/2$ or $\pi/4$ , it acts as a half-wave plate (HWP) or quarter-wave plate (QWP) respectively. Jones matrices taken from [11]. . . . .	13
2.4	Some key differences between linear and nonlinear optics (summarized from [11]). . . . .	15
2.5	Linear (even) MO effects, classified by intensity/polarization analysis and reflection/transmission. Polarization sensitive effects include the Faraday effect, and polar and longitudinal MOKE. Intensity sensitive effects include magnetic circular dichroism (MCD) and transversal MOKE [24]. . . . .	48
3.1	Overview of the pump and probe mechanisms for OKE and MOKE spectroscopy. . . . .	53
3.2	Components of the OKEMOKE system. . . . .	69
4.1	Experimental parameters for DI water. . . . .	89
4.2	Experimental parameters for acetone. . . . .	90
4.3	Experimental parameters for sample EK086-3. . . . .	92
4.4	Experimental parameters for permalloy. . . . .	94
5.1	Third-order susceptibilities for iron-doped zinc sulfide samples. Values are given in esu units. Previous data for sample EK040-3 was not available. . . . .	104

---

# List of Figures

1.1	Transition regions vs temperature for $\text{SrO}(\text{La}_{1-x}\text{Sr}_x\text{MnO}_3)$ at different ratios $x$ . FM and AF indicates ferromagnetic and antiferromagnetic transitions. Figure taken from [7]. . . . .	2
2.1	Illustration of the two Maxwell curl equations - the curl of a vector field is the limit of the line integral of the field around a closed loop divided by the area of the loop, as the area approaches a point. The direction of integration follows the right-hand rule. (a) Ampère's law (2.1); the black vectors show the $\mathbf{H}$ field at an infinitesimal point in space, and the green vector is the curl of $\mathbf{H}$ . The red and blue vectors are $\mathbf{J}$ and the time derivative of $\mathbf{D}$ respectively. (2.1) states that the green vector is equal to the sum of the red and blue vector. (b) Faraday's law (2.2); the black vectors show the $\mathbf{E}$ field at an infinitesimal point in space, and the green vector is the curl of $\mathbf{E}$ . The red vector is the time derivative of $\mathbf{B}$ . (2.2) states that the green vector is equal in magnitude to the red vector, and points in the opposite direction (Lenz's law). . . . .	6
2.2	Illustration of the two Maxwell divergence equations - the divergence of a vector field is the limit of the surface integral of the field around an enclosed volume divided by the volume, as the volume approaches a point. (a) Gauss's law (2.3); the black vectors show the $\mathbf{D}$ field at an infinitesimal point in space, and the red sphere is a positive charge. (2.3) states that the total outgoing flux density of the volume is equal to the charge density $\rho$ . Due to sign convention, a negative charge would produce an in-going flux, which is equivalent to a negative flux density and negative divergence. (b) Gauss's law for magnetism (2.4); the black vectors show the $\mathbf{B}$ field at an infinitesimal point in space. The total outgoing flux is always zero, since magnetic monopoles do not exist. The in-going flux is exactly equal to the outgoing flux, such that the field lines always close in on themselves. A divergence-free vector field is called a solenoidal field. . . . .	7

---

2.3	Monochromatic electromagnetic wave, propagating in the z-direction and polarized in the y-direction. The wave equation, derived from Maxwell's equations, enables propagation of this wave. . . . .	9
2.4	Polarization ellipse. The polarization state is described by the angles $\Psi$ which signifies the rotation of the majority axis and the ellipticity angle $\chi$ , describing the width of the ellipse. . . . .	13
2.5	John Kerr (1824-1907) [12]. . . . .	14
2.6	Illustration of linear, quadratic (second-order) nonlinear and cubic (third-order) nonlinear media. Third-order media behave symmetrically to an applied electric field, while second-order media behave asymmetrically. . . . .	17
2.7	Schematic illustration of the nonlinear wave equation. . . . .	19
2.8	Illustration of the 27 elements in the $\chi^{(2)}$ tensor. Each colored slice can be considered a 2nd rank tensor, i.e. a regular matrix. When a specific vector component $i$ of $\mathbf{P}^{(2)}$ is considered (i.e. $P_i^{(2)}$ ), the tensor is reduced to the matrix with the corresponding index (shown here by the different colors). . . . .	21
2.9	Illustration of phase modulation within a third-order nonlinear medium. The phase is modulated because (a) the intensity of the beam is strong enough to alter its own refractive index, (b) a pump beam alters the refractive index for a weak beam, assumed too weak to alter its own refractive index. Intensity is indicated by the thickness of the arrows. . . . .	26
2.10	Simple two-level system. . . . .	30
2.11	Two level system with virtual states created by the forced oscillations of the electromagnetic wave. . . . .	33
2.12	Possible transitions of second-harmonic generation in a three-level system. The black arrows show the real level sequence, the gray arrows show possible virtual sequences and the solid double-sided arrows show the separation energy between the real and virtual levels. . . . .	34
2.13	Transition sequences for IDRI. . . . .	35
2.14	Simple Raman resonance model for system with two nuclear vibrational levels ( $g^0$ and $g^1$ ) and two electronic levels ( $n^0$ and $n^1$ ). . . . .	36
2.15	<b>(a)</b> First Stokes scattering <b>(b)</b> Stimulated Raman gain <b>(c)</b> Anti-Stokes scattering <b>(d)</b> Second Stokes scattering. . . . .	37
2.16	Dispersion relation for the third-order susceptibility. The solid curve shows the real part, and the dashed curve shows the imaginary part. Off-resonance, the susceptibility is dominated by a constant background susceptibility, originating from the instantaneous electronic response. The graph is intended to reflect the results presented by [19]. . . . .	38
2.17	Classification of magnetic materials. . . . .	39
2.18	Hysteresis curve (thick line) with initial magnetization from unmagnetized state (dashed line). Coercivity, saturation magnetization and remanence field are marked in the figure. The arrows indicate the direction of the magnetic cycle. . . . .	41

---

---

2.19	Experimental MOKE geometries. The dashed line indicates the plane of incidence, the red arrows show the incident and reflected light, and the black arrow shows the direction of magnetization. The magnetic field is (a) perpendicular to the interface plane (b) parallel to the interface and normal to the plane of incidence (c) parallel to both the surface and the plane of incidence [22] . . . . .	43
2.20	Linearly polarized wave, polarized along the y-axis, decomposed into a left and right-hand circularly polarized wave. . . . .	44
2.21	Illustration of optical rotation. In a magnetic medium with purely real complex refractive index $N$ , $\hat{\sigma}_+$ and $\hat{\sigma}_-$ travel with different phase velocities and are shifted in phase. The linear polarization state rotates by an angle $\theta_k$ without becoming elliptical. . . . .	45
2.22	Ellipticity from polarization-dependent attenuation of circular waves. The green curve shows the trace of the electric field as an ellipse. The ellipticity is defined by the angle $\eta_k$ . . . . .	46
2.23	Longitudinal MOKE geometry. The plane of incidence is indicated by the red plane, and the polarization states are indicated by the blue shapes. The ferromagnetic sample is magnetized along the x-direction. . . . .	48
3.1	The optical measurement system. Optical and magneto-optical Kerr effect is utilized to perform characterization of materials. . . . .	52
3.2	Illustration of mechanical delay line; a retroreflector mounted on a motorized translation stage. Each $10\ \mu\text{m}$ of distance adds approximately 66 fs of delay time between the pump and the probe. Stationary mirrors are included to bring the beam back to its original trajectory. . . . .	54
3.3	Delay line with stationary mirrors and retroreflector. . . . .	55
3.4	Illustration of pump-probe spectroscopy (pulses are represented by their intensity envelope). The probe is delayed in time with a variable delay line. The probe records different regimes according to the delay time. $\tau_1$ : probe arrives before pump and measures no signal (only the noise), $\tau_2$ : probe arrives together with pump, and measures the excitation by the pump, $\tau_3$ : probe arrives after pump and measures relaxation in the material. The dashed curve illustrates a typical signal obtained from pump-probe spectroscopy. . . . .	56
3.5	Illustration of OKE spectroscopy. The probe is polarized along the x-axis, and the pump is polarized $45^\circ$ with respect to the x-axis. The two beams spatially overlap inside the sample. Rotation of the polarization is measured by the Kerr angle $\theta_K$ . . . . .	57
3.6	OKE signal from deionized (DI) water. The inset shows the full signal on a logarithmic scale. A second peak can be observed around 12 ps due to Fabry-Perot reflections. . . . .	59
3.7	Cuvette with DI water used in the measurement presented in figure 3.6. The inner thickness is 1 mm, which corresponds to half of the effective distance traveled between the first and second peak. . . . .	60

---



---

3.8	Experimental setup of MOKE (probe only). The magnet sits next to the sample and magnetizes the sample in the longitudinal direction. The magnetization of the sample is assumed to be locked completely in the longitudinal direction. . . . .	64
3.9	Procedure for magnetic cycling. The red curve shows the first half of the cycle, and the blue curve shows the second half. The sample must initially be saturated in one direction and then left in a remanence state (1). The field is then reversed and varied from zero (1) to saturation (2) and back to zero (3). The direction is then reversed again, and varied from zero (3) to saturation in the opposite direction (4) and back to zero (1). (1) and (3) marks the points where the magnet must be reversed, and (2) and (4) marks the saturation regions, which corresponds to the maximum backwards and forwards field strengths. . . . .	65
3.10	MOKE holder with permalloy sample. The magnet can be seen to the right.	66
3.11	MOKE spectroscopy sample holder. . . . .	67
3.12	Illustration of the OKEMOKE system. Polarization states are indicated next to polarizers. The dashed line shows the trajectory of the beams when the flip mirrors and mirror towers are raised, and the solid line when the mirrors are lowered. The blue arrows illustrate the static magnetic flux density. <b>B</b> : Beam Stopper, <b>BS</b> : Beam Splitter, <b>CW</b> : Chopper Wheel, <b>FM</b> : Flip Mirror, <b>L</b> : Lens, <b>LP</b> : Linear Polarizer, <b>M</b> : Mirror, <b>MT</b> : Mirror Tower, <b>VA</b> : Variable Attenuator. . . . .	70
3.13	Solstice Laser Amplification System. . . . .	71
3.14	Generation of pump and probe beam. The probe is passed through a delay line, to adjust the temporal overlap. . . . .	72
3.15	Optical chopper wheel, connected to chopper controller. The chopper controller is used to adjust and monitor the chopping frequency, and provides a reference signal to the lock-in amplifier. An optical encoder in the base of the chopper measures the chopping frequency. . . . .	73
3.16	Thorlabs MC2000 and Stanford Research Systems SR450 chopper wheels, used to improve SNR. . . . .	73
3.17	Balanced Detector with top lid removed. A motor sits next to the quarter wave plate, which allows the balance point to be shifted. The two photodiodes can be seen to the right. . . . .	74
3.18	Illustration of balanced detector used to measure polarization of the probe. <b>QWP</b> : Quarter Wave Plate, <b>WP</b> : Wollaston Prism, <b>PD</b> : Photodiodes. . . .	76
3.19	SR830 lock-in amplifier, showing x and y components of the measured signal (in microvolts). . . . .	77
3.20	Functional block diagram of SR830 dual-phase lock-in amplifier, taken from [37]. . . . .	78
3.21	Tektronix DPO2014 Digital Phosphor Oscilloscope (100 MHz, 4-Ch, 1 GS/s), displaying signal from detector (green) and reference signal from lock-in (yellow). . . . .	79

---

---

3.22	Simulated detector response with fundamental frequency of 1 kHz. The fundamental frequency is illustrated by the dashed line (amplitude not to scale). The noise is Gaussian distributed. . . . .	80
3.23	Simulated detector response with chopping frequency of 520 Hz. The fundamental period of the detector signal is now nearly twice as long, due to the chopper. The shaded area shows the modulation of the signal induced by the pump (positive and negative halves correspond to clockwise and counter-clockwise depolarization of the probe - see section 3.5.8). Note that the exact shape of the modulation envelope depends on the optics. . .	81
3.24	Result after signal and reference multiplication with (a) noise (b) probe (c) pump and probe. The DC component in (c) can be extracted with a low-pass filter. . . . .	82
3.25	Samples of permalloy with optical coating . . . . .	85
3.26	Illustration of the Kerr defocusing effect. The gradient illustrates the beam intensity profile, which is proportional to the second-order index of refraction. . . . .	85
4.1	Bandwidth of the lasers. . . . .	88
4.2	OKE signal from deionized (DI) water. The inset shows the full signal on a logarithmic scale. . . . .	90
4.3	OKE signal from acetone. The inset shows the full signal on a logarithmic scale.. . . .	91
4.4	OKE signal from sample EK086-3. Film-thickness: 3.3 $\mu\text{m}$ , iron concentration: 6.0 %. . . . .	93
4.5	OKE peak signal and dark noise for different pump powers. . . . .	95
4.6	Raw data of the magnetic flux density along the x-direction of the sample, used to measure hysteresis in MOKE spectroscopy. The arrows indicate the direction of the magnetic cycle. The negative portion of the distance-axis indicate that the magnet was moving towards the sample, and the positive portion indicates that it was moving away from the sample. . . .	96
4.7	Raw MOKE signal, obtained with longitudinal MOKE spectroscopy. The asymmetry around the mirror point (illustrated by the green line) indicates a permanent reversal of the magnetization. . . . .	96
4.8	Raw data from time-resolved MOKE spectroscopy. The full range of the translation stage was used for the measurement. . . . .	97
4.9	Time-domain noise measurement on TR-MOKE from probe only. The first 100 ps have noise correlated across multiple scans, and is believed to originate in a slight shift in the probe alignment from the translation stage.	97
5.1	Broadband Raman resonance, with two modes excited. Frequencies $\omega_1$ , $\omega_2$ , $\omega_3$ and $\omega_4$ must be contained within the bandwidth in order to excite the two modes. The highest frequency that can be excited must fulfill the criteria $\Omega < \Delta\nu$ . . . . .	100
5.2	Construction of instrument function (dashed curve) from measured signal on DI water (black curve). The shaded region was mirrored around a point close to the peak. The black line indicates the mirror point. . . . .	101

---

---

5.3	Logarithmic plot of signal and instrument function. . . . .	102
5.4	Signal and instrument function after cropping. Only the initial part of the signal is shown - the full signals extend out to 11 ps. . . . .	103
5.5	Imaginary part of spectra. A slight frequency shift has been introduced to improve the overlap of the signals in the frequency-domain. . . . .	104
5.6	Raman spectrum of DI water. Experimental data has been fitted to a sum of three Gaussians centered around theoretical transition frequencies. . . . .	105
5.7	Dependence of signal peak and dark noise on pump power, measured with OKE spectroscopy on DI water. . . . .	106
5.8	Dynamic range plotted against pump power of single-scan measurements. . . . .	107
5.9	Magnetic flux density of the north pole and south pole of the magnet, measurement and fit. . . . .	108
5.10	TR-MOKE signal of permalloy. . . . .	109
5.11	Hysteresis measurement of permalloy. The hysteresis was measured to be $1.43 \text{ mT} \pm 0.2 \text{ mT}$ , indicated by the green lines. Only fringes have been measured due to restrictions in available magnetic flux density. . . . .	110
A.1	Solution of the nonlinear wave equation, based on the Crank-Nicolson method (central time, central space) and the 1st Born approximation, with the CLF condition for numerical stability. The initial electric field is a femtosecond Gaussian wave-packet with central frequency $\lambda_c = 700 \text{ nm}$ . A second-harmonic component at $\lambda_c/2$ can be seen in the final power spectral density, due to the nonlinear interaction. Additional component arise at $\lambda_c/n$ and $\lambda_c/2n$ due to residual reflected light within the medium, and a component arises at $\lambda = 0$ due to optical rectification (although this is rather weak because the majority of the wave has left the medium). The figure is only indented for illustrative purposes, and may contain numerical errors. . . . .	124

---

# Abbreviations

AC	=	Alternating Current
AG	=	Asymmetrized Gaussian
AR	=	Anti-Reflection
BL	=	Bucaro-Litovitz
c.c.	=	Complex Conjugate
CARS	=	Coherent Anti-Stokes Raman Scattering
DC	=	Direct Current
DFG	=	Difference-Frequency Generation
DI	=	Deionized
DR	=	Dynamic Range
FWHM	=	Full-Width At Half Maximum
HWP	=	Half Wave Plate
IC	=	Integrated Circuit
IDRI	=	Intensity-Dependent Refractive Index
IPS	=	Intrinsic Permutation Symmetry
L-MOKE	=	Longitudinal MOKE
MCD	=	Magnetic Circular Dichroism
MO	=	Magneto-Optics/Magneto-Optical
MOKE	=	Magneto-Optical Kerr Effect
MSHG	=	Magnetically Induced SHG
NL	=	Nonlinear
NOLIMOKE	=	Nonlinear MOKE
OKE	=	Optical Kerr Effect
OKEMOKE	=	Optical Kerr Effect - Magneto-Optical Kerr Effect
OR	=	Optical Rectification
P-MOKE	=	Polar MOKE
PD	=	Photodiode
PSD	=	Phase-Sensitive Detector
QM	=	Quantum Mechanics
QWP	=	Quarter Wave Plate
SFG	=	Sum-Frequency Generation
SHG	=	Second-Harmonic Generation
SNR	=	Signal-To-Noise Ratio
SRG	=	Stimulated Raman Gain
SRL	=	Stimulated Raman Loss
T-MOKE	=	Transversal MOKE
THG	=	Third-Harmonic Generation
THz	=	Terahertz
TR	=	Time-Resolved
XPM	=	Cross-Phase Modulation

---

# Introduction

## 1.1 Project Work and Motivation

Since the early 1970s, technological advancements in computing have largely been driven by Moore's law, which predicts that the number of transistors in an integrated circuit (IC) will double every 12 to 18 months. The power consumption of each transistor scales linearly with size according to Dennard's scaling law, such that the total power consumption of an IC remains constant with die area [1]. In recent years however, this practice has been challenged by physical limitations in the silicon. This is often referred to as the *breaking of Moore's law*. After the 65 nm CMOS benchmark was reached in 2006-2007, power consumption became a limiting factor, and this evolution has led to the issue of *dark silicon* in modern multicore processors - a large number of transistors are under-utilized at any time to avoid overheating [2]. Power consumption in the form of heat dissipation is an inherent problem in conventional logic devices with charge-based signal carriers. Alternative, non-charge based solutions have been proposed, where magnetic properties such as spin succeeds the role of charge as the signal carrier. The 2015 International Roadmap of Semiconductors lists SpinFETs, Nanomagnetic logic devices and Spinwave logic devices as novel candidates [3]. Thanks to the nonvolatile nature of spin in ferromagnetic media, extremely low-powered magnetic devices are indeed feasible. Understanding the characteristics of heat and spin transfer in such media is paramount, and requires extremely fast, and highly sensitive measurement techniques.

Since the invention of the laser in the 1960s, optical detection of atomic and molecular behavior has provided revolutionary insight into the microscopic world. The advent of ultrafast laser sources with pulse widths in the femtosecond ( $10^{-15}$  s) scale has enabled probing of dynamic processes down to the timescale of nuclear motion [4]. Techniques in optical amplification has further brought about laser sources with peak power of several gigawatts, whose electric field strength rivals the interatomic fields of atoms (on the order of  $10^7$  V m<sup>-1</sup>) [5]. This has led to advances in the field of nonlinear optics, and the well-defined energy levels of molecules can be probed by resonant effects such as the stimulated Raman effect [6].

This masters project is aimed towards the creation and testing of an optical spectroscopic system, capable of characterizing properties of magnetic media at ultrafast timescales. This work is motivated by the possibility of performing in-house measurements on magnetic perovskite oxides, epitaxially grown by The Oxide Electronics Group at NTNU. Perovskite oxides encompass solids with the same crystalline structure as calcium titanium oxide - the perovskite crystal structure. The chemical formula for perovskites is  $ABO_3$ , where A and B are different cations, bonded by the anion oxides. The A and B site elements are of very different size, and often include rare earth elements. In perovskite materials, electrons can be strongly correlated, and material properties depend greatly on the ratio of the A and B site elements [7]. This is illustrated in figure 1.1, which shows different transition regions of bilayer manganates  $SrO(La_{1-x}Sr_xMnO_3)_2$  for different temperatures and ratios  $x$ . Both ferromagnetic and antiferromagnetic transitions are observed. Particularly, lanthanum strontium manganite ( $La_{0.7}Sr_{0.3}MnO_3$ ) grown on strontium titanate ( $SrTiO_3$ ) is of interest to the group. The thickness of these films are typically less than 100 unit cells, and optical characterization is therefore difficult. In place of the perovskite materials, known reference samples will instead be characterized, to experimentally verify that the system is working as intended, and open up the possibility for future work in the laboratory.

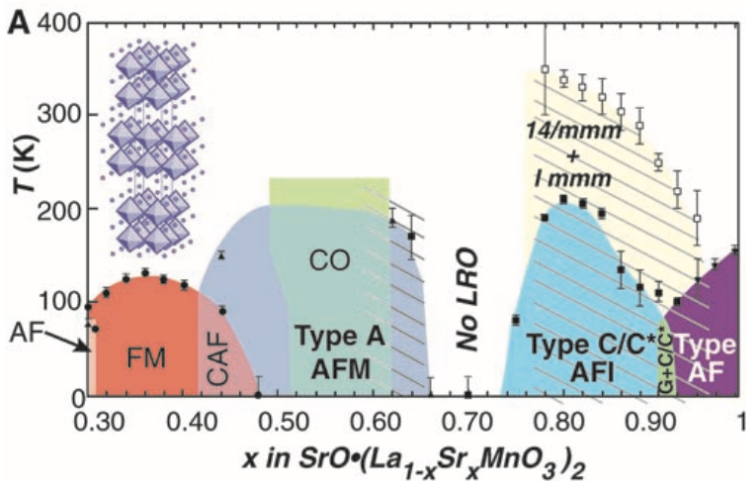


**Figure 1.1:** Transition regions vs temperature for  $SrO(La_{1-x}Sr_xMnO_3)_2$  at different ratios  $x$ . FM and AF indicates ferromagnetic and antiferromagnetic transitions. Figure taken from [7].

The feasibility of using nonlinear and magneto-optical measurement techniques for optical characterization are explored in this thesis. Both these branches of optics date back to the 1800s, with the first evidences of magneto-optics discovered by Michael Faraday in 1845, and nonlinear optics by John Kerr in 1875. It was however not until the 1960s, when the laser was invented, that nonlinear optics expanded as a field of study. Studies on magneto-optics have historically been motivated by optically accessible information stored in high-density magnetic materials [8]. This is highly relevant today, due to the potential

applications in magnetic devices, as mentioned previously. Studies of demagnetization and magnetization recovery transients has also been made possible by the ultrafast temporal widths of femtosecond lasers. The time-resolved magnetization dynamics conveys crucial information about limitations in practical applications, because it fundamentally limits the rate of magnetic switching and energy consumption.

The system will be built as an extension to a previously existing spectroscopy system, based on third-order nonlinear optics. The intention is to preserve and improve the capabilities of the old system, and incorporate new measurements based on magneto-optic effects. The nonlinear optical system will also be used to perform characterization of samples intended for mid-infrared Q-switched laser applications, on request from another group of researchers.

## 1.2 What is Spectroscopy?

Spectroscopy is the process in which light interacts with some medium, and the light that is reflected or transmitted is analyzed to gain knowledge about the medium. It comes from the Latin *spectron*, meaning *spirit* or *ghost*, and the Greek *σκοπειν* meaning *to see* [9]. The name is telling, because in molecular spectroscopy, nothing is in direct contact with the medium - only light. The molecules are never directly *seen* in spectroscopy, but their influence on light carries a great deal of information about the molecular world. The indirectness of the process means that a theoretical model is needed, to transition between the measured signals and conclusions about matter. The model must describe the behavior of matter and incorporate the effects of light. In this masters project, both nonlinear and magnetic media have been investigated through spectroscopy. The underlying physics behind these two types of media are rather different, and the theoretical background needed to understand all processes is relatively wide. Chapter 2 contains the fundamental theory which is used in the analysis, and is intended to encompass, as completely as possible, all light-matter interactions relevant to the project. It would however be impossible to fully cover these branches of physics in a single masters thesis, due to the sheer vastness of information that has been accumulated over more than a century.

Multiple spectroscopic techniques have been employed in this project work: *optical Kerr effect* (OKE) and *magneto-optical Kerr effect* (MOKE) spectroscopy has been used to carry out measurements of nonlinear and magnetic properties respectively. This signifies the physical origin of the *interaction process*. A wave of light has many properties which can be altered by a medium and detected, such as e.g. wavelength, phase, intensity and polarization. OKE and MOKE spectroscopy are both examples of *polarization spectroscopy*, which signifies that polarization is the *property of light* that is altered in the process. The measurements are also scanned in time, by employing *pump-probe spectroscopy*. This achieves *time-resolved (TR) measurements*, as opposed to resolving measurements in e.g. the frequency domain. Spectral information is obtained indirectly from TR measurements through the Fourier transform.



### **1.3 Outline of the Thesis**

The thesis is divided into six chapters; chapter 2 covers the underlying physics, and is intended to familiarize the reader with the concepts utilized in experiments. Only rudimentary electromagnetism and quantum mechanics has been assumed known to the reader in writing this chapter. The experimental system is described in detail in chapter 3, along with how data is interpreted and analyzed. Practical experimental considerations are also covered, which are intended to improve the repeatability of the measurements. Results and analysis are presented in chapters 4 and 5 respectively. The provided results are accompanied by experimental parameters, which further increase repeatability. Lastly, chapter 6 concludes the work and gives an outline for future work.

# Chapter 2

## Theory

### 2.1 Introduction

All spectroscopy is based on the properties of electromagnetic waves, and their interaction with matter. Spectroscopic analysis therefore resides on the understanding of light, matter, and the influence one has on the other. The theory of light is provided by the Maxwell equations, from which the classical results are still highly valid in the general context. Matter, and light matter interactions, are classically described by the constitutive relations, in terms of the polarization and magnetization vectors. The same results may be obtained from quantum mechanics, by introducing the classical electromagnetic field as a perturbation in the Hamiltonian and calculating the expectation values of the dipole operator. The latter approach defines the field of quantum electronics. Quantum mechanics also provides a description of nonlinear resonance effects, which fall outside the scope of the classical model.

This chapter is divided into six sections, which are intended to cover different branches of optics relevant to the thesis work. The introductory chapter presents fundamental electromagnetic wave theory, and is followed by sections on polarization optics, linear and nonlinear optics and magneto optics. A section on quantum mechanics has also been included to complete the discussion on nonlinear optics, as well as a section on magnetism in materials.

This chapter is primarily intended to cover general theory; the theory specific to the experimental setup has been reserved for chapter 3. The chapter is also intended to be as complete as possible, assuming only intermediate knowledge of electromagnetism and a rudimentary understanding of quantum mechanics, and derives results directly usable in the experimental work.

## 2.2 Electromagnetism

### 2.2.1 Introduction

According to the standard model of particle physics, there are four fundamental forces in the universe: gravitation, electromagnetism, the weak force and the strong force. The forces are mediated by their respective fields - properties of space which evolve in space and time according to their field equations. Electromagnetic fields are described by the Maxwell equations [10];

$$\nabla \times \mathbf{H} = \mathbf{J} + \frac{\partial \mathbf{D}}{\partial t} \quad (2.1)$$

$$\nabla \times \mathbf{E} = -\frac{\partial \mathbf{B}}{\partial t} \quad (2.2)$$

$$\nabla \cdot \mathbf{D} = \rho \quad (2.3)$$

$$\nabla \cdot \mathbf{B} = 0 \quad (2.4)$$

Maxwell's equations  
(General differential form)

where  $\mathbf{E}$  is the electric field,  $\mathbf{D}$  is the electric displacement,  $\mathbf{H}$  is the magnetic field,  $\mathbf{B}$  is the magnetic flux density,  $\mathbf{J}$  is the electric free current density and  $\rho$  is the electric free charge density.  $\mathbf{E}$ ,  $\mathbf{D}$ ,  $\mathbf{H}$ ,  $\mathbf{B}$ ,  $\mathbf{J}$  and  $\rho$  are all functions of three-dimensional space and time. The Maxwell equations are illustrated in figures 2.1 and 2.2.

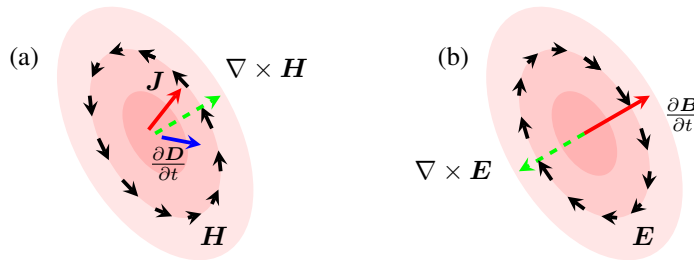


**Figure 2.1:** Illustration of the two Maxwell curl equations - the curl of a vector field is the limit of the line integral of the field around a closed loop divided by the area of the loop, as the area approaches a point. The direction of integration follows the right-hand rule. (a) Ampère's law (2.1); the black vectors show the  $\mathbf{H}$  field at an infinitesimal point in space, and the green vector is the curl of  $\mathbf{H}$ . The red and blue vectors are  $\mathbf{J}$  and the time derivative of  $\mathbf{D}$  respectively. (2.1) states that the green vector is equal to the sum of the red and blue vector. (b) Faraday's law (2.2); the black vectors show the  $\mathbf{E}$  field at an infinitesimal point in space, and the green vector is the curl of  $\mathbf{E}$ . The red vector is the time derivative of  $\mathbf{B}$ . (2.2) states that the green vector is equal in magnitude to the red vector, and points in the opposite direction (Lenz's law).

The electric charge and current densities obey the conservation law for electric charge

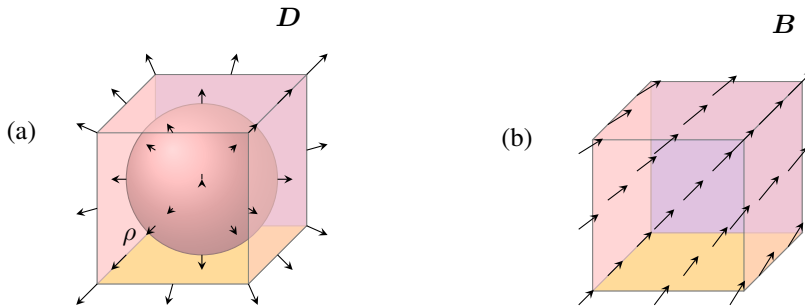


**Figure 2.2:** Illustration of the two Maxwell divergence equations - the divergence of a vector field is the limit of the surface integral of the field around an enclosed volume divided by the volume, as the volume approaches a point. (a) Gauss's law (2.3); the black vectors show the  $\mathbf{D}$  field at an infinitesimal point in space, and the red sphere is a positive charge. (2.3) states that the total outgoing flux density of the volume is equal to the charge density  $\rho$ . Due to sign convention, a negative charge would produce an in-going flux, which is equivalent to a negative flux density and negative divergence. (b) Gauss's law for magnetism (2.4); the black vectors show the  $\mathbf{B}$  field at an infinitesimal point in space. The total outgoing flux is always zero, since magnetic monopoles do not exist. The in-going flux is exactly equal to the outgoing flux, such that the field lines always close in on themselves. A divergence-free vector field is called a solenoidal field.

$$\nabla \cdot \mathbf{J} = -\frac{d\rho}{dt}. \quad (2.5)$$

The fields are related to mechanics by the Lorentz force equation which states that the force acting upon a charged particle by an electromagnetic field is

$$\mathbf{F} = q(\mathbf{E} + \mathbf{v} \times \mathbf{B}) \quad (2.6)$$

where  $\mathbf{F}$  is the Lorentz force,  $q$  is the charge of the particle and  $\mathbf{v}$  is its velocity.

Matter is comprised of particles with innate electric charge, and are naturally affected by electric and magnetic fields. In dielectric media, in which free charges and currents are absent, the externally applied electric field can induce dipole moments, align permanent dipole moments, or migrate ionic charge [10]. The interaction can be described by a free-space component and component from the material alone. The electric polarization vector  $\mathbf{P}$  is introduced to describe the material-dependent interaction. A similar interaction may be observed between the externally applied magnetic field and the perpetual orbital motion of the electrons in atomic orbitals. The magnetization vector  $\mathbf{M}$  is introduced to describe the material-dependent component of the magnetic field, analogous to the electric polarization. Magnetic interactions are highly material-dependent, and are further discussed in section 2.6. With the addition of  $\mathbf{P}$  and  $\mathbf{M}$ , there is a total of six electromagnetic fields, but only four equations to describe them. Two additional equations are required, termed the constitutive relations. They describe the separation of free-space and material-dependent contributions of the fields. The constitutive relations are commonly expressed as

$$\mathbf{D} = \epsilon_0 \mathbf{E} + \mathbf{P} \quad (2.7)$$

$$\mathbf{H} = \frac{1}{\mu_0} \mathbf{B} - \mathbf{M} \quad (2.8)$$

where  $\epsilon_0$  is the free-space permittivity and  $\mu_0$  is the free-space permeability. Provided that the material is linear,  $\mathbf{P}$  and  $\mathbf{M}$  may be included in the material permittivity and permeability

$$\mathbf{D} = \epsilon \mathbf{E} \quad (2.9)$$

$$\mathbf{H} = \frac{1}{\mu} \mathbf{B} \quad (2.10)$$

with

$$\mathbf{P} = \epsilon_0 \chi \mathbf{E} \quad (2.11)$$

$$\mathbf{M} = \chi_m \mathbf{H} \quad (2.12)$$

where  $\chi$  is the electric susceptibility and  $\chi_m$  is the magnetic susceptibility (both dimensionless). The six electromagnetic fields and the two charge fields are summarized in table 2.1 with SI-units.

**Table 2.1:** Summary of the electromagnetic fields and charge fields with SI-units. Multiple names exist for some of the fields - the one listed in the table follow the nomenclature used by Kong [10].

Symbol	Name	Unit
$\mathbf{E}$	Electric field	V/m
$\mathbf{D}$	Electric displacement	C/m <sup>2</sup>
$\mathbf{P}$	Electric polarization	C/m <sup>2</sup>
$\mathbf{H}$	Magnetic field	A/m
$\mathbf{B}$	Magnetic flux density	Wb/m <sup>2</sup>
$\mathbf{M}$	Magnetization	A/m
$\mathbf{J}$	Electric current density	A/m <sup>2</sup>
$\rho$	Electric free charge density	C/m <sup>3</sup>

## 2.2.2 The Electromagnetic Wave Equation

Equations (2.1)-(2.4) can be combined to derive a wave equation for electromagnetic waves. This is feasible because an electric field that changes in time always has accompanied with it a magnetic field, and vice versa. Figure 2.3 shows a snapshot at a given time of an electromagnetic wave propagating along the z-direction. The wave is polarized in the y-direction (polarization of waves is explained in section 2.3). The wave equation

is central to all of optics, and particularly in the field of nonlinear optics, which is later shown.

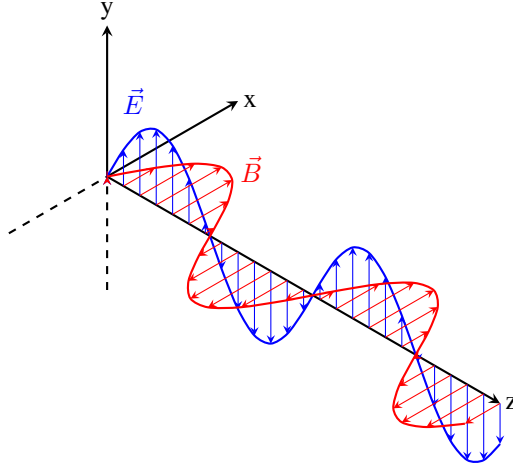


**Figure 2.3:** Monochromatic electromagnetic wave, propagating in the z-direction and polarized in the y-direction. The wave equation, derived from Maxwell's equations, enables propagation of this wave.

The wave equation for the electric field can be derived by taking the curl of (2.2) (or the curl of (2.1) for the magnetic field)

$$\nabla \times \nabla \times \mathbf{E} = -\frac{\partial}{\partial t} \nabla \times \mathbf{B} \quad (2.13)$$

with (2.8) for the  $\mathbf{B}$  field

$$\nabla \times \nabla \times \mathbf{E} = -\mu_0 \frac{\partial}{\partial t} (\nabla \times \mathbf{H} + \nabla \times \mathbf{M}). \quad (2.14)$$

Inserting (2.1) for  $\nabla \times \mathbf{H}$  with the constitutive relation (2.7) for  $\mathbf{D}$  we obtain

$$\nabla \times \nabla \times \mathbf{E} = -\mu_0 \frac{\partial}{\partial t} \left( \mathbf{J} + \mu_0 \frac{\partial \mathbf{E}}{\partial t} + \frac{\partial \mathbf{P}}{\partial t} + \nabla \times \mathbf{M} \right). \quad (2.15)$$

Moving the  $\mathbf{E}$  terms to the left-hand side and introducing the effective current density  $\mathbf{J}_{eff}$  yields

$$\nabla \times \nabla \times \mathbf{E} + \epsilon_0 \mu_0 \frac{\partial^2 \mathbf{E}}{\partial t^2} = -\mu_0 \frac{\partial \mathbf{J}_{eff}}{\partial t}. \quad (2.16)$$

where

$$\mathbf{J}_{eff} = \mathbf{J} + \frac{\partial \mathbf{P}}{\partial t} + \nabla \times \mathbf{M}. \quad (2.17)$$

(2.16) states that within a point in a medium, a time-varying  $\mathbf{P}$  field or a rotating  $\mathbf{M}$  field (described by the curl operator) acts identical to a current density. The time-derivative

of the effective current density acts as a source-term in the wave equation for the electric field.

The vector triple product is given by Lagrange's formula

$$\mathbf{A} \times (\mathbf{B} \times \mathbf{C}) = \mathbf{B}(\mathbf{A} \cdot \mathbf{C}) - \mathbf{C}(\mathbf{A} \cdot \mathbf{B}). \quad (2.18)$$

By setting  $\mathbf{A} = \mathbf{B} = \nabla$ , the curl of the curl of  $\mathbf{E}$  is

$$\nabla \times \nabla \times \mathbf{E} = \nabla(\nabla \cdot \mathbf{E}) - \nabla^2 \mathbf{E}. \quad (2.19)$$

The first term on the right-hand side of (2.19) is further simplified by insertion of (2.7) and (2.3)

$$\nabla(\nabla \cdot \mathbf{E}) = \frac{1}{\epsilon_0} \nabla(\nabla \cdot \mathbf{D} - \nabla \cdot \mathbf{P}) \quad (2.20)$$

$$= \frac{1}{\epsilon_0} \nabla(\rho + \rho_b) \quad (2.21)$$

$$= \frac{1}{\epsilon_0} \nabla \rho_{tot} \quad (2.22)$$

where the equation

$$\nabla \cdot \mathbf{P} = -\rho_b \quad (2.23)$$

was used to express the source of the polarization field due to the bound charge density  $\rho_b$ , and where  $\rho_{tot}$  is the total charge density of free and bound charges. So long as the spatial variation of the charge density is slow compared to an optical wavelength (which generally is a reasonable assumption) the gradient of  $\rho_{tot}$  is very small and the term may be neglected. The curl of the curl of  $\mathbf{E}$  is thus equal to the Laplacian of  $\mathbf{E}$ . The result is

$$\nabla^2 \mathbf{E} - \epsilon_0 \mu_0 \frac{\partial^2 \mathbf{E}}{\partial t^2} = \mu_0 \frac{\partial \mathbf{J}_{eff}}{\partial t}, \quad (2.24)$$

which is a wave equation with free-space velocity  $c_0 \equiv \frac{1}{\sqrt{\epsilon_0 \mu_0}}$  and a source-term  $\mu_0 \frac{\partial \mathbf{J}_{eff}}{\partial t}$ .

In the absence of charges and currents (e.g. in vacuum/air), the source-term vanishes and the wave equation becomes homogeneous

$$\boxed{\nabla^2 \mathbf{E} - \frac{1}{c_0^2} \frac{\partial^2 \mathbf{E}}{\partial t^2} = 0} \quad (2.25)$$

Free-space wave equation

with  $c_0 = 299\,792\,458$  m/s, the speed of light in vacuum.

In non-conductive, non-magnetic media,  $\mathbf{J}$  and  $\nabla \times \mathbf{M}$  vanishes in (2.17) and the only source of radiation is the electrical polarization of the medium.

$$\nabla^2 \mathbf{E} - \frac{1}{c_0^2} \frac{\partial^2 \mathbf{E}}{\partial t^2} = \mu_0 \frac{\partial^2 \mathbf{P}}{\partial t^2}. \quad (2.26)$$

Wave equation, non-magnetic,  
non-conductive medium

## 2.3 Polarization Optics

### 2.3.1 Introduction

As an electromagnetic wave propagates in free space, the electric and magnetic fields oscillate in the transverse plane of the wave. The envelope of the wave is characterized by its polarization, which is an intrinsic property of the wave. In the nomenclature of electromagnetism, the word *polarization* is often used ambiguously. It may refer to either (1) the *electric polarization field*,  $\mathbf{P}$ , that describes the separation of charges in a medium due to electrostatic induction, or (2) the envelope of an electromagnetic wave. Both definitions are used frequently throughout this chapter, and the meaning of the word is therefore contextual.

### 2.3.2 Jones Vectors and Jones Matrices

A monochromatic plane wave propagating in the z-direction may be expressed as the real part of a complex phasor

$$\mathbf{E}(z, t) = \text{Re}\{\mathbf{E}_0 e^{i(\omega t - k_z z)}\} \quad (2.27)$$

where  $\mathbf{E}_0 = E_x \hat{\mathbf{x}} + E_y \hat{\mathbf{y}}$  is the complex envelope of the wave. It is convenient to express  $E_x$  and  $E_y$  in a compact column matrix form, called the Jones vector

$$\mathbf{J} = \begin{bmatrix} E_x \\ E_y \end{bmatrix}. \quad (2.28)$$

A coherent plane wave with known frequency and direction of propagation is completely characterized by its Jones vector [11].

Interaction between light and matter can result in a change in the Jones vector. In the Jones formalism, the interaction is described by a Jones matrix  $\mathbf{T}$  for the given medium, such that the input Jones vector  $\mathbf{J}_1$  is related to the output Jones vector  $\mathbf{J}_2$  by

$$\mathbf{J}_2 = \mathbf{T} \mathbf{J}_1. \quad (2.29)$$

A system composed of cascaded optical elements with individual Jones matrices may be expressed by its own equivalent Jones matrix that is the product of each individual Jones matrix. The innermost term in the matrix product corresponds to the first element, and



the outermost term corresponds to the last element. In a system with  $N$  elements, the equivalent Jones matrix is

$$\mathbf{J}_2 = \underbrace{\mathbf{T}_N \mathbf{T}_{N-1} \dots \mathbf{T}_2 \mathbf{T}_1}_{=\mathbf{T}_{System}} \mathbf{J}_1. \quad (2.30)$$

It is convention to write the Jones vectors on a normalized form, such that

$$|E_x|^2 + |E_y|^2 = 1. \quad (2.31)$$

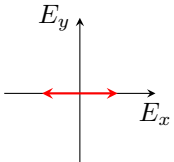
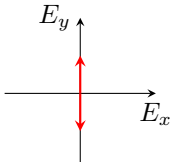
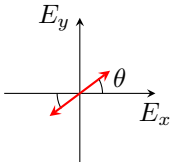
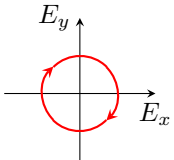
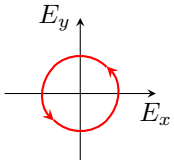
It is also common to drop any prefactors in the Jones vectors or matrices, because they affects each component equally and therefore do not affect the polarization state.

Jones vectors for some important polarization states are given in table 2.2. Jones matrices for a linear polarizer and wave retarder are given in table 2.3, together with the coordinate transformation matrix  $\mathbf{R}(\theta)$ . Transformation between two coordinate systems rotated by an angle  $\theta$  are given by the operations

$$\mathbf{T}' = \mathbf{R}(\theta) \mathbf{T} \mathbf{R}(-\theta) \quad (2.32)$$

$$\mathbf{T} = \mathbf{R}(-\theta) \mathbf{T}' \mathbf{R}(\theta). \quad (2.33)$$

**Table 2.2:** Some important polarization states and associated Jones vectors. Jones vectors taken from [11].

Linear along x	Linear along y	Linear at angle $\theta$
$\mathbf{J} = \begin{bmatrix} 1 \\ 0 \end{bmatrix}$ 	$\mathbf{J} = \begin{bmatrix} 0 \\ 1 \end{bmatrix}$ 	$\mathbf{J} = \begin{bmatrix} \cos \theta \\ \sin \theta \end{bmatrix}$ 
Right-hand circular	Left-hand circular	
$\mathbf{J} = \frac{1}{\sqrt{2}} \begin{bmatrix} 1 \\ j \end{bmatrix}$ 	$\mathbf{J} = \frac{1}{\sqrt{2}} \begin{bmatrix} 1 \\ -j \end{bmatrix}$ 	

**Table 2.3:** Jones matrix for linear polarizer and wave retarder. The coordinate transformation matrix can be applied to transform a Jones matrix in a given coordinate system to another coordinate system rotated by an angle  $\theta$ . This can be done by the transformation  $T' = \mathbf{R}(\theta)\mathbf{T}\mathbf{R}(-\theta)$ , and back again by  $T = \mathbf{R}(-\theta)\mathbf{T}'\mathbf{R}(\theta)$ . If the angle  $\Gamma$  in the wave retarder matrix is  $\pi/2$  or  $\pi/4$ , it acts as a half-wave plate (HWP) or quarter-wave plate (QWP) respectively. Jones matrices taken from [11].

Linear x-polarizer	Wave retarder (fast axis along x)	Coordinate transformation
$\mathbf{T}_{LP} = \begin{bmatrix} 1 & 0 \\ 0 & 0 \end{bmatrix}$	$\mathbf{T}_{WP} = \begin{bmatrix} 1 & 0 \\ 0 & e^{-j\Gamma} \end{bmatrix}$	$\mathbf{R}(\theta) = \begin{bmatrix} \cos \theta & \sin \theta \\ -\sin \theta & \cos \theta \end{bmatrix}$

### 2.3.3 Ellipticity

Measurements of the changes in polarization after interaction with a medium can be used for characterization of certain properties. The medium can induce both a rotation in the polarization, as well as an anisotropic phase shift, which can make a linear polarization elliptical. The ellipticity can be described in terms of the angles  $\Psi$  and  $\chi$ , in reference to figure 2.4.

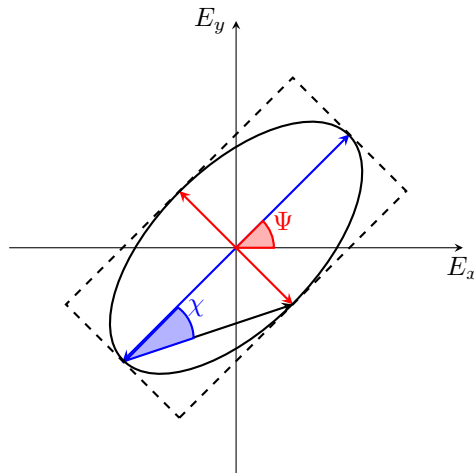


**Figure 2.4:** Polarization ellipse. The polarization state is described by the angles  $\Psi$  which signifies the rotation of the majority axis and the ellipticity angle  $\chi$ , describing the width of the ellipse.

When light propagates through a birefringent medium (see section 2.4.2), the majority axis rotates, and the ellipticity increases. This is described by the rotation transformation described above, and when the phase angle  $\Gamma$  is  $\pi/2$  or  $\pi/4$ , the medium behaves as a quarter wave or half wave retarder respectively, and the linearly polarized light is transformed into a circular polarization.

### 2.3.4 The Kerr Effects - Overview



**Figure 2.5:** John Kerr (1824-1907) [12].

Before moving on to nonlinear optics and magneto-optics, it is pertinent to provide a brief overview of the Kerr effects. Further details on the relevant Kerr effects are provided in appropriate sections later in this chapter. This overview section is intended to alleviate some of the confusion surrounding the Kerr effects, since they differ somewhat in physical origin.

There are in total four optical effects named after the Scottish reverend John Kerr, who is credited with their discovery in the period 1875-1877. These are the optical Kerr effect (OKE/AC Kerr effect) and the electro-optical Kerr effect (DC Kerr effect) [6][5], the magneto-optical Kerr effect (MOKE) [13][8] and the nonlinear magneto-optical Kerr effect (NOLIMOKE/magnetically induced second-harmonic generation (MSHG)) [14]. With the exception of MSHG, all Kerr effects cause a change in the polarization of light after interaction with the medium due to electrically (for the AC/DC Kerr effect) or magnetically (for MOKE) induced birefringence (see 2.4.2). Studies of OKE and MOKE reveal important material characteristics, and they are the key topics for this thesis.

The AC and DC Kerr effects originate under different conditions of third order nonlinear interactions. They occur when a medium is exposed to a strong electric field. When the field is varying rapidly in time (optical), the AC Kerr effect is observed, and when it is static, or varying slowly enough in time, the DC Kerr effect is observed. Nonlinear optics is explained in detail in 2.4. The AC and DC Kerr effects can be observed in all materials, but is usually weak. Certain liquids have been found to produce a stronger response.

The magneto-optical Kerr effect differs from the AC and DC Kerr effects in origin, by being linear in the optical field. Instead, birefringence is caused by interactions between the optical field and the magnetization field  $M$  in the material. MOKE only affects light that is reflected. An analogous effect, called the Faraday effect, works similarly but with transmitted light. MOKE is a weak effect, and is undetectable in most materials, but is much more prominent in ferromagnetic materials. MOKE spectroscopy is a powerful tool

for investigating ferromagnetic materials, because it is highly sensitive and non-invasive. Magneto-optics is further explained in 2.7.

Lastly, the nonlinear magneto-optical Kerr effect is both nonlinear in the optical field, and dependent on  $M$ . It can occur when a strong optical field is reflected from a magnetic surface. Rather than birefringence, MSHG causes generation of second-harmonic light in the medium.

## 2.4 Linear and Nonlinear Optics

### 2.4.1 Introduction

The discipline of nonlinear optics can generally be considered to encompass all optical phenomena in which the strength of the fields play a dominant role. Interactions between light and matter may be divided into linear and nonlinear regimes based on the field strength. Some fundamental differences between linear and nonlinear optics are summarized in table 2.4 [11]. A multitude of exotic phenomena can occur as a result of nonlinear interactions, such as second-harmonic generation, sum- and difference-frequency generation, optical parametric oscillation and the optical Kerr effect, to name a few.

The nonlinearity manifests itself in the relation between the electric field  $E$  and the electric polarization  $P$ . When a medium is exposed to an electric field comparable in magnitude to the inter-atomic or crystalline electric fields,  $P$  begins to deviate from the linear expression in (2.11). Since the electric polarization is the source of the nonlinearity, nonlinear effects can only occur in a medium and not in free-space.

**Table 2.4:** Some key differences between linear and nonlinear optics (summarized from [11]).

Property	Linear Optics	Nonlinear Optics
Refractive index (and speed of light)	Independent of intensity	Dependent of intensity
Absorption coefficient	Independent of intensity	Dependent of intensity
Superposition principle	Valid	Invalid
Frequency of light	Does not change by passage through medium	Can change by passage through a medium
Photon interactions	Photons do not interact; two light beams will not interact with each other	Photons interact within the medium; one light beam can control another

### 2.4.2 Linear Optics

When the applied electric field is sufficiently weak, a medium can be considered linear, and (2.11) holds. The medium is then completely characterized by its electric susceptibility,  $\chi$ , which is a 2nd rank tensor containing 9 elements

$$\chi = \begin{bmatrix} \chi_{11} & \chi_{12} & \chi_{13} \\ \chi_{21} & \chi_{22} & \chi_{23} \\ \chi_{31} & \chi_{32} & \chi_{33} \end{bmatrix}. \quad (2.34)$$

If  $\chi$  is diagonal i.e.  $\chi_{ij} = 0$  for  $i \neq j$ , the induced polarization is always aligned with the field. Additionally, if the non-zero components are all equal, the induced polarization is independent of the polarization of the external field. The medium is hence invariant under coordinate transforms, and the susceptibility may be treated as a constant times the identity matrix [15]

$$\chi = \begin{bmatrix} \chi_{11} & 0 & 0 \\ 0 & \chi_{11} & 0 \\ 0 & 0 & \chi_{11} \end{bmatrix} \quad (2.35)$$

$$= \chi_{11} \mathbf{I}. \quad (2.36)$$

The symmetry properties just described is that of an isotropic medium. For media with more complicated symmetry, the susceptibility tensor may look different. If the diagonal elements are unequal, or if non-zero off-diagonal elements exist, the medium is classified as anisotropic (or birefringent/birefractive). The electric polarization  $\mathbf{P}$  then depends on the polarization of  $\mathbf{E}$ . An electric field polarized along a certain axis may give rise to a perpendicular component in  $\mathbf{P}$ , which can cause rotation and ellipticity of the polarization, in an anisotropic medium.

If the medium is homogeneous ( $\chi$  is independent of position within the medium) and nondispersive ( $\chi$  is independent of time; the medium has no electric memory), the polarization is a linear combination of each vector component of  $\mathbf{E}$

$$P_i = \sum_{j=1,2,3} \epsilon_0 \chi_{ij} E_j. \quad (2.37)$$

When  $\mathbf{P}$  is linear in  $\mathbf{E}$ , the wave equation takes on a simple form; inserting (2.11) into (2.26) yields

$$\nabla^2 \mathbf{E} - \frac{1}{c_0^2} \frac{\partial^2 \mathbf{E}}{\partial t^2} = \epsilon_0 \mu_0 \chi \frac{\partial^2 \mathbf{E}}{\partial t^2} \quad (2.38)$$

$$\nabla^2 \mathbf{E} - \frac{1}{c_0^2} (1 + \chi) \frac{\partial^2 \mathbf{E}}{\partial t^2} = 0 \quad (2.39)$$

$$\boxed{\nabla^2 \mathbf{E} - \frac{n_0^2}{c_0^2} \frac{\partial^2 \mathbf{E}}{\partial t^2} = 0} \quad (2.40)$$

Wave equation,  
linear medium

where  $n_0 \equiv \sqrt{1 + \chi}$  is the refractive index of the medium. The wave equation for a linear, homogeneous, nondispersive medium is identical to the free-space wave equation, with the difference being the velocity of the wave now being  $c = c_0/n_0$ .

### 2.4.3 Nonlinear Optics

When a medium is exposed to an electric field of considerable strength,  $\mathbf{P}$  displays a nonlinear relationship with  $\mathbf{E}$ . The nonlinearity may originate in a nonlinear relationship between the atomic restoring force and the electron displacement from equilibrium (Hooke's law becomes invalid), or in the dependency of the quantum density of states on the electric field strength.

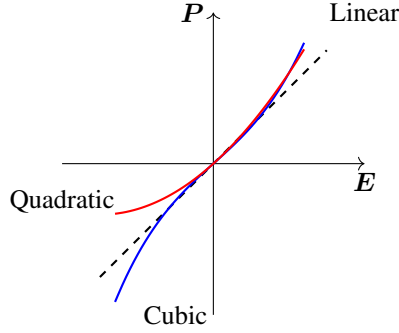


**Figure 2.6:** Illustration of linear, quadratic (second-order) nonlinear and cubic (third-order) nonlinear media. Third-order media behave symmetrically to an applied electric field, while second-order media behave asymmetrically.

Since the deviation from (2.11) is subtle under non-resonant conditions, the nonlinear relationship can be expressed as a Taylor expansion in  $\mathbf{E}$

$$\mathbf{P} = \epsilon_0 \left( \chi^{(1)} \mathbf{E} + \chi^{(2)} \mathbf{E} \mathbf{E} + \chi^{(3)} \mathbf{E} \mathbf{E} \mathbf{E} + \dots \right) \quad (2.41)$$

where  $\chi^{(2)}$  and  $\chi^{(3)}$  denotes the second and third order nonlinear susceptibility respectively<sup>1</sup> (the linear susceptibility is denoted by the superscript (1) to distinguish it from higher-order terms). The nonlinear behavior is illustrated in figure 2.6.

The separate terms in  $\mathbf{P}$  may be addressed individually

$$\mathbf{P} = \mathbf{P}^{(1)} + \mathbf{P}^{(2)} + \mathbf{P}^{(3)} + \dots \quad (2.42)$$

where  $\mathbf{P}^{(1)}$  is the linear term, and  $\mathbf{P}^{(2)}$  and  $\mathbf{P}^{(3)}$  are the second and third-order nonlinear terms respectively. Since all terms in (2.42) are vectors, i.e. 1st rank tensors, and  $\chi^{(1)}$  is a 2nd rank tensor, it follows that  $\chi^{(2)}$  is a 3rd rank tensor and  $\chi^{(3)}$  is a 4th rank tensor. In three-dimensional space,  $\chi^{(2)}$  has 27 elements and  $\chi^{(3)}$  has 81 elements. Individual components of the tensor are denoted  $\chi_{ijk}^{(2)}$  and  $\chi_{ijkl}^{(3)}$ . In the general case, all elements must be considered, but symmetry relations can often be applied to reduce this to a manageable number. This is because many of the elements are zero, and the non-zero elements are not independent.

<sup>1</sup>The nonlinear susceptibilities are sometimes expressed in a different notation, e.g.  $\epsilon_0 \chi^{(2)} \iff 2d$  and  $\epsilon_0 \chi^{(3)} \iff 4\chi^{(3)}$ . Strictly speaking,  $2d$  and  $\epsilon_0 \chi^{(2)}$  are not exactly interchangeable because  $2d$  is on contracted index form.

$\chi^{(2)}$  and  $\chi^{(3)}$  are expected to be numerically small, and their order-of-magnitude can be estimated by considering that nonlinear behavior becomes apparent when the magnitude of the electric field is comparable to the field experienced by the electrons in an atom [5]

$$E_{at} = \frac{e}{4\pi\epsilon_0 a_0^2} \quad (2.43)$$

where  $-e$  is the charge of the electron, and  $a_0$  is the Bohr radius of the hydrogen atom. Under non-resonant conditions, it is expected that  $\chi^{(2)} \approx \chi^{(1)}/E_{at}$  and  $\chi^{(3)} \approx \chi^{(1)}/E_{at}^2$ , and for condensed matter,  $\chi^{(1)}$  is often close to 1. The approximate values in SI-units are

$$\chi^{(2)} \approx 1.94 \times 10^{-12} \text{ m/V}$$

and

$$\chi^{(3)} \approx 3.78 \times 10^{-24} \text{ m}^2/\text{V}^2$$

which turns out to be reasonably close to values measured for the nonlinear susceptibilities.

Three terms were included in the Taylor expansion (2.41). This is usually sufficient to explain the most prominent nonlinear processes (although sometimes higher order terms must be included as well). The first term contains the linear susceptibility, and (2.11) reduces to (2.41) when the applied field is weak. The second term contains the second-order nonlinear susceptibility and is the origin of e.g. second-harmonic generation (SHG) and the Pockel's effect (see section 2.4.4). The third term contains the third-order nonlinear susceptibility and is the origin of e.g. third harmonic generation (THG) and the optical Kerr effect (OKE). This is explained in further detail in the next sections. If the medium belongs to a point group with inversion symmetry (i.e. a centrosymmetric medium) the second term vanishes identically and the nonlinear behavior is dominated by third-order effects. Media which display second-order behavior are called non-centrosymmetric.

It is convenient to separate the linear and nonlinear contributions in (2.41)

$$\mathbf{P} = \mathbf{P}^{(1)} + \mathbf{P}^{NL} \quad (2.44)$$

$$= \underbrace{\epsilon_0 \chi^{(1)} \mathbf{E}}_{\text{Linear}} + \underbrace{\mathbf{P}^{NL}}_{\text{Nonlinear}} \quad (2.45)$$

where

$$\mathbf{P}^{NL} = \underbrace{\epsilon_0 \chi^{(2)} \mathbf{E} \mathbf{E}}_{\text{Second order}} + \underbrace{\epsilon_0 \chi^{(3)} \mathbf{E} \mathbf{E} \mathbf{E}}_{\text{Third order}}. \quad (2.46)$$

When the nonlinear polarization is included in the wave equation for a non-magnetic, non-conductive medium (2.26), the linear component can be contracted in the refractive index

$$\boxed{\nabla^2 \mathbf{E} - \frac{n_0^2}{c_0^2} \frac{\partial^2 \mathbf{E}}{\partial t^2} = \mu_0 \frac{\partial^2 \mathbf{P}^{NL}}{\partial t^2}} \quad (2.47)$$

Wave equation,  
nonlinear medium

such that the left-hand side of the equation is identical to the wave equation for a linear medium (2.40), with the inclusion of a source-term on the right-hand side that has origin in the nonlinearity.

The source-term  $\mu_0 \frac{\partial^2 \mathbf{P}^{NL}}{\partial t^2}$  is a nonlinear function of  $\mathbf{E}$ . This causes the medium to radiate an electric field, which in turn affects the source. This suggests that the nonlinear wave equation must be solved iteratively, as shown schematically in figure 2.7. Appendix A shows a numerical solution to the nonlinear wave equation where  $\chi^{(1)}$  and  $\chi^{(2)}$  has been included. The resulting electric field contains a component at  $2\omega$ , which is caused by second-harmonic generation.

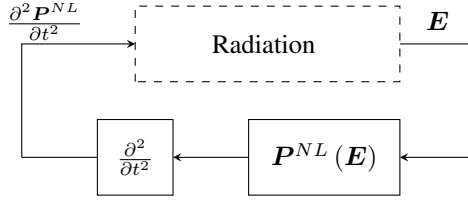


**Figure 2.7:** Schematic illustration of the nonlinear wave equation.

## 2.4.4 Second-Order Effects

In appendix A it is shown that a second-harmonic component of the electric field emerges from the nonlinear wave equation when  $\chi^{(2)}$  is included in the polarization, i.e.

$$\mathbf{P} = \epsilon_0 \chi^{(1)} \mathbf{E} + \epsilon_0 \chi^{(2)} \mathbf{E} \mathbf{E}. \quad (2.48)$$

This can be justified mathematically by considering plane waves in one dimension, propagating in a second-order nonlinear medium. In one-dimension, the fields can be treated as scalars, and the real electric field can be expressed as the real part of a complex phasor. To be general, we consider two waves at frequencies  $\omega_1$  and  $\omega_2$ , and treat the second-order process as a three-wave mixing process

$$E(z, t) = \text{Re}\{E_{10}e^{i(\omega_1 t - k_1 z)} + E_{20}e^{i(\omega_2 t - k_2 z)}\}. \quad (2.49)$$

By considering a fixed coordinate in  $z$ , the space-dependence may be contracted in the complex amplitude (denoted by the tilde sign)

$$E(t) = \text{Re}\{\tilde{E}_{10}e^{i\omega_1 t} + \tilde{E}_{20}e^{i\omega_2 t}\} \quad (2.50)$$

$$= \frac{1}{2} \left( \tilde{E}_{10}e^{i\omega_1 t} + \tilde{E}_{20}e^{i\omega_2 t} + c.c. \right) \quad (2.51)$$

where c.c. denotes the complex conjugate.

The nonlinear polarization is then



$$P^{(2)}(t) = \epsilon_0 \chi^{(2)} E(t)^2 \quad (2.52)$$

$$= \epsilon_0 \chi^{(2)} \left[ \frac{1}{2} \left( \tilde{E}_{10} e^{i\omega_1 t} + \tilde{E}_{20} e^{i\omega_2 t} + c.c. \right) \right]^2 \quad (2.53)$$

$$= \epsilon_0 \chi^{(2)} \frac{1}{4} \left[ |\tilde{E}_{10}|^2 e^{i2\omega_1 t} + |\tilde{E}_{20}|^2 e^{i2\omega_2 t} \right. \quad (2.54)$$

$$\left. + 2\tilde{E}_{10}\tilde{E}_{20}e^{i(\omega_1+\omega_2)t} + 2\tilde{E}_{10}\tilde{E}_{20}^*e^{i(\omega_1-\omega_2)t} \right. \quad (2.55)$$

$$\left. + |\tilde{E}_{10}|^2 + |\tilde{E}_{20}|^2 + c.c. \right]. \quad (2.56)$$

Frequency components arise at

$$2\omega_1, 2\omega_2, \omega_1 \pm \omega_2, 0$$

and the negative of each frequency. They are respectively called

- $2\omega_1$  and  $2\omega_2$ : Second-harmonic generation (SHG)
- $\omega_1 + \omega_2$ : Sum-frequency generation (SFG)
- $\omega_1 - \omega_2$ : Difference-frequency generation (DFG)
- 0: Optical rectification (OR)

The nonlinear polarization is the sum of all involved frequencies, weighted by their Fourier coefficients

$$P^{(2)}(t) = \sum_n \frac{1}{2} \tilde{P}^{(2)}(\omega_n) e^{-i\omega_n t} \quad (2.57)$$

where  $n$  is taken over positive and negative integers, because negative frequencies are included.

When  $\omega_1 = \omega_2 = \omega$ , the sum and difference-frequencies reduce to  $2\omega$ ,  $-2\omega$  and 0, and the summation in (2.57) is easily resolved

$$P^{(2)}(t) = \underbrace{\text{Re}\{\tilde{P}^{(2)}(2\omega)e^{i2\omega t}\}}_{\text{SHG}} + \underbrace{\text{Re}\{\tilde{P}^{(2)}(0)\}}_{\text{OR}} \quad (2.58)$$

where

$$\tilde{P}^{(2)}(2\omega) = \tilde{P}^{(2)}(0) = \frac{1}{2} \epsilon_0 \chi^{(2)} |\tilde{E}_0|^2 \quad (2.59)$$

and

$$\tilde{E}_0 = \tilde{E}_{10} + \tilde{E}_{20}. \quad (2.60)$$

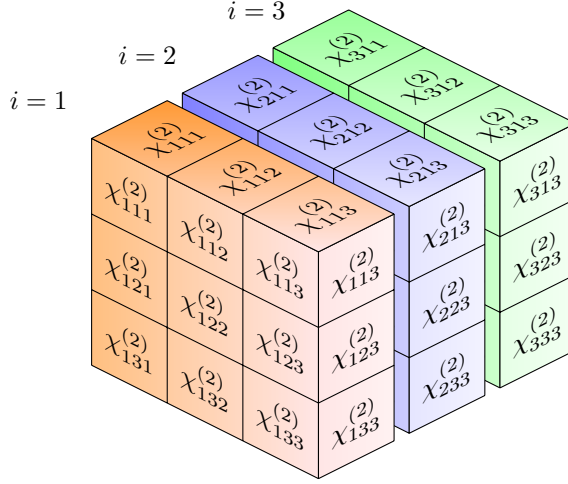


**Figure 2.8:** Illustration of the 27 elements in the  $\chi^{(2)}$  tensor. Each colored slice can be considered a 2nd rank tensor, i.e. a regular matrix. When a specific vector component  $i$  of  $\mathbf{P}^{(2)}$  is considered (i.e.  $P_i^{(2)}$ ), the tensor is reduced to the matrix with the corresponding index (shown here by the different colors).

When the electric field is static, the optical rectification is called Pockels effect.

This derivation, and the numerical solution presented in appendix A, were based on a simplified formalism where  $\chi^{(2)}$ ,  $\mathbf{E}$  and  $\mathbf{P}$  are treated as one-dimensional, scalar quantities. In reality,  $\mathbf{E}$  and  $\mathbf{P}$  must be treated as vectors, while  $\chi^{(2)}$  must be treated as a 3rd rank tensor in three-dimensional space. Figure 2.8 shows a three-dimensional representation of this tensor. Additionally,  $\chi^{(2)}$  is not frequency independent, but depends on the frequencies of all participating waves. Thus, in order to fully compensate for the structural dependence of nonlinear processes, the equations for the polarization should be written on vector/tensor form.

A general form of the second-order process can be written as [6]

$$P_i^{(2)}(\omega_3) = \epsilon_0 K_2(\omega_3; \omega_1, \omega_2) \sum_{jk} \chi_{ijk}^{(2)}(\omega_3; \omega_1, \omega_2) E_j(\omega_1) E_k(\omega_2) \quad (2.61)$$

where the sum is taken over all combinations  $j = 1, 2, 3$  and  $k = 1, 2, 3$  (corresponding to  $x, y, z$  components) of the electric field, and the subscript  $i$  corresponds to the component of the polarization. Furthermore,  $K_2$  is given by

$$K_2(\omega_3; \omega_1, \omega_2) = \frac{1}{2} p_{12} 2^{r-l} \quad (2.62)$$

where the components of  $K_2$  originate in the following way:

- The factor  $\frac{1}{2}$  is the same that appears in (2.51), and originates in the complex definition of the fields.

- $p_{12}$  is the number of distinct permutations of  $\omega_1$  and  $\omega_2$ .  $p_{12} = 1$  if  $\omega_1 = \omega_2$  and  $p_{12} = 2$  if  $\omega_1 \neq \omega_2$ . The factor  $p_{12}$  is in some cases written as an extra sum over the permutations  $\sum_p$ .
- $l$  and  $r$  is the number of zero frequency component to the left and right of the semicolon respectively. This is necessary, because special care has to be taken when zero frequency components are present in a nonlinear process.

$K^2$  is indeed a measure of the degeneracy of the process, and is in some literature written instead as  $D^2$ .

The notation used for  $\chi_{ijk}^{(2)}$  deserves special attention; the three frequency arguments in the parenthesis correspond to the individual frequency components of the participating waves. The first argument (to the left of the semicolon) corresponds to the frequency of the polarization, while the other two correspond to the participating electric fields. The relation  $\omega_3 = \omega_1 + \omega_2$  is always fulfilled, so only two frequency arguments are strictly required. It is nevertheless common to include all three. Second-order processes are, as previously stated, a form of three-wave mixing, and both positive and negative frequencies must be included to fully account for that.

Second-harmonic generation can be considered a special case of (2.61) with  $\omega_1 = \omega_2 = \omega$ . (2.61) is then reduced to

$$P_i^{(2)}(2\omega) = \frac{1}{2}\epsilon_0 \sum_{jk} \chi_{ijk}^{(SHG)}(2\omega; \omega, \omega) E_j(\omega) E_k(\omega) \quad (2.63)$$

since  $K_2 = \frac{1}{2}$  in this case.

The vector/tensor form is particularly important in third-order processes and is further explained in the next section.

### 2.4.5 Third-Order Effects

The even components in (2.42) vanish within the bulk region of centrosymmetric media<sup>2</sup>, and nonlinear effects are dominated by  $P^{(3)}$ . The polarization of the medium is then given by

$$\mathbf{P} = \epsilon_0 \chi^{(1)} \mathbf{E} + \epsilon_0 \chi^{(3)} \mathbf{E} \mathbf{E} \mathbf{E}. \quad (2.64)$$

As with SHG, we initially consider scalar, one-dimensional fields. If the electric field is comprised of three waves at frequencies  $\omega_1$ ,  $\omega_2$  and  $\omega_3$ , i.e.

$$E(t) = \text{Re}\{\tilde{E}_{10}e^{i\omega_1 t} + \tilde{E}_{20}e^{i\omega_2 t} + \tilde{E}_{30}e^{i\omega_3 t}\} \quad (2.65)$$

$$= \frac{1}{2} \left( \tilde{E}_{10}e^{i\omega_1 t} + \tilde{E}_{20}e^{i\omega_2 t} + \tilde{E}_{30}e^{i\omega_3 t} + c.c. \right) \quad (2.66)$$

where *c.c.* is the complex conjugate, the nonlinear polarization is

---

<sup>2</sup>In general, all nonlinear effects are always present within a medium. This is also true for centrosymmetric media, because the symmetry is always broken at the medium interface. It is however possible to isolate particular effects by experimental considerations.

$$P^{(3)}(t) = \epsilon_0 \chi^{(3)} E(t)^3 \quad (2.67)$$

$$= \epsilon_0 \chi^{(3)} \left[ \frac{1}{2} \left( \tilde{E}_{10} e^{i\omega_1 t} + \tilde{E}_{20} e^{i\omega_2 t} + \tilde{E}_{30} e^{i\omega_3 t} + c.c. \right) \right]^3. \quad (2.68)$$

By resolving the third power multiplication of  $E(t)$ , one finds that a total of 44 frequency components appears in the equation:

$$\begin{aligned} &\omega_1, \omega_2, \omega_3, 3\omega_1, 3\omega_2, 3\omega_3, (\omega_1 + \omega_2 + \omega_3), (\omega_1 + \omega_2 - \omega_3), (\omega_1 + \omega_3 - \omega_2), \\ &(\omega_2 + \omega_3 + \omega_1), (2\omega_1 \pm \omega_2), (2\omega_1 \pm \omega_3), (2\omega_2 \pm \omega_1), (2\omega_2 \pm \omega_3), (2\omega_3 \pm \omega_1), \\ &(2\omega_3 \pm \omega_2) \end{aligned}$$

along with the negative of each frequency. This demonstrates the complicated nature of third-order interactions, and many non-linear effects originate in this wave-mixing process (in contrast, only 9 frequency components were generated in the second-order three-wave mixing process). The Fourier expansion of the third-order process is

$$P^{(3)}(t) = \sum_n \frac{1}{2} \tilde{P}^{(3)}(\omega_n) e^{-i\omega_n t} \quad (2.69)$$

where  $n$  is taken over positive and negative integers.

When  $\omega_1 = \omega_2 = \omega_3 = \omega$ , the total number of frequencies is reduced to 4:  $\omega$ ,  $-\omega$ ,  $3\omega$  and  $-3\omega$ . The summation in (2.69) can then be resolved

$$P^{(3)}(t) = \underbrace{\text{Re}\{\tilde{P}^{(3)}(3\omega)e^{i3\omega t}\}}_{\text{THG}} + \underbrace{\text{Re}\{\tilde{P}^{(3)}(\omega)e^{i\omega t}\}}_{\text{IDRI/OKE}} \quad (2.70)$$

i.e. waves at frequency  $\omega$  and  $3\omega$ . The  $3\omega$  wave is known as third-harmonic generation (THG), and is a clear analogy to SHG. The conversion rate for THG is usually quite low, and the effect is not as commonly utilized for generation of higher frequencies as SHG. The frequency-component at  $\omega$  is however quite significant, and reveals a relationship between  $P^{(3)}$  and the refractive index. This effect is known as intensity-dependent refractive index (IDRI) when a single wave modulates its own refractive index as it propagates through a medium, and the optical Kerr effect (OKE) when one wave changes the refractive index of another wave in the same medium. IDRI and OKE are further discussed in the next section.

As with the second-order interactions discussed in the previous section, third-order interactions are further complicated by the vector/tensor form.  $\chi^{(3)}$  is a 4th rank tensor which in three-dimensional space consists of 81 elements.

Similarly to (2.61), a general form of the third-order process can be written as [6]

$$P_i^{(3)}(\omega_4) = \epsilon_0 K_3(\omega_4; \omega_3, \omega_2, \omega_1) \sum_{jkl} \chi_{ijkl}^{(3)}(\omega_4; \omega_1, \omega_2, \omega_3) E_j(\omega_1) E_k(\omega_2) E_l(\omega_3) \quad (2.71)$$

where

$$K_3(\omega_4; \omega_3, \omega_2, \omega_1) = \frac{1}{2} p_{123} 2^{r-l} \quad (2.72)$$

which is analogous to the degeneracy factor for the second-order process (the only difference being that  $p_{123}$  is the number of distinct permutations of  $\omega_1, \omega_2$  and  $\omega_3$ ).

In the case of IDRI, (2.71) can be expressed as

$$P_i^{(3)}(\omega) = \frac{3}{4} \epsilon_0 \sum_{jkl} \chi_{ijkl}^{IDRI}(\omega; \omega, -\omega, \omega) E_j(\omega) E_k^*(\omega) E_l(\omega) \quad (2.73)$$

and in the case of OKE (with  $E(\omega_1)$  as probe,  $E(\omega_2)$  as pump), as

$$P_i^{(3)}(\omega_1) = \frac{3}{2} \epsilon_0 \sum_{jkl} \chi_{ijkl}^{OKE}(\omega_1; \omega_2, -\omega_2, \omega_1) E_j(\omega_2) E_k^*(\omega_2) E_l(\omega_1). \quad (2.74)$$

## 2.4.6 Intensity-Dependent Refractive Index (IDRI) and the Optical Kerr Effect (OKE)

When only one wave is involved,  $\tilde{P}^{(3)}(\omega)$  is given by [5]

$$\tilde{P}^{(3)}(\omega) = \frac{3}{4} \epsilon_0 \chi^{(3)}(\omega; \omega, -\omega, \omega) |\tilde{E}(\omega)|^2 \tilde{E}(\omega) \quad (2.75)$$

where one of the frequency arguments is chosen to be negative such that  $\omega_4 = \omega_1 + \omega_2 + \omega_3$  is fulfilled.

The total (linear and nonlinear) polarization at  $\omega$  is then

$$P(\omega) = \epsilon_0 \chi^{(1)} \tilde{E}(\omega) + \frac{3}{2} \epsilon_0 \chi^{(3)} |\tilde{E}(\omega)|^2 \tilde{E}(\omega) \quad (2.76)$$

$$= \epsilon_0 \left( \chi^{(1)} + \frac{3}{2} \chi^{(3)} |\tilde{E}(\omega)|^2 \right) \tilde{E}(\omega) \quad (2.77)$$

$$= \epsilon_0 \chi_{eff} \tilde{E}(\omega) \quad (2.78)$$

where

$$\chi_{eff} = \chi^{(1)} + \frac{3}{2} \chi^{(3)} |\tilde{E}(\omega)|^2 \quad (2.79)$$

is the effective susceptibility. This effectively causes the linear susceptibility, and inherently, the refractive index, to be modified

$$n^2 = 1 + \chi_{eff} \quad (2.80)$$

where

---

$$n = n_0 + 2\bar{n}_2|\tilde{E}(\omega)|^2 \quad (2.81)$$

$$= n_0 + \bar{n}_2\langle E^2(t) \rangle. \quad (2.82)$$

$n_0$  is the regular linear refractive index, and  $\bar{n}_2$  is called the second-order refractive index (although it originates in a third-order process)

$$\bar{n}_2 = \frac{3\chi^{(3)}}{4n_0}. \quad (2.83)$$

The term  $\langle E^2(t) \rangle$  in (2.82) symbolizes the time-average of the electric field, related to the absolute value of the amplitude by  $\langle E^2(t) \rangle = 2\tilde{E}(\omega)\tilde{E}^*(\omega) = 2|\tilde{E}(\omega)|^2$ .

Since  $\langle E^2(t) \rangle \propto I$  (the optical intensity) (2.82) can be expressed as

$$\boxed{n = n_0 + n_2 I} \quad (2.84)$$

Intensity-dependent  
refractive index

where

$$\boxed{n_2 = \frac{\bar{n}_2}{n_0\epsilon_0 c} = \frac{3\chi^{(3)}}{4n_0^2\epsilon_0 c_0}}. \quad (2.85)$$

Second-order index  
of refraction (IDRI)

Since the refractive index of the medium changes as a function of the optical intensity, it is possible for one wave to change the propagation of another. It is even possible for one part of a light pulse to modify the propagation of a latter part of the same pulse. This enables modulation of a light wave by means of another wave, a feat that is impossible in a linear medium. The process in which a strong beam of light modulates a weak is referred to as the optical Kerr effect (OKE). Other commonly used names are AC Kerr effect, cross-phase modulation (XPM) and weak-wave retardation. The strong and weak beams are referred to as pump and probe respectively. In order to be physically distinguishable, they must naturally have different direction of propagation.

If  $E(\omega_1)$  is the probe beam and  $E(\omega_2)$  is the pump beam, (2.75) can be rewritten as

$$P^{(3)}(\omega_1) = \frac{3}{2}\epsilon_0\chi^{(3)}(\omega_1; \omega_2, -\omega_2, \omega_1)|E(\omega_2)|^2 E(\omega_1) \quad (2.86)$$

where the degeneracy factor is twice as large since the two beams are distinguishable. The refractive index is then

$$n = n_0 + 2\bar{n}_2^X |E(\omega)|^2 \quad (2.87)$$

where

$$\bar{n}_2^X = \frac{3\chi^{(3)}}{2n_0}. \quad (2.88)$$

In terms of intensity, OKE is expressed as

$$n = n_0 + n_2^X I \quad (2.89)$$

Optical Kerr Effect

where

$$n_2^X = \frac{\bar{n}_2^X}{n_0 \epsilon_0 c} = \frac{3\chi^{(3)}}{2n_0^2 \epsilon_0 c_0}. \quad (2.90)$$

Second-order index  
of refraction (OKE)

Note that IDRI can be considered a special case of OKE, when the pump and probe beams are one and the same. IDRI and OKE are illustrated in figure 2.9. The second-order index of refraction is typically on the order of  $10^{-10} \text{ cm}^2/\text{W}$  to  $10^{-18} \text{ cm}^2/\text{W}$ , and requires high-intensity light to be observable.

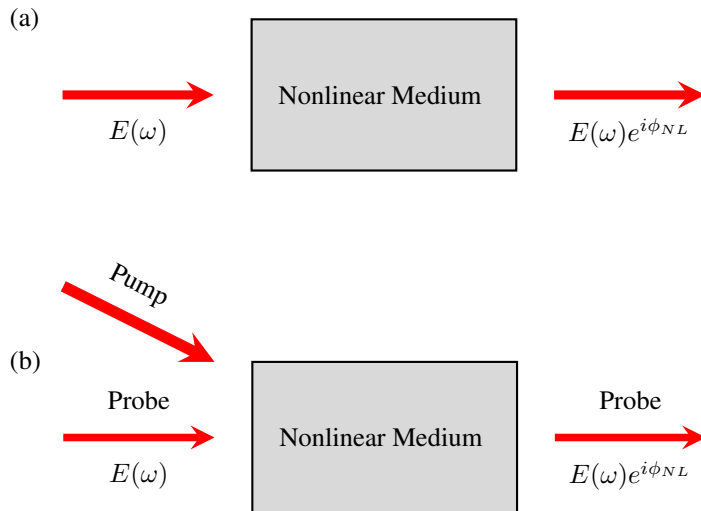


**Figure 2.9:** Illustration of phase modulation within a third-order nonlinear medium. The phase is modulated because (a) the intensity of the beam is strong enough to alter its own refractive index, (b) a pump beam alters the refractive index for a weak beam, assumed too weak to alter its own refractive index. Intensity is indicated by the thickness of the arrows.

## 2.4.7 Nonlinear Optics in the Time-Domain

In this section, the nonlinear response functions are examined in the time-domain. Ambiguity arises in the derivations of some of the previous equations, due to the implicit transitions between the time-domain and the frequency domain. Initially, the polarization response was assumed to instantaneously follow the electric field. A scalar treatment of the susceptibilities was therefore valid in the time-domain. This property is however never realized in physical systems, and the non-instantaneous response function must be introduced to account for this.

Equations (2.63), (2.73) and (2.74) are examples of equations that are neither frequency-domain equations, nor true time-domain equations. Instead, they appear as equations on the *hybrid* form, in the terminology of New [6]. In the hybrid form, the notation  $E(\omega)$  refers to an electric field in the time-domain of a narrow frequency band around  $\omega$ . The unit of the  $n$ th order susceptibility is  $(\text{m/V})^{n-1}$ , and the unit of the electric fields are  $\text{V/m}$  which makes it a time-domain equation. The hybrid form is canonical in the literature (see e.g. [11], [6] or [5]), but is not always explicitly disclosed.

For each polarization response equation in the frequency-domain, there exists a corresponding time-domain equation, in which the multiplication of the susceptibility tensor elements with the fields in the frequency-domain is replaced with the convolution of the impulse response function and the fields in the time-domain.

The time-domain equations, in the nomenclature of Butcher and Cotter, are as follows [16]

- The linear response:

$$\mathbf{P}^{(1)}(t) = \epsilon_0 \int_{-\infty}^{\infty} d\tau \mathbf{R}^{(1)}(t - \tau) \cdot \mathbf{E}(\tau) \quad (2.91)$$

- The second-order response:

$$\mathbf{P}^{(2)}(t) = \epsilon_0 \int_{-\infty}^{\infty} d\tau_1 \int_{-\infty}^{\infty} d\tau_2 \mathbf{R}^{(2)}(t - \tau_1, t - \tau_2) : \mathbf{E}(\tau_1) \mathbf{E}(\tau_2) \quad (2.92)$$

- The third-order response:

$$\mathbf{P}^{(3)}(t) = \epsilon_0 \int_{-\infty}^{\infty} d\tau_1 \int_{-\infty}^{\infty} d\tau_2 \int_{-\infty}^{\infty} d\tau_3 \mathbf{R}^{(3)}(t - \tau_1, t - \tau_2, t - \tau_3) : \quad (2.93)$$

$$\mathbf{E}(\tau_1) \mathbf{E}(\tau_2) \mathbf{E}(\tau_3)$$

The susceptibilities  $\chi^{(n)}$  are replaced with their corresponding time-domain response functions  $\mathbf{R}^{(n)}$ .

The necessity for the time-domain equations become obvious when time-resolved spectroscopy is discussed in chapter 3.



## 2.5 Quantum Mechanics

### 2.5.1 Introduction

The physical origin of nonlinear optics was largely overlooked in section 2.4. Instead, it was attributed solely to the Taylor expansion of the polarization vector. This model accurately describes the nonlinear susceptibility off-resonance, but fails to account for material resonance effects. A more complete theory is provided by time-dependent perturbation theory within the quantum mechanical framework. The results derived in this section provide a way of interpenetrating the time-dependence of the nonlinear susceptibilities. Matter is treated quantum mechanically with the density matrix formalism, and the fields classically, as a perturbation of the system. This interaction model belongs to the discipline of physics known as quantum electronics. It is shown that electromagnetic waves alter the properties of the material and induce virtual energy levels. These levels give rise to energy transitions which is addressed in terms of absorption and emission of individual photons.

The next sections primarily follow the quantum theory found in chapter 5, 8 and 9 of New [6], with complimentary theory of the density matrix from Pantell and Puthoff [15].

### 2.5.2 Basic Concepts

An atomic state may be described by its wave function  $\psi$ , that is postulated to contain all information that can be known about a system. In the Dirac formalism, the state may be represented by the ket-vector  $|\psi\rangle$  in the abstract Hilbert space, and its complex conjugate, the bra-vector  $\langle\psi|$ . Operators are used to transform a state vector into another. An operator  $\hat{A}$  may act on a vector  $|v\rangle$  to produce a new vector  $|w\rangle$ ;

$$|w\rangle = \hat{A}|v\rangle. \quad (2.94)$$

The state vector is related to the wave function by the bra-ket integral for an operator  $\hat{A}$

$$\int u^* \hat{A}v \, dV = \langle u|\hat{A}|v\rangle. \quad (2.95)$$

The product of a bra and ket vector represents the integral

$$\int u^* v \, dV = \langle u|v\rangle \quad (2.96)$$

and is termed the scalar product, or the inner product. It has the following properties:

$$\langle u|v\rangle = \langle v|u\rangle^* \quad (2.97)$$

$$\langle u|u\rangle \geq 0. \quad (2.98)$$

The state vectors are, in the non-relativistic case, eigenvectors of the Schrödinger equation

$$\hat{H}|\psi\rangle = i\hbar \frac{\partial |\psi\rangle}{\partial t} \quad (2.99)$$

where  $\hat{H} = \hat{H}_0 + \hat{V}$  is the Hamiltonian operator, and contains both the unperturbed Hamiltonian  $\hat{H}_0$  and a perturbation Hamiltonian  $\hat{V}$  (alternatively written  $\hat{H}'$ ). Within the dipole approximation, the perturbation can be written as

$$\hat{V} = -\hat{\boldsymbol{\mu}} \cdot \mathbf{E} = e\hat{\mathbf{r}} \cdot \mathbf{E} \quad (2.100)$$

where  $e$  is the elementary charge and  $\hat{\boldsymbol{\mu}}$  is the dipole operator.

### 2.5.3 The Two-Level System

The density matrix  $\rho$  is an equivalent representation of the wave function, that allows transition between the quantum mechanical formalism, and the equations of motion associated with a particular experiment. The density matrix is widely used in nonlinear optics to provide a quantum mechanical description for the nonlinear (as well as linear) interactions. In short, the density matrix contains the probability amplitudes for the states of the system. Unlike the more traditional expansion coefficient associated with the eigenstates of a *pure state*, the coefficients in the density matrix incorporate statistical averaging over all eigenstates in a *mixed state*. A state is said to be pure, if all atoms/molecules are in the same quantum state, otherwise it is mixed. A more detailed explanation of the density matrix is given in appendix B.

Some important properties of the density matrix:

1. The expectation value of an operator  $\hat{A}$  is found by the *trace* of the matrix product of the density matrix and the operator

$$\langle A \rangle = Tr(\hat{A}\rho) \quad (2.101)$$

The trace is the sum of diagonal elements, i.e.

$$\langle A \rangle = \sum_{ij} A_{ji}\rho_{ij}. \quad (2.102)$$

2. The density matrix evolves in time according to

$$i\hbar \frac{\partial \rho}{\partial t} = [\hat{H}, \rho] \quad (2.103)$$

where the right-hand side denotes the commutator of the Hamiltonian and the density matrix.

3. The density matrix is Hermitian

$$\rho_{ij} = \rho_{ji}^*. \quad (2.104)$$

4. The density matrix is normalized

$$Tr(\rho) = 1. \quad (2.105)$$

Figure 2.10 shows a simple two-level system. The density matrix can be expressed as a 2-by-2 matrix for this system

$$\rho = \begin{bmatrix} \rho_{00} & \rho_{01} \\ \rho_{10} & \rho_{11} \end{bmatrix} = \begin{bmatrix} |a_0|_{\bar{}}^2 & a_0 \bar{a}_1^* \\ a_1 \bar{a}_0^* & |a_1|_{\bar{}}^2 \end{bmatrix} \quad (2.106)$$

where the overbar denotes averages over the ensemble and  $a_n$  is the probability amplitude of the  $n$ th state.



**Figure 2.10:** Simple two-level system.

In thermal equilibrium, the diagonal elements of the density matrix follow the Boltzmann distribution

$$\rho_{ii} = \frac{e^{-E_i/\kappa T}}{e^{\sum_m E_m/\kappa T}} \quad (2.107)$$

where  $T$  is the temperature, and  $\kappa$  is the Boltzmann constant. The off-diagonal elements are zero in thermal equilibrium. Relaxation processes act to redistribute the population of states and allow the system to reach thermal equilibrium with its environment. The Hamiltonian can be expressed in terms of the unperturbed Hamiltonian  $\hat{H}_0$  and an energy operator  $\hat{H}_1$  for the interaction between the medium and the perturbation (e.g. by an electromagnetic field). The perturbation Hamiltonian can further be divided into a term for the interaction and a randomizing term corresponding to interactions between e.g. the atom and lattice;  $\hat{H}_1 = \hat{H}' + \hat{H}^r$ . When the interaction is absent, the off-diagonal terms evolve in time according to

$$i\hbar \frac{\partial \rho_{ij}}{\partial t} = -\hbar\omega_{ij}\rho_{ij} + [\hat{H}', \rho]_{ij} - \frac{i\hbar}{\tau_{ij}}\rho_{ij} \quad (2.108)$$

and the diagonal terms by

$$i\hbar \frac{\partial \rho_{ii}}{\partial t} = [\hat{H}', \rho]_{jj} + \frac{i\hbar}{T_1}(\rho_{jj}^e - \rho_{jj}) \quad (2.109)$$

where  $\rho_{jj}^e$  is the equilibrium value of the matrix element. For the two-level system, there are two time-constants to consider: the time-constant for the diagonal elements  $T_{12}$ , and for the off-diagonal elements  $\tau_{12}$ .  $T_{12}$  is generally written  $T_1$  and is the time-constant of the decay back to thermal equilibrium in the absence of a perturbation.  $\tau_{12}$  is generally written  $T_2$  and is associated with the linewidth of a transition.  $T_1$  is called the longitudinal,

spin-lattice, or dipole-lattice relaxation time, and  $T_2$  is called the transverse, dipole-dipole, or spin-spin relaxation time. A connection clearly exist between the transient responses measured in pump-probe spectroscopy and the time-evolution of the density matrix. This is however outside the scope of this thesis (see e.g. [17]).

The density matrix is related to the susceptibilities introduced in previous sections through the dipole operator  $\hat{\mu}$ . The expectation value of the dipole operator is  $\langle \mu \rangle = Tr(\hat{\mu}\rho)$ , to which the classical polarization vector used in previous sections is directly related by

$$\boxed{P = N \langle \mu \rangle} \quad (2.110)$$

where  $N$  is the total atomic/molecular number density. In the simplest two-level system, only off-diagonal elements are non-zero (which is true if the system lacks a static electric dipole moment, such as in the ground state of atoms)

$$\hat{\mu} = \begin{bmatrix} 0 & \mu_{01} \\ \mu_{10} & 0 \end{bmatrix}. \quad (2.111)$$

The polarization vector is in this case

$$P = N \langle \mu \rangle = N (\rho_{01}\mu_{10} + \rho_{10}\mu_{01}) \quad (2.112)$$

The resulting polarization vector is obviously independent of any external electric field, since we assumed the system was unperturbed. The polarization contains only off-diagonal terms of the density matrix which are zero at thermal equilibrium.

When the system is subject to a perturbation in the form of an electromagnetic field, the Hamiltonian is given by (2.100). The amplitude coefficients evolve in time according to

$$i\hbar \frac{\partial a_n}{\partial t} = \hbar\omega_n a_n + \sum_l V_{nl} a_l \quad (2.113)$$

where  $V_{nl} = \langle n | \hat{V} | l \rangle$  is the perturbation matrix element. From (2.100), it follows that

$$V_{ln} = -(\langle x \rangle_{ln} E_x + \langle y \rangle_{ln} E_y + \langle z \rangle_{ln} E_z) \quad (2.114)$$

where the notation  $\langle j \rangle_{ln} = \mu_{ln}^j$  is used for the  $j$ th Cartesian coordinate of the dipole moment.

By applying a first-order perturbation with zeroth order solutions  $a_0^{(0)} = 1$  and  $a_1^{(0)} = 0$  (i.e. all atoms are in the ground state) and a driving, single-harmonic electric field

$$E_j = \frac{1}{2} \left( \hat{E}_j e^{i\omega t} + c.c. \right) \quad (2.115)$$

the perturbation reads

$$V_{10} = -\frac{1}{2} \sum_j \langle j \rangle_{10} \left( \hat{E}_j e^{i\omega t} + c.c. \right) \quad (2.116)$$

summed over  $j = x, y, z$ . Integration of (2.113) with respect to time yields

$$a_1^{(1)} = \frac{1}{2\hbar} \sum_j \langle j \rangle_{10} \left( \frac{\hat{E}_j e^{i\omega t}}{\omega_{10} + \omega} + \frac{\hat{E}_j^* e^{-i\omega t}}{\omega_{10} - \omega} \right) \quad (2.117)$$

and in terms of the density matrix,

$$\rho_{10}^{(1)} = \rho_{01}^{(1)*} = \frac{1}{2\hbar} \sum_j \langle j \rangle_{10} \left( \frac{\hat{E}_j e^{i\omega t}}{\tilde{\omega}_{10} + \omega} + \frac{\hat{E}_j^* e^{-i\omega t}}{\tilde{\omega}_{10} - \omega} \right) \quad (2.118)$$

where dampening is included in the complex frequency  $\tilde{\omega}_{10} = \omega_{10} - i\gamma_{10}$ .

With the perturbation of the electromagnetic wave, the polarization reads

$$P_i = N \left( \rho_{01}^{(1)} \langle i \rangle_{10} + \rho_{10}^{(1)} \langle i \rangle_{01} \right) \quad (2.119)$$

$$= \frac{N}{2\hbar} \sum_j \underbrace{\left( \frac{\langle j \rangle_{01} \langle i \rangle_{10}}{\tilde{\omega}_{10}^* - \omega} + \frac{\langle i \rangle_{01} \langle j \rangle_{10}}{\tilde{\omega}_{10} + \omega} \right)}_{\epsilon_0 \chi^{(1)}} \hat{E}_j e^{i\omega t} + c.c. \quad (2.120)$$

and the polarization is proportional to the electric field, which is in agreement with the traditional result presented in section 2.4.2. From (2.37), it follows that

$$\chi_{ij}^{(1)} = \frac{N}{\epsilon_0 \hbar} \left( \frac{\langle j \rangle_{01} \langle i \rangle_{10}}{\tilde{\omega}_{10}^* - \omega} + \frac{\langle i \rangle_{01} \langle j \rangle_{10}}{\tilde{\omega}_{10} + \omega} \right) \quad (2.121)$$

and for a many-level system,

$$\chi_{ij}^{(1)} = \frac{N}{\epsilon_0 \hbar} \sum_j \left( \frac{\langle j \rangle_{01} \langle i \rangle_{10}}{\tilde{\omega}_{10}^* - \omega} + \frac{\langle i \rangle_{01} \langle j \rangle_{10}}{\tilde{\omega}_{10} + \omega} \right). \quad (2.122)$$

The system behaves as a forced oscillator, that is driven by the applied frequency  $\omega$ , rather than its natural frequency. The forced oscillations create temporary, virtual energy states in the medium, which supports short-lived transitions that would be otherwise forbidden. This is illustrated in figure 2.11. If the complex nature of the natural frequency is ignored, the denominators in the susceptibility term is simply the separation between the real energy transition  $\hbar\omega_{01}$  and the virtual energy levels  $\hbar\omega$ . Resonance effects are observed in the linear susceptibility when the energy of the photons in the wave approach the transition energy of the system.

## 2.5.4 Higher-Order Processes

The take-home message from the previous section is the use of virtual energy levels in a medium perturbed by an electromagnetic wave. The wave alters the properties of the medium, effectively transforming it into a new medium. Photons can be absorbed into intermediate energy levels corresponding to the driving energy of the perturbation wave, which would be forbidden in the unperturbed case. The virtual states originate from the

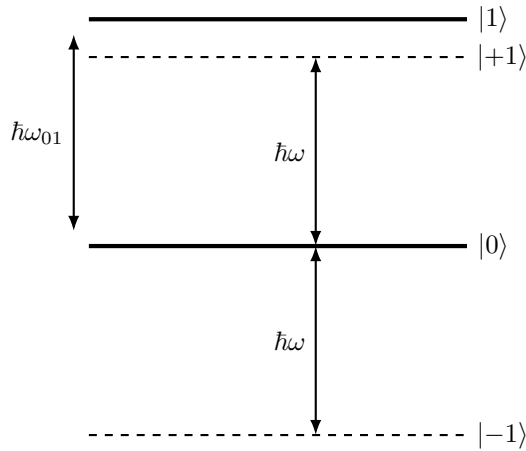


**Figure 2.11:** Two level system with virtual states created by the forced oscillations of the electromagnetic wave.

electron response, and are therefore instantaneous [18]. They are not eigenstates, and cannot be occupied once the perturbation is removed. If enough photons participate in the process, virtual energy levels can further be created at  $\pm 2\hbar\omega$ ,  $\pm 3\hbar\omega$  and so on. Photons can therefore combine in a multitude of ways, and new photons can be emitted from the virtual states to give rise to effects such as second-harmonic generation, sum and difference-frequency generation, third-harmonic generation, etc. Since the number of photons in an electromagnetic wave is related to the amplitude, the quantum mechanical model conforms well with the classical notion that these are nonlinear effects.

In the previous section, the perturbation was done to first order. The obtained results can be used to extend the perturbation to second and third order, and with additional energy levels. Analogous to (2.117),  $a_2^{(1)}$  for an additional energy level  $|2\rangle$  is given by

$$a_2^{(1)} = \frac{1}{2\hbar} \sum_j \langle j \rangle_{20} \left( \frac{\hat{E}_j e^{i\omega t}}{\omega_{20} + \omega} + \frac{\hat{E}_j^* e^{-i\omega t}}{\omega_{20} - \omega} \right) \quad (2.123)$$

since the energy levels are functionally equivalent. The second-order perturbation is given by

$$\frac{\partial a_1^{(2)}}{\partial t} + i\omega_{10} a_1^{(2)} = -\frac{i}{\hbar} V_{12} a_2^{(1)}. \quad (2.124)$$

The corresponding second-order polarization contains a large number of terms, corresponding to different transition sequences, which in turn correspond to different nonlinear effects. The resulting equations are therefore often subdivided based on the effect of interest. The result for e.g. second-harmonic generation for a three-level system is

$$\begin{aligned}
 \hat{P}_i^{2\omega} = \frac{N}{2\hbar^2} \sum_{jk} & \left( \frac{\langle j \rangle_{01} \langle k \rangle_{12} \langle i \rangle_{20}}{(\omega_{10} - \omega)(\omega_{20} - 2\omega)} + \frac{\langle j \rangle_{02} \langle k \rangle_{21} \langle i \rangle_{10}}{(\omega_{20} - \omega)(\omega_{10} - 2\omega)} \right. \\
 & + \frac{\langle k \rangle_{01} \langle i \rangle_{12} \langle j \rangle_{20}}{(\omega_{10} - \omega)(\omega_{20} + \omega)} + \frac{\langle k \rangle_{02} \langle i \rangle_{21} \langle j \rangle_{10}}{(\omega_{20} - \omega)(\omega_{10} + \omega)} \\
 & \left. + \frac{\langle i \rangle_{01} \langle j \rangle_{12} \langle k \rangle_{20}}{(\omega_{10} + 2\omega)(\omega_{20} + \omega)} + \frac{\langle i \rangle_{02} \langle j \rangle_{21} \langle k \rangle_{10}}{(\omega_{20} + 2\omega)(\omega_{10} + \omega)} \right) \hat{E}_j^\omega \hat{E}_k^\omega
 \end{aligned} \tag{2.125}$$

where dampening has been neglected in the denominators.

The transitions corresponding to term 1, 3 and 5 in (2.125) are illustrated in figure 2.12, namely the sequence  $0 \Rightarrow 1 \Rightarrow 2 \Rightarrow 0$ . This is indicated by the black arrows on the left-hand side of the diagram. The gray arrows indicate the virtual energy transitions and the solid double-sided arrows indicate the energy separation between the real and virtual sequence. Each virtual sequence has two associated energy separations, whose product appear in the denominators of (2.125) and therefore indicate the strength of the given term. It should be noted that, in the quantum mechanical framework, the issue of centrosymmetry as a necessity for second-order processes is reflected in the dipole matrix. States have definite parity in a medium with inversion symmetry, and there is thus no way of choosing a sequence of transitions to close the loop. It follows that the triple-products of the dipole matrix elements in (2.125) are zero.

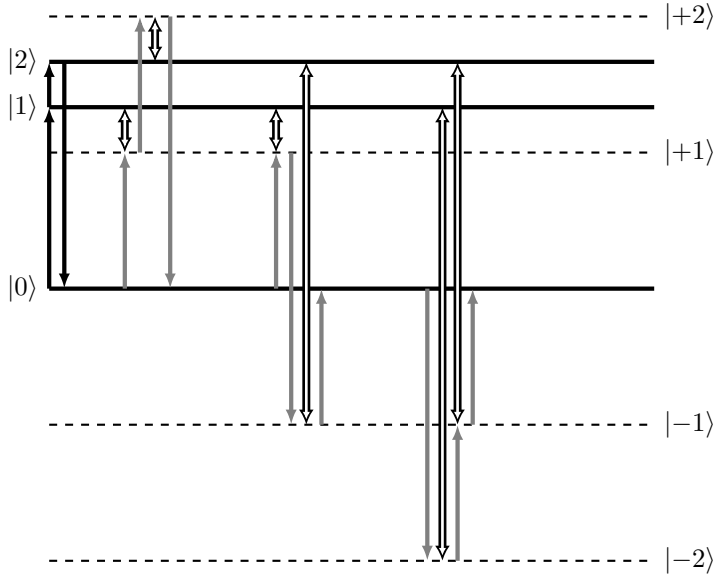


**Figure 2.12:** Possible transitions of second-harmonic generation in a three-level system. The black arrows show the real level sequence, the gray arrows show possible virtual sequences and the solid double-sided arrows show the separation energy between the real and virtual levels.

Third-order interactions are similarly described by extending the perturbation theory to third-order. The mathematics for third-order interactions is much more complicated due to the many terms, and is therefore not examined in detail. The corresponding energy diagram for the intensity-dependent refractive index (IDRI) is presented in figure 2.13.

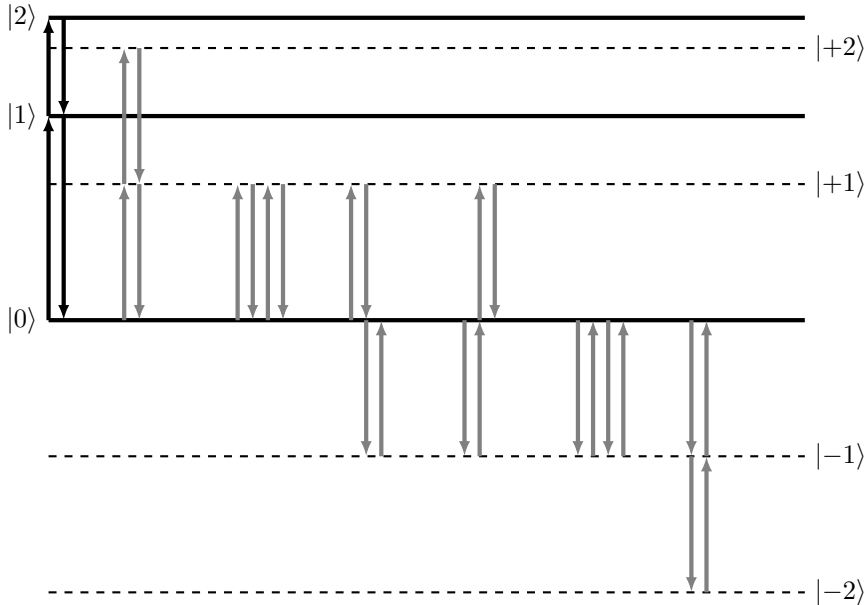


**Figure 2.13:** Transition sequences for IDRI.

As the figure illustrates, IDRI (and OKE) is the result of the mixing of four photons at the same frequency. This reconciles the quantum description with the classical equations presented in section 2.4.6. It also highlights the necessity to include all involved frequencies in the argument for the third-order susceptibility.

## 2.5.5 The Stimulated Raman Effect

It was shown in the previous sections that virtual energy levels enable energy transitions from the instantaneous electronic response. Two photons may be absorbed indirectly (as opposed to a direct, linear absorption) through a virtual energy level and emitted at a different frequency such that the difference frequency lies close to a material resonance. This process is known as a Raman resonance, and leaves the system in an excited state.

Raman resonance involves two waves at different frequencies. Following the conventional terminology of early experiments on spontaneous Raman scattering in the 1920s, the high frequency component is termed the laser wave  $\omega_L$  (or sometimes the pump wave), and the low frequency the Stokes wave  $\omega_S$  ( $\omega_L > \omega_S$ ). When IDRI and OKE was explained in section 2.4.6, it was assumed that  $\chi^{(3)}$  was real, and in this case, the theory applies directly. However, when  $\chi^{(3)}$  is taken to be complex, i.e.  $\chi^{(3)} = \chi' + i\chi''$ , the intensity of the Stokes wave is found to grow or decay according to



$$\frac{\partial I_S}{\partial z} = g_S I_S \quad (2.126)$$

where  $g_S \propto \chi''_R$  is the Stokes gain coefficient and the subscript  $R$  indicates Raman scattering. Growth or decay of the Stokes wave is determined by the sign of  $\chi''_R$ .

Stokes gain is maximized when the difference frequency of the laser and Stokes waves matches a material resonance, i.e.  $\omega_L - \omega_S = \Omega$ , as shown in figure 2.14. Here, the interaction is shown to be on resonance with a molecular vibrational state. The resonance could also originate in rotational or electronic energy levels.

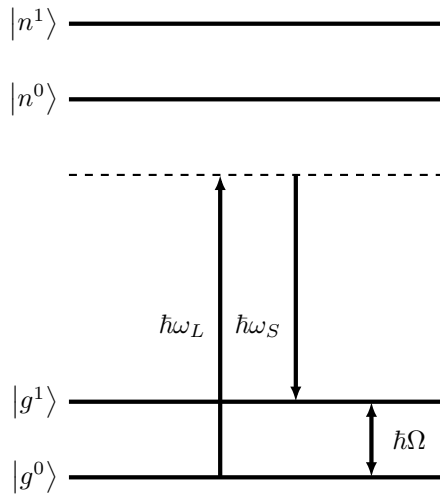


**Figure 2.14:** Simple Raman resonance model for system with two nuclear vibrational levels ( $g^0$  and  $g^1$ ) and two electronic levels ( $n^0$  and  $n^1$ ).

Clearly, absorption of a laser photon and emission of a Stokes photon implies loss of energy, since there is one-to-one correspondence in the photon exchange, but not in the frequency. The energy is lost to the medium in the form of an excitation, and a population of molecules remain in this state for a certain lifetime. The energy may be lost in the form of spontaneous emission, in which a photon at the Raman frequency  $\Omega$  is emitted. Other possibilities exist where emission is stimulated by other photons. Some possible scenarios are shown in figure 2.15. Stimulated Raman gain (SRG) is observed when the Stokes wave is absorbed and a photon at the laser frequency is emitted, as illustrated in 2.15 (b) [18]. Negative virtual levels (not shown) can similarly give rise to stimulated Raman loss (SRL). Figure 2.15 (c) illustrates the first anti-Stokes scattering, and is often referred to as coherent anti-Stokes Raman scattering (CARS). In this scenario, a photon at the laser frequency is absorbed from an excited state, and a photon at the anti-Stokes frequency is emitted. A third example is shown in figure 2.15 (d), in which the gain in the Stokes wave causes the material to be pumped at the Stokes frequency and a second Stokes wave is created. This can cascade into several further down-shifted frequencies.

The nonlinear polarization arising at the Stokes frequency can be calculated from

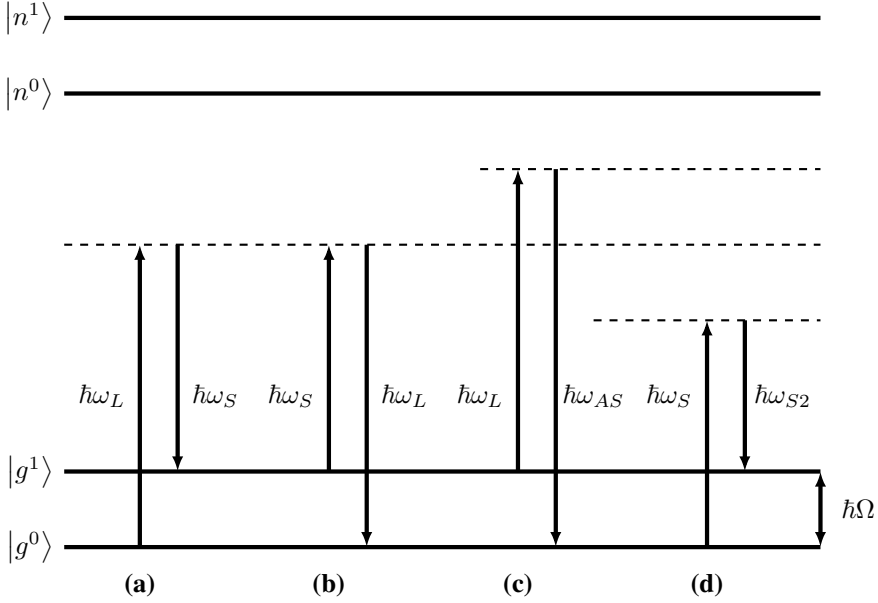


**Figure 2.15:** (a) First Stokes scattering (b) Stimulated Raman gain (c) Anti-Stokes scattering (d) Second Stokes scattering.

(2.110), using third-order permutations of the density matrix. The result is provided by Bloembergen [19]<sup>3</sup>

$$\langle P^{NL}(\omega_S) \rangle = \langle P^{NL}(-\omega_S) \rangle^* = NTr(\hat{\mu}^* \rho^{*(3)}(-\omega_S)) \quad (2.127)$$

which is found to be

$$\langle P^{NL}(\omega_S) \rangle = \chi_S(\omega_S; \omega_L, -\omega_L, \omega_S) |E_L|^2 E_S \quad (2.128)$$

where  $\chi_S$  is the Stokes-susceptibility, given by

$$\chi_S = -\frac{Ne^4 \hbar^{-3} \eta^2}{\omega_L - \omega_S - \omega_{g'g^0} - i\gamma_{g'g^0}} \times \left| \frac{\mu_{ng}\mu_{gn}}{\omega_L - \omega_{n^0g^0}} - \frac{\mu_{ng}\mu_{gn}}{\omega_L - \omega_{n'g^0}} - \frac{\mu_{ng}\mu_{gn}}{\omega_S + \omega_{n^0g^0}} + \frac{\mu_{ng}\mu_{gn}}{\omega_S + \omega_{n'g^0}} \right|^2 \quad (2.129)$$

and  $\eta$  is related to the interaction Hamiltonian by  $\eta(-\mu_{ng})E_S = \hat{H}_{n'g^0}^{(\omega_S)} = -\hat{H}_{n^0g'}^{(\omega_S)}$ . Resonance occurs from the denominator as the difference frequency between the laser and Stokes wave approach the transition energy  $\hbar\omega_{g'g^0}$ . At exactly resonance,  $\omega_L - \omega_S - \omega_{g'g^0} = 0$  and the susceptibility is purely imaginary and limited only by the damping

<sup>3</sup>The notation has been altered to, as best as possible, match that of New [6].

term  $\gamma_{g'g^0}$ . The real part of third-order susceptibility can be divided into a constant, non-resonant background  $\chi'_{NR}$  and the real-part of the Stokes susceptibility  $\chi'_S$ , which is resonant around  $\Omega$ . The imaginary part is similarly expressed by the imaginary part of the Stokes susceptibility  $\chi''_S$ , with zero background off-resonance in agreement with previous discussion on IDRI/OKE. The real and imaginary parts satisfy the same criteria for the Kramers-Kronig relation as the linear susceptibility.

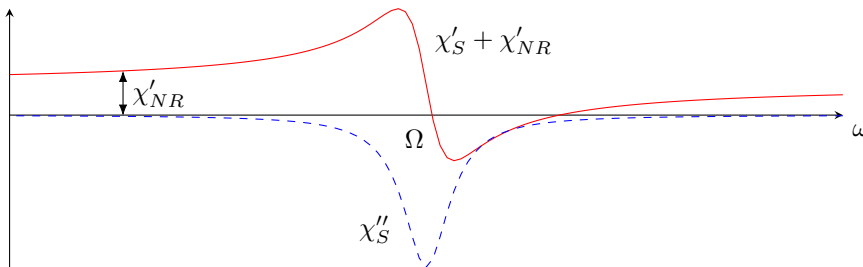


**Figure 2.16:** Dispersion relation for the third-order susceptibility. The solid curve shows the real part, and the dashed curve shows the imaginary part. Off-resonance, the susceptibility is dominated by a constant background susceptibility, originating from the instantaneous electronic response. The graph is intended to reflect the results presented by [19].

## 2.6 Magnetism in Materials

### 2.6.1 Introduction

The remainder of this chapter is devoted to magnetism and magneto-optics. Before proceeding to magneto-optics, it is appropriate to introduce the different types of magnetism that is found in different materials. Ferromagnetism is of particular interest, and is discussed in section 2.6.3. The theory in this section is primarily taken from [20].

Macroscopic magnetization in materials originates from the magnetic moment of individual electrons. There are two sources that give rise to the magnetic moment. One is the orbital motion around the nucleus in the atom, which can be considered a tiny, closed loop of current. The other is the moment arising from the electron spin around its own axis, which can be directed up or down.

The net magnetic moment of an atom is the total contribution from orbital motion and spin. Electron pairs of opposing direction (such as spin up and spin down) cancel each other out, creating net zero magnetic moment. In an atom with all shells or subshells filled, such as in the inert gases, the magnetization is completely canceled. Permanent magnetization is therefore not possible in such materials. The connection to the electron orbitals makes macroscopic magnetization a highly material-specific property. Materials can be classified based on their magnetic properties: the three main classes of magnetism are diamagnetism, paramagnetism and ferromagnetism. Antiferromagnetism and ferrimagnetism are additional subclasses of ferromagnetism.

## 2.6.2 Types of Magnetism

Materials of different classes of magnetization respond very differently to an externally applied magnetic field. The response is characterized by the magnetization  $M$ , which is related to the magnetic field by

$$M = \chi_m H \quad (2.130)$$

where  $\chi_m$  is the magnetic susceptibility which is dimensionless. The magnetic susceptibility is related to the material permeability  $\mu$ , the free-space permeability  $\mu_0$  and the relative permeability  $\mu_r$  by

$$\chi_m = \frac{\mu}{\mu_0} - 1 \equiv \mu_r - 1. \quad (2.131)$$

The relative permeability may be greater or lesser than unity, and the magnetic susceptibility can therefore be negative.

Diamagnetism and paramagnetism are the weakest forms of magnetism, and are characterized respectively by a negative and positive magnetic susceptibility that is close to unity. They possess no spontaneous magnetization, and the flux density inside the materials in the absence of an external magnetic field is close to that of vacuum. Diamagnetic and paramagnetic materials are therefore often referred to as non-magnetic materials.

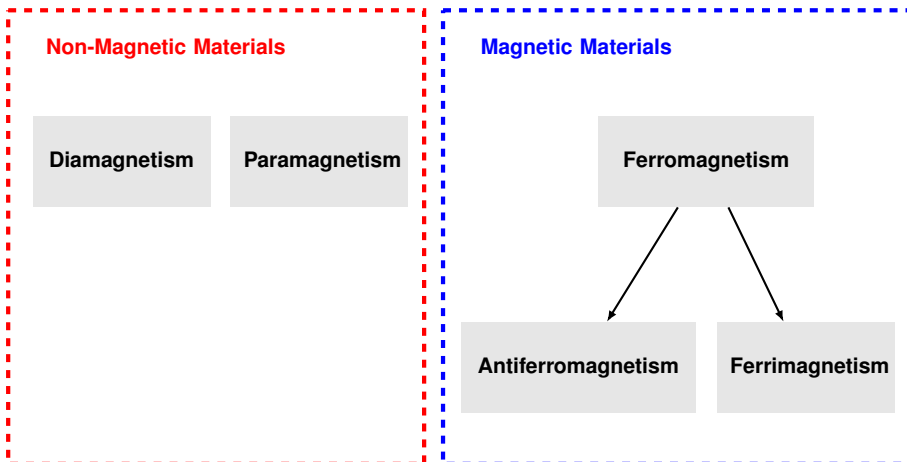


**Figure 2.17:** Classification of magnetic materials.

When diamagnetic materials are exposed to an external magnetic field, the orbital motion of the electrons change slightly. This causes a magnetization to be induced in the opposite direction of the applied field, which corresponds to a negative magnetic susceptibility. The effect is very weak, and typical orders of magnitude for  $\chi_m$  is  $-10^{-5}$ . When subjected to a strong enough field, diamagnetic materials will tend to move against regions of weaker magnetization, and are hence repelled by magnets.

Paramagnetic materials have permanent dipole moments due to incomplete cancellation of spin and/or orbital moments. They are randomly oriented, and therefore possess

no net macroscopic magnetization. The dipoles are however free to rotate, and may align themselves with an external field. This gives rise to a magnetization aligned with the external field, but since there is no interaction between adjacent dipoles, the induced magnetization is weak. For paramagnetic materials,  $\chi_m$  is positive, and typically in the range  $10^{-2}$  to  $10^{-5}$ .

Ferromagnetic materials are classified by a permanent magnetic moment in the absence of an externally applied magnetic field (i.e. spontaneous magnetization). Only a handful of elements possess ferromagnetic properties, including iron, cobalt, nickel and some rare earth metals. The magnetic susceptibility can be as high as  $10^6$ , and the magnetic flux density inside the material is therefore dominated by the magnetization field ( $M \gg H$ ). Ferromagnetism originates in atomic magnetic moments due to uncancelled electron spins. Coupling exists between neighboring atoms, which causes the magnetization to be retained after an external field is removed. The magnetization therefore depends on the history of the applied field, and ferromagnetic materials hence possess hysteresis properties. The coupling can exist over relatively large volumes, and a region with uniform magnetization is called a domain. Hysteresis and domains are explained in further detail in the next section.

Lastly are the classes of antiferromagnetism and ferrimagnetism. Like ferromagnetic materials, magnetic coupling exist between neighboring atoms. The coupling in antiferromagnets cause neighboring spins to align in antiparallel. The material as a whole therefore sees a cancellation of spin and experiences no magnetic moment. Antiferromagnets are often used in combination with ferromagnets in thinfilms, to create devices with specialized magnetic properties. Coupling between ferromagnetic and antiferromagnetic layers can create a preferred direction of magnetization, which gives rise to an offset in the hysteresis, known as exchange bias [21]. Ferrimagnetism is characterized by both parallel and antiparallel coupling, however unlike antiferromagnets, spontaneous magnetization exists due to incomplete cancellation of spins.

### 2.6.3 Domains and Hysteresis

The characteristic magnetic behavior of a ferromagnet is only observed below the Curie temperature  $T_c$ , in which the material consists of small regions of mutual alignment of the magnetization. These small volumes are called domains, and individual domains are in a local saturation of the magnetization. Adjacent domains are separated by domain walls, in which the magnetization rotates from one direction to another. The macroscopic magnetization field is the vector sum of all domain contributions.

When a specimen is initially unmagnetized, the spontaneous magnetization is zero. As the external magnetic field strength is increased from zero, the  $M - B$  relationship is linear and given by the initial permeability  $\mu_i$ , which is a material property. After a certain field strength is reached, the linearity is broken, and the permeability becomes a nonlinear function of  $B$ . Domains that are favorably oriented, that is, partially or fully aligned with the applied field, begins to grow at the expense of less favorable domains. These domains grow in volume by absorbing neighboring domains, and the magnetization increases sharply for small variations in the magnetic field. Eventually, the specimen consists of only a single, large domain, nearly aligned with the field, and the magnetization starts to tail off. Further increase of the field achieves saturation by means of rotation,

and when the magnetization is perfectly aligned with the field, no further increase in the magnetization can be achieved.

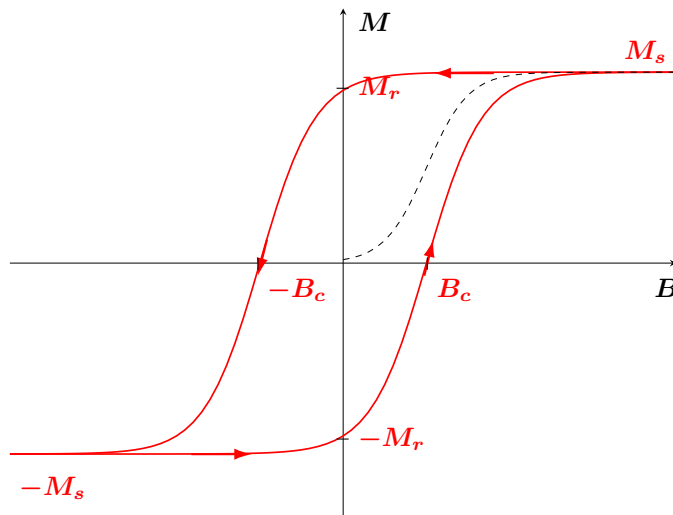


**Figure 2.18:** Hysteresis curve (thick line) with initial magnetization from unmagnetized state (dashed line). Coercivity, saturation magnetization and remanence field are marked in the figure. The arrows indicate the direction of the magnetic cycle.

After initial magnetization, a ferromagnetic specimen can not return directly to the unmagnetized state. Instead, the magnetic response is characterized by a hysteresis behavior. The hysteresis may be described in terms of *coercivity*, *saturation magnetization*, *remanence field* and *exchange bias*:

- **Coercivity/Coercive field ( $B_c$ )** - The field strength required to reduce the magnetization to zero in the direction opposite to the previous magnetization. The coercive field corresponds to half the width of the hysteresis curve around zero magnetization.
- **Saturation magnetization ( $M_s$ )** - The magnetization in the saturation region.
- **Remanence field ( $M_r$ )** - The magnetization retained by the material after the external field is removed. This originates in the resistance to change in domain walls, and causes the magnetization to lag behind the applied field. The remanence field typically lies close to the saturation magnetization, particularly for hard magnetic materials (as opposed to soft), which are characterized by a large hysteresis area.
- **Exchange bias ( $B_e$ )** - The offset in the hysteresis. This is caused by magnetic pinning from an antiferromagnetic layer, and is not normally observed in single-layered ferromagnets.

Figure 2.18 shows a typical hysteresis curve, with the characteristic fields marked in. The arrows indicate the direction of the magnetic cycle, where the field is increased in one

direction until saturation is reached, and then reversed until saturation is reached in the opposite direction. Since the magnetization field depends on the history of the applied magnetic field, the hysteresis may take on different shapes based on the driving field.

## 2.7 Magneto-Optics

### 2.7.1 Introduction

Magneto-optics (MO) encompasses a group of phenomena associated with the alteration of light as it reflects from, or transmits through a medium, due to the magnetic state of the medium. MO effects are weak in nature, and undetectable in most materials. The MO response is greatly enhanced by the high magnetic ordering of ferromagnetic materials, and they are indeed the main subject of most MO studies. The first of the effects to be observed, and perhaps the most well known, is the Faraday effect, discovered in 1845 by Michael Faraday. Light transmitted through a medium parallel to the direction of magnetization experiences a nonreciprocal rotation of the polarization state. This has many practical applications today, typically as Faraday rotators, Faraday mirrors or optical circulators in optical fibers [11]. Magnetic fields exist as one of the few things to locally break the time-reversal symmetry found throughout most other physical systems. In other words, the presence of the magnetic field causes the system to behave differently if the direction of time were to be reversed. Magneto-optical systems therefore violate the principle of reciprocity.

Magneto-optical effects are characterized by complex off-diagonal tensor elements in the complex linear susceptibility tensor. The MO effect is equivalently reflected in the complex dielectric tensor  $\epsilon$  or in the complex conductivity tensor  $\sigma$  [8]. The dielectric tensor is more commonly used in the literature. For a magnetized medium with arbitrary direction of magnetization, the dielectric tensor takes on the form (see appendix C)

$$\epsilon = \begin{bmatrix} \epsilon_{xx} & \epsilon_{xy} & -\epsilon_{xz} \\ -\epsilon_{xy} & \epsilon_{xx} & \epsilon_{yz} \\ \epsilon_{xz} & -\epsilon_{yz} & \epsilon_{xx} \end{bmatrix} \quad (2.132)$$

which satisfies the Onsager symmetry identity

$$\epsilon_{ij}(\mathbf{M}) = \epsilon_{ji}(-\mathbf{M}). \quad (2.133)$$

### 2.7.2 The Magneto-Optical Kerr Effect

When linearly polarized light is reflected on a plane interface between an ambient and magnetic medium, the polarization state changes. This is known as the magneto-optical Kerr effect (MOKE). Rotation and ellipticity is attributed respectively to the real and imaginary part of the complex refractive index of the magnetic medium. The diagonal terms in the dielectric tensor are nonmagnetic, and remain unchanged by a reversal of the magnetic field. The off-diagonal elements contain the contribution from the magnetization of the medium, and can be probed under certain experimental geometries to directly measure the magnetization of the medium.

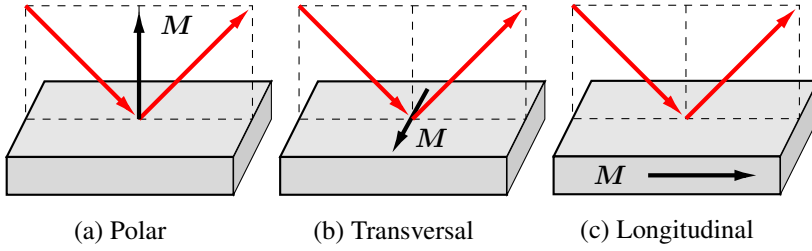


**Figure 2.19:** Experimental MOKE geometries. The dashed line indicates the plane of incidence, the red arrows show the incident and reflected light, and the black arrow shows the direction of magnetization. The magnetic field is (a) perpendicular to the interface plane (b) parallel to the interface and normal to the plane of incidence (c) parallel to both the surface and the plane of incidence [22]

MOKE can be divided into three "pure" MOKE geometries, or MOKE states, corresponding to different configurations of the interacting fields: polar MOKE (P-MOKE), transversal MOKE (T-MOKE) and longitudinal MOKE (L-MOKE). The direction of the magnetization is respectively perpendicular to the interface, parallel to the interface and normal to the plane of incidence and parallel to both the surface and the plane of incidence [22]. This is illustrated in figure 2.19. In each of the three configurations, four of the six off-diagonal tensor elements in (2.132) vanish, and the effects of each state can be probed in isolation. P-MOKE is the effect with the strongest MO response, however this requires a polar field to be sustained within the medium. The geometric structure of magnetic thinfilms is in disfavor of polar fields, because they contribute a large fringe field. Fringe fields are associated with a higher energy cost, because the electrons in the medium must oppose a large external force pointing in the opposite direction of their collective spins. For this reason, L-MOKE is a more suitable tool for characterization, and is the focus of the remaining sections. It will also be assumed that the magnetic medium under study is optically and magnetically isotropic, unless otherwise stated.

### 2.7.3 Optical Rotation and Ellipticity of Circularly Polarized Waves

The physical origin of the MO effects can be attributed to the difference in refractive index experienced by electromagnetic waves traveling in the left and right-hand direction (in accordance with the right-hand rule). A linearly polarized wave can always be decomposed into a superposition of two circularly polarized waves [5]. A wave polarized along the  $y$ -direction can be expressed as

$$\mathbf{E} = E_+ \hat{\sigma}_+ + E_- \hat{\sigma}_- \quad (2.134)$$

where

$$\hat{\sigma}_\pm = \frac{\hat{y} \pm i\hat{x}}{\sqrt{2}}. \quad (2.135)$$

The real part of the complex refractive index corresponds to the amount of reduction in phase velocity in relation to a wave propagating in free-space, and is referred to as the



refractive index. The imaginary part of the complex refractive index corresponds to the degree of absorption, and is referred to as the extinction coefficient

$$N = n + ik. \quad (2.136)$$

In a magnetic medium, right and left-hand polarized waves see a different refractive index, and consequently travel with a different phase velocities and experience a different degree of absorption [23].

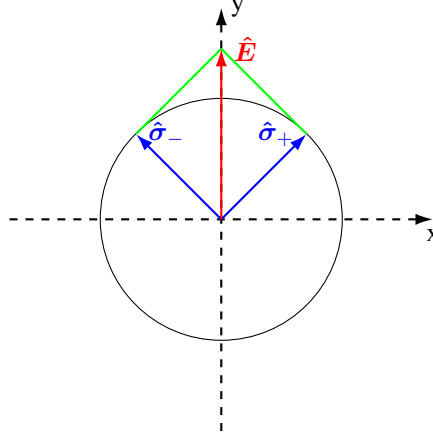


**Figure 2.20:** Linearly polarized wave, polarized along the y-axis, decomposed into a left and right-hand circularly polarized wave.

We first consider the case where the complex refractive index is purely real, i.e.  $N = n$ . The waves  $\hat{\sigma}_+$  and  $\hat{\sigma}_-$  travel with different phase velocities in the magnetic medium, but experience no attenuation. A phase shift is induced between the two waves, and the direction of polarization is rotated. There is however no ellipticity induced in the wave, since both waves have equal magnitude. This is referred to as optical rotation, and is a magneto-optic effect.

The x- and y-components of  $\hat{\sigma}_+$  and  $\hat{\sigma}_-$  can be expressed as

$$E_x^- = A \cos(kz - \omega t) \quad (2.137)$$

$$E_y^- = -A \sin(kz - \omega t) \quad (2.138)$$

and

$$E_x^+ = A \cos(kz - \omega t) \quad (2.139)$$

$$E_y^+ = A \sin(kz - \omega t). \quad (2.140)$$

We denote the refractive index of the right- and left-hand circular waves as  $n^+$  and  $n^-$  respectively. The x- and y-components can then be rewritten as

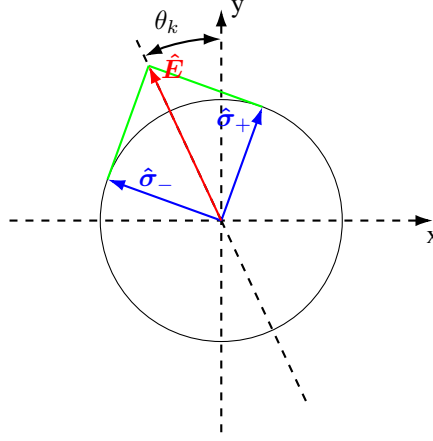


**Figure 2.21:** Illustration of optical rotation. In a magnetic medium with purely real complex refractive index  $N$ ,  $\hat{\sigma}_+$  and  $\hat{\sigma}_-$  travel with different phase velocities and are shifted in phase. The linear polarization state rotates by an angle  $\theta_k$  without becoming elliptical.

$$E_x^- = A \cos \left[ \frac{\omega}{c_0} (n^- z - c_0 t) \right] \quad (2.141)$$

$$E_y^- = -A \sin \left[ \frac{\omega}{c_0} (n^- z - c_0 t) \right] \quad (2.142)$$

and

$$E_x^+ = A \cos \left[ \frac{\omega}{c_0} (n^+ z - c_0 t) \right] \quad (2.143)$$

$$E_y^+ = A \sin \left[ \frac{\omega}{c_0} (n^+ z - c_0 t) \right]. \quad (2.144)$$

By defining  $\bar{n} = \frac{n^+ + n^-}{2}$  and applying trigonometric identities for the sum and difference of sines and cosines, it can be shown that the sum of each component is

$$E_x = E_x^+ + E_x^- = 2A \cos \left[ \frac{\omega}{c_0} (nz - c_0 t) \right] \cos \left[ \frac{\omega}{2c_0} (n^+ - n^-) z \right] \quad (2.145)$$

$$E_y = E_y^+ + E_y^- = 2A \cos \left[ \frac{\omega}{c_0} (nz - c_0 t) \right] \sin \left[ \frac{\omega}{2c_0} (n^+ - n^-) z \right]. \quad (2.146)$$

The angle of rotation is termed the Kerr angle  $\theta_k$ , and is given by

$$\tan \theta_k = \frac{E_x}{E_y} = \frac{2A \cos \left[ \frac{\omega}{c_0} (nz - c_0 t) \right] \cos \left[ \frac{\omega}{2c_0} (n^+ - n^-) z \right]}{2A \cos \left[ \frac{\omega}{c_0} (nz - c_0 t) \right] \sin \left[ \frac{\omega}{2c_0} (n^+ - n^-) z \right]} \quad (2.147)$$

$$= \tan \left[ \frac{\omega}{2c_0} (n^+ - n^-) z \right] \quad (2.148)$$

from which it follows that

$$\theta_k = \frac{\omega}{2c_0} (n^+ - n^-) z. \quad (2.149)$$

The angle of rotation (in radians) is directly proportional to the interaction length and the separation in refractive index between the right- and left-hand circularly polarized waves.

Next, we consider the effect of attenuation on the circularly polarized waves. The complex refractive index is now assumed to contain polarization-dependent attenuation, but not phase velocity. Since both waves complete a full rotation in the same amount of time, the axis of oscillation does not change. However, since one of the waves is attenuated more than the other, the amplitude difference causes the field to follow an ellipse instead of a straight line. If one of the two waves were completely attenuated, the polarization would become purely circular. When only some attenuation is observed, the linear polarization broadens to an ellipse along the original axis of oscillation. This is illustrated in figure 2.22.

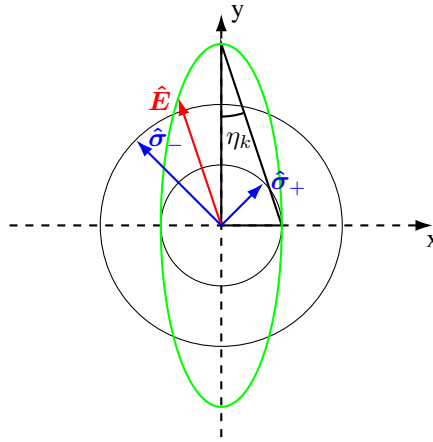


**Figure 2.22:** Ellipticity from polarization-dependent attenuation of circular waves. The green curve shows the trace of the electric field as an ellipse. The ellipticity is defined by the angle  $\eta_k$ .

The ellipticity is qualitatively described by the angle  $\eta_k$ , which is given by

$$\tan \eta_k = \frac{|\hat{\sigma}_+| - |\hat{\sigma}_-|}{|\hat{\sigma}_+| + |\hat{\sigma}_-|}. \quad (2.150)$$

For small angles, this can be written as

$$\eta_k = \frac{\sqrt{I_+} - \sqrt{I_-}}{\sqrt{I_+} + \sqrt{I_-}} \quad (2.151)$$

where  $I_{\pm}$  is the intensity the waves. Empirically, the absorbance is related to the intensity by Beer's law

$$I = I_0 e^{-A \ln 10}. \quad (2.152)$$

Inserting this expression into (2.151) yields

$$\eta_k = \frac{\exp\left(-\frac{A^+}{2} \ln 10\right) - \exp\left(-\frac{A^-}{2} \ln 10\right) \sqrt{I_0}}{\exp\left(-\frac{A^+}{2} \ln 10\right) + \exp\left(-\frac{A^-}{2} \ln 10\right) \sqrt{I_0}} \quad (2.153)$$

$$= \frac{\exp\left(-\frac{A^- - A^+}{2} \ln 10\right) - 1}{\exp\left(-\frac{A^- - A^+}{2} \ln 10\right) + 1} \quad (2.154)$$

and by expanding the exponentials into Taylor series, the expression is simplified to

$$\theta = (A^- - A^+) \frac{\ln 10}{4}. \quad (2.155)$$

This result shows that the ellipticity is proportional to the separation between absorbance in right and left-hand circular waves.

In a medium where both the refractive index and extinction coefficient differs for right- and left-hand circular waves, the polarization changes both through rotation and ellipticity. The result is an elliptical polarization with the majority axis rotated. This appears similar to how linear polarization behaves after interacting with an anisotropic medium, but differs in origin; in a nonmagnetic anisotropic medium, both rotation and ellipticity originate in the directional dependence of the phase velocity, but in a magnetic medium, it is related both to the phase velocity and attenuation.

#### 2.7.4 The Complex Voigt Vector

In order to quantitatively describe the magnetization, both the Kerr rotation and ellipticity must be taken into account. This can be represented by the complex Voigt vector, whose real part represents the Kerr rotation and imaginary part represents the Kerr ellipticity [14]

$$\tilde{\Theta}_k = \theta_k + i\eta_k. \quad (2.156)$$

It can be shown that, for both polar [14] and longitudinal [13] MOKE, the Voigt vector is proportional to the magnetization of the magnetic medium, i.e.

$$\tilde{\Theta}_k \propto M_i \quad (2.157)$$

**Table 2.5:** Linear (even) MO effects, classified by intensity/polarization analysis and reflection/transmission. Polarization sensitive effects include the Faraday effect, and polar and longitudinal MOKE. Intensity sensitive effects include magnetic circular dichroism (MCD) and transversal MOKE [24].

	Polarization analysis	Intensity
Transmission	Faraday	MCD
Reflection	P-MOKE L-MOKE	T-MOKE

where  $i = z, x$  for polar and longitudinal MOKE respectively. Transversal MOKE differs from the other two in that the polarization remains unaffected by the magnetization, and only the intensity changes. The MO effects that are linear in the magnetization are listed in table 2.5 [24]. The effects listed under *polarization analysis* are treated in terms of the Voigt vector.

### 2.7.5 Longitudinal MOKE

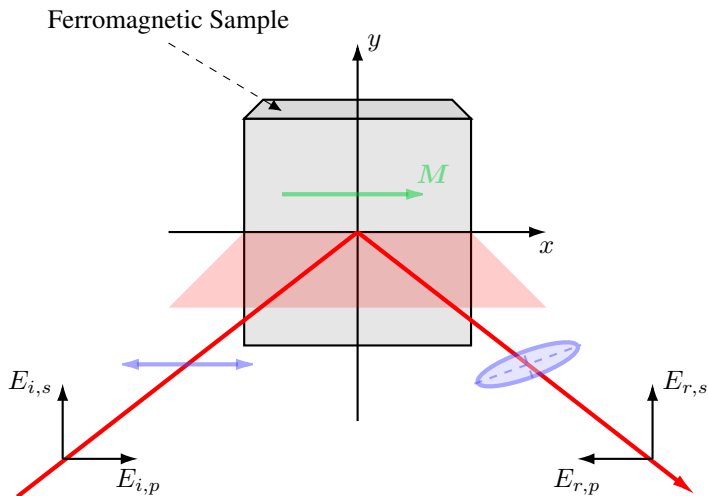


**Figure 2.23:** Longitudinal MOKE geometry. The plane of incidence is indicated by the red plane, and the polarization states are indicated by the blue shapes. The ferromagnetic sample is magnetized along the x-direction.

Consider the situation in figure 2.23 where light is incident on a ferromagnetic sample, polarized parallel to the plane of incidence (referred to as p-polarized light). The experimentally accessible quantities are related to the Fresnel coefficients, which give the ratio between p-polarized (parallel to the plane of incidence) and s-polarized (perpendicular to the plane of incidence) amplitudes for the incident and reflected light,  $r_{mn} = E_{r,m}/E_{i,n}$ .

The Fresnel coefficients are given by [13]

$$R = \begin{bmatrix} r_{ss} & r_{sp} \\ r_{ps} & r_{pp} \end{bmatrix} = \begin{bmatrix} r_s & \alpha m_x + \gamma m_z \\ -\alpha m_x + \gamma m_z & r_p + \beta m_y \end{bmatrix} \quad (2.158)$$

where  $\alpha$ ,  $\beta$  and  $\gamma$  are complex coefficients and  $m_x$ ,  $m_y$  and  $m_z$  are the normalized magnetization components. It is clear from the off-diagonal elements that a magnetization along x or y causes an intermixing between s- and p-polarized light. The derivation of (2.158) is based on the dielectric tensor being on the form

$$\epsilon = N^2 \begin{bmatrix} 1 & iQm_z & -iQm_y \\ -iQm_z & 1 & iQm_x \\ iQm_y & -iQm_x & 1 \end{bmatrix} \quad (2.159)$$

where  $N$  is the complex refractive index, and  $Q = Q_r + iQ_i$  is the complex magneto-optical coupling factor.  $Q$  is here assumed to be the same, irrespective of the direction of the field, i.e. *magneto-optical isotropy*. Generally, it is found that the contribution from polar MOKE is significantly larger than others.

When the magnetization is completely in the plane of the interface between the magnetic and ambient medium, i.e.  $m_z = 0$ , the complex Voigt vector can be expressed as

$$\tilde{\Theta}_k = \frac{r_{sp}}{r_p} = \tilde{\alpha} m_x \quad (2.160)$$

with

$$\tilde{\alpha} = \frac{-iNQ \cos \theta \tan \theta'}{(N \cos \theta - \cos \theta') (\cos \theta + N \cos \theta')} \quad (2.161)$$

where  $\theta$  and  $\theta'$  are the angles of incidence and refraction respectively. The complex coefficient  $\tilde{\alpha}$  depends both on the complex refractive index and MO coupling coefficient of the magnetic medium, and can be regarded as an experimental constant. It can be concluded that, as long as the magnetic medium is magneto-optically isotropic, both the Kerr angle and ellipticity are proportional to the x-component of the magnetization.

In cases of magneto-optical anisotropy, the situation is slightly more complicated. For a uniaxial crystal, the dielectric tensor along the symmetry-axis can be written as

$$\epsilon = N^2 \begin{bmatrix} 1 & iQ_{\perp} m_z & -iQ_{\perp} m_y \\ -iQ_{\perp} m_z & 1 & iQ_{\parallel} m_x \\ iQ_{\perp} m_y & -iQ_{\parallel} m_x & 1 \end{bmatrix} \quad (2.162)$$

where  $Q_{\perp}$  is the MO coupling factor perpendicular to the symmetry axis, and  $Q_{\parallel}$  is the parallel. By applying a coordinate transform about an angle  $\phi_0$  in reference to the symmetry axis, the resulting Voigt vector is

$$\tilde{\Theta}_k = \tilde{\alpha} [(1 + \tau \sin^2 \phi_0) m_x - \tau \cos \phi_0 \sin \phi_0 m_y] \quad (2.163)$$

where

$$\tau = \frac{Q_{\perp} - Q_{\parallel}}{Q_{\parallel}}. \quad (2.164)$$

The resulting Kerr angle and ellipticity thus have a contribution from the transverse direction of the magnetization.

### 2.7.6 Nonlinear Magneto Optics

Lastly, we make a brief mention of a fourth type of Kerr effect, known as nonlinear MOKE (NOLIMOKE). This is an effect similar to the second-harmonic generation effect described by nonlinear optics, but originates in both the magnetization and the optical field. Very generally, the dielectric tensor can be expressed as a Taylor series in the various fields [24]

$$\epsilon \approx \epsilon_0 + O(\mathbf{k}) + O(\mathbf{B}) + O(\mathbf{E}) + O(B_i E_j) + O(B_i B_j) + \dots \quad (2.165)$$

where  $\epsilon_0$  is the normal, linear permittivity,  $O(\mathbf{k})$  originates in natural optical activity,  $O(\mathbf{B})$  and  $O(B_i B_j)$  correspond to magneto-optic effects,  $O(\mathbf{E})$  to electro-optic effects and  $O(B_i E_j)$  to magneto-electric effects. The magneto-optical response is then manifested as a wavelength shift, and exists as one possible method of non-invasive probing of the magnetization.

# The OKEMOKE System

## 3.1 Overview

### 3.1.1 Introduction

In this masters project, an optical system has been constructed and tested in the Ultrafast Optics Laboratory at NTNU. The primary function of this laboratory is to characterize materials based on optical measurement techniques. Our system utilizes the optical Kerr effect (OKE) and the magneto-optical Kerr effect (MOKE) to measure dynamical processes of certain classes of materials at ultrafast timescales. The pump-probe spectroscopic technique is used to achieve time-resolved sampling of dynamic transients. The system is shown in figure 3.1.

The system was built as an expansion of a pre-existing setup that could perform OKE spectroscopy. A large portion of this thesis is devoted to the OKE system, because it is the foundation on which the MOKE system was built. The OKE system has also been used throughout the duration of the project to perform various measurements. Details on these measurements are found in chapter 4.

This chapter explains how the system works, and how it is operated. It is implied that all results presented throughout the thesis were obtained from measurements performed by the system.

### 3.1.2 Capabilities of the System

Our system can perform measurements on small material samples that can be brought to the laboratory for characterization. A variety of measurements can be made on the materials, based on the principles of OKE and MOKE.

OKE is utilized to measure the time-resolved impulse-response function of the third-order nonlinear susceptibility after broad-band pump excitation. The Raman spectrum of the material can be extracted from the recorded time-domain signal by a series of signal-processing steps. The Raman spectrum provides the frequencies (and thereby the energies)



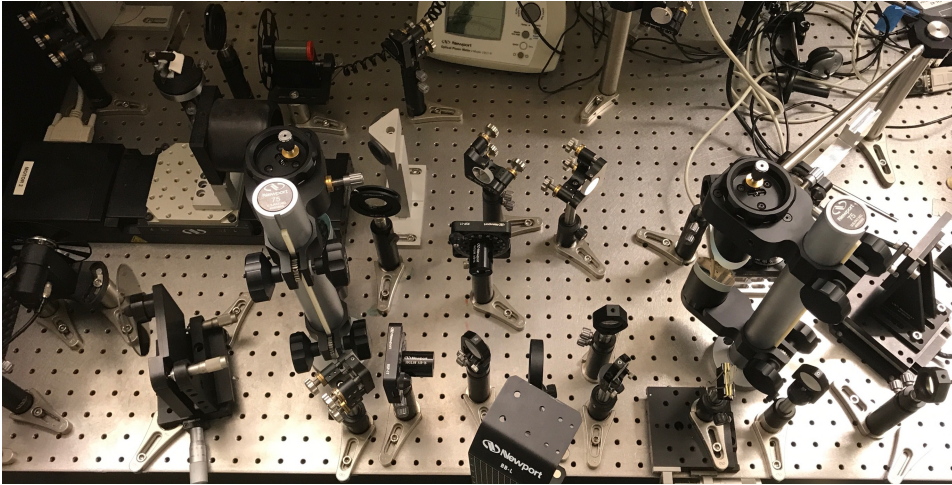


**Figure 3.1:** The optical measurement system. Optical and magneto-optical Kerr effect is utilized to perform characterization of materials.

of modes near the ground state, typically corresponding to low-level rotational or vibrational modes. These modes normally require THz radiation to be observed through linear absorption. The nonlinear measurement alleviates the need for these frequencies to be present in the laser, as long as the bandwidth<sup>1</sup> of the laser is larger than the frequency separation of the observed modes. More explicitly, so long as the difference frequency of the laser and Stokes wave falls within the bandwidth of the laser, Raman modes of the corresponding Stokes wave can be observed.

MOKE is used to measure the magnetization vector in a material. By varying an externally applied magnetic field, the magnetic hysteresis of the material is readily obtained. The time-resolved relaxation dynamics of the magnetization can be observed after pump-induced demagnetization to measure time constants of the demagnetization and the magnetization recovery transient.

MOKE measurements rely on a strong magneto-optical response, and can therefore only be performed on ferromagnetic materials. If the magnetization of the material is weak, antireflective (AR) coating can be applied to allow more light to interact with the medium. OKE measurements can in principle be done on all solids and liquids, but a useful analysis relies on other effects being absent. Since the measurement is done in transmission, the materials should be relatively transparent in wavelengths around the central wavelength of the laser (800 nm). Some degree of absorption is acceptable, but the measurement is rendered unreliable if the probe power is increased too close to the pump power.

---

<sup>1</sup>The term *bandwidth* is ambiguous in this context. Since the measurement relies on a third-order effect, the full-width at half maximum (FWHM) is not the best measure of the bandwidth. The measurement is limited to the frequency region of the laser strong enough to induce an appreciable number of virtual states, which attributes a signal significantly higher than the noise.

## 3.2 Pump-Probe Spectroscopy

### 3.2.1 Introduction

Pump-probe spectroscopy is a powerful tool for investigating dynamical material responses at ultrafast timescales. Two beams, termed the pump and the probe, interact with the medium. The pump is higher in optical intensity than the probe (typically by at least an order of magnitude), and is used to excite the material from thermal equilibrium. The probe beam interacts with the medium and conveys information about the excitation and relaxation dynamics, which can be extracted through detection of the probe. The transient behavior of the relaxation process, from the excitation to thermal equilibrium, accommodates interesting time-constants for the material. Spectral information can be retrieved by taking the Fourier transform of the time-resolved signal. The dualism of convolution and multiplication in the time and frequency domains enables retrieval of the frequency-dependent material coefficients. Furthermore, pump-probe measurements exist that uniquely define a chemical element or compound (such as the Raman spectrum), making it highly suitable for characterization.

The specific method of excitation and probing depends on the experimental design, and is discussed in detail in sections 3.3 and 3.4 for OKE and MOKE spectroscopy respectively. The probing mechanism of OKE and MOKE are fundamentally similar; both measure the degree of birefringence of the material, through the depolarization. The origin of the birefringence is however dissimilar. In OKE spectroscopy, birefringence is a direct consequence of the interaction between the nonlinear medium and the pump. However, in MOKE spectroscopy the magnetization field within the medium induces the birefringence, and can be tuned with an externally applied magnetic field. The pump interaction induces a change in the magnetization, which thereupon changes the birefringence. The domains of a ferromagnetic material (see section 2.6) ensures that the magnetization never completely vanishes, and birefringence is an intrinsic property of such materials. Measurements can therefore be made without a pump to obtain the hysteresis. An extra degree of freedom exists in the form of a magnetic field. Table 3.1 gives an overview of the roles of pump and probe (as well as the magnetic field in MOKE) for the different spectroscopic techniques.

**Table 3.1:** Overview of the pump and probe mechanisms for OKE and MOKE spectroscopy.

	Probe	Pump	Magnetic field
OKE	Optical-Kerr effect	Birefringence	-
MOKE	Magneto-optical Kerr effect	Demagnetization	Birefringence

### 3.2.2 Sampling with THz Resolution

High-resolution pump-probe spectroscopy is made possible by the advent of modern pulsed laser sources, which can generate pulses of extremely narrow temporal width: down to

femtosecond and even attosecond time-regimes. At such short timescales, the material can be considered "frozen in place" for the duration of interaction between the material and the pulse. The strong field of the pump serves to promote electrons from the ground state to higher energy states, where they will remain until they undergo spontaneous or stimulated emission, or thermalize back to equilibrium. This typically happens on the order of picoseconds (although many are faster), which makes femtosecond laser light short enough to resolve the process.

Recording of the relaxation is achieved by delaying the pump and probe pulses in relation to one another. This is achieved by a mechanical translation stage, with a set of mirrors oriented  $45^\circ$  to each other (called a retroreflector), as illustrated in figure 3.2 and depicted in figure 3.3. The speed of light in air is approximately  $3 \times 10^8$  m/s, which translates to a pump-probe delay of 6.6 ps/mm if the light travels back and forth between the retroreflector and the stationary mirrors. The delay line must thus be able to move in tens of micrometer increments to achieve the same resolution as the pulse width of the femtosecond laser, which sets the limit for how fast a physical process can be resolved.

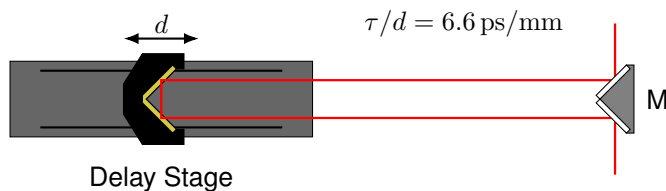


**Figure 3.2:** Illustration of mechanical delay line; a retroreflector mounted on a motorized translation stage. Each  $10 \mu\text{m}$  of distance adds approximately 66 fs of delay time between the pump and the probe. Stationary mirrors are included to bring the beam back to its original trajectory.

The pulses arrive at regular intervals, given by the repetition rate of the laser source, and is typically on the order of milliseconds to nanoseconds. Since the repetition period is many orders of magnitude lower than characteristic relaxation times, the material can be considered to be in thermal equilibrium before each new pair of pump and probe pulses arrive. Repeated measurements with varying pump-probe separation time is thus effectively equivalent to taking successive snapshots of the average response across the interaction region. The measurements can be stitched together to obtain the excitation and relaxation dynamics. This is illustrated in figure 3.4.

The high spatial resolution of the scanning process translates to a sampling frequency of several THz in the time-domain. It is important to distinguish between the optical sampling rate (the minimum delay time-separation between two measurements) and the electronic sampling rate. The electronic measurement of the signal is sampled orders of magnitude below the optical sampling frequency. As long as the electronic sampling is fast enough to resolve two consecutive laser pulses, the optical sampling is independent of the electronic sampling. The *response time* of the detector impulse response limits how quickly a pulse can be resolved, which is typically in the order of a few microseconds. Additionally, each sampled pump-probe delay time must be maintained until enough pulses arrive to stabilize the lock-in amplifier (see section 3.5.9). This only limits the minimum time required for a measurement series, and not the optical sampling frequency. Instead,



**Figure 3.3:** Delay line with stationary mirrors and retroreflector.

the optical sampling is limited entirely by the pulse width of the laser, and the step length of the delay stage.

The peak appearing in the pump-excitation phase of figure 3.4 is known as the coherent artifact, and is related to the autocorrelation of the pulses rather than the dynamics of the material. This artifact is present in the signal as long as the pump and probe originate from the same source (assuming no dispersion). The coherent artifact can be deconvoluted from the signal in post processing, provided that the autocorrelation of the laser source is known.

### 3.2.3 Signal, Noise and Dynamic Range

As with all electronics and optics, measurements are subject to various sources of noise. The term *noise* is used to describe any part of the measured signal that is undesirable, and in general, unpredictable. The noise floor fundamentally limits the detection, because the signal has to be distinct from the noise in order to be detectable. Considerable steps have been taken to ensure that the signal is lifted out of the noise, including heterodyne detection, the use of chopper wheels and a lock-in amplifier, and averaging of consecutive measurements. The lock-in amplifier allows very small signals to be extracted from the noise, because, even though the magnitude of the signal may be low, the amplitude in the frequency domain at the signal frequency is relatively stable in time (unlike the noise, which has amplitudes in the frequency domain that vary randomly in time). These steps are described further in section 3.5.

The quality of a signal is often expressed in terms of the signal-to-noise ratio (SNR) or dynamic range (DR). They are defined as follows [25]:

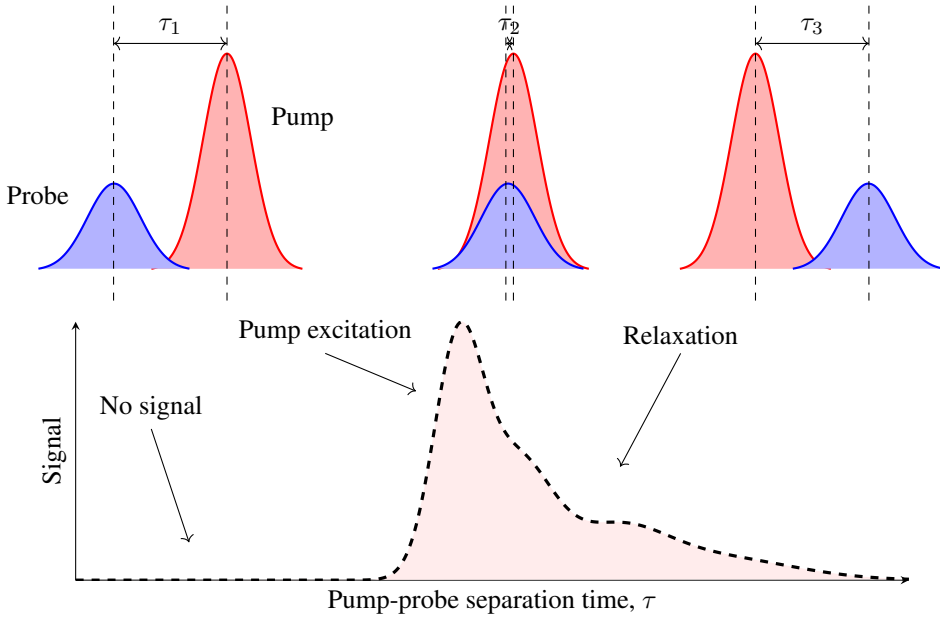


**Figure 3.4:** Illustration of pump-probe spectroscopy (pulses are represented by their intensity envelope). The probe is delayed in time with a variable delay line. The probe records different regimes according to the delay time.  $\tau_1$ : probe arrives before pump and measures no signal (only the noise),  $\tau_2$ : probe arrives together with pump, and measures the excitation by the pump,  $\tau_3$ : probe arrives after pump and measures relaxation in the material. The dashed curve illustrates a typical signal obtained from pump-probe spectroscopy.

- SNR: The average of the measured signal in time, divided by the standard deviation of the measured signal

$$SNR = \frac{\langle P \rangle}{\sigma_P}. \quad (3.1)$$

- DR: The maximum measured signal divided by the dark noise, that is, the standard deviation of the measured signal when no signal is present

$$DR = \frac{\max(P)}{\sigma_{DN}}. \quad (3.2)$$

In pump-probe, the dark noise is measured before the pump and probe overlap, the region labeled *no signal* in figure 3.4.

Both metrics are used throughout the discussion, but DR is primarily used in the results.

## 3.3 OKE Spectroscopy

### 3.3.1 Introduction

OKE spectroscopy is based on the optical Kerr effect, explained in section 2.4.6, in which a strong pump beam and a weak probe beam cross-couple inside a nonlinear medium. Equations (2.89) and (2.90) give the relationship between the refractive index experienced by the probe and the intensity of the pump. For simplicity, the equations were derived in one dimension. In three dimensions however, they become directionally dependent, such that the change in refractive index occurs along the direction of polarization of the pump. The pump excitation induces an anisotropic phase shift, which invokes a material birefringence (see section 2.4.2). The birefringence induces depolarization of the probe (see section 2.3.3). The time-resolved depolarization and recovery is measured to obtain the OKE signal. The OKE signal represents the time-domain impulse-response function, corresponding to the third-order susceptibility in the frequency domain. The distinction between time and frequency-domain response functions was made explicit in section 2.4.7. The third-order susceptibility can be obtained through the Fourier transform. The frequency of low-level modes are contained within the imaginary part of the third-order susceptibility, typically corresponding to vibrational or rotational modes (or sometimes librations in liquids), as explained in section 2.5.5.

### 3.3.2 Measurement

Depolarization of the probe is only observed when the pump is polarized at an angle, due to the anisotropic phase shift. Different schemes have been developed towards this end [18]. Our system utilizes the conventional  $45^\circ$  polarization arrangement, in which the probe is polarized along the x-axis, and the pump at a  $45^\circ$  angle. This is illustrated in figure 3.5.

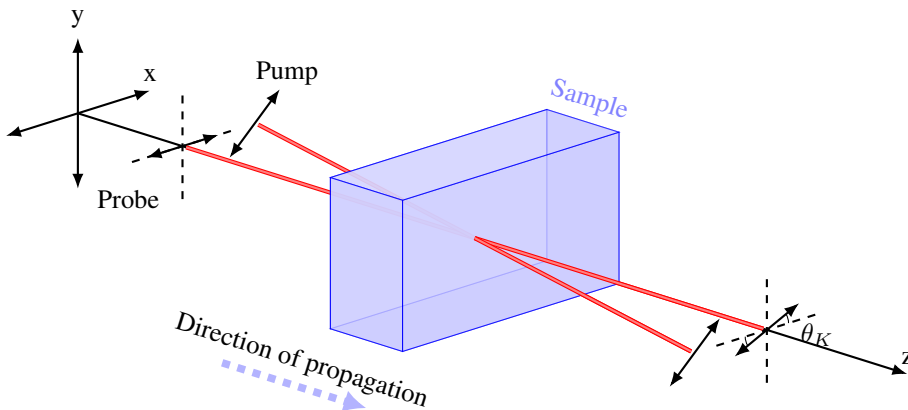


**Figure 3.5:** Illustration of OKE spectroscopy. The probe is polarized along the x-axis, and the pump is polarized  $45^\circ$  with respect to the x-axis. The two beams spatially overlap inside the sample. Rotation of the polarization is measured by the Kerr angle  $\theta_K$ .

The initial probe polarization state can be mathematically separated into two perpendicular components along a  $45^\circ$  axis, one of which is perpendicular to the pump and one of which is parallel. Each component sees a different refractive index, due to the presence of the pump. In the formalism of Jones, the sample is equivalently represented by the Jones matrix of a wave plate, with its fast axis along the direction of the pump [26]. The tilted wave plate matrix can be found by applying the similarity transformation (2.32)

$$\mathbf{T}_{Sample} = \mathbf{R}(45^\circ)\mathbf{T}_{WP}(\Gamma)\mathbf{R}(-45^\circ) \quad (3.3)$$

$$\mathbf{T}_{Sample} = \begin{bmatrix} \cos \frac{\Gamma}{2} & -i \sin \frac{\Gamma}{2} \\ -i \sin \frac{\Gamma}{2} & \cos \frac{\Gamma}{2} \end{bmatrix}. \quad (3.4)$$

The phase delay  $\Gamma$  is given by [27]

$$\Gamma(t) = \frac{\omega L}{c_0} \Delta n(t) \quad (3.5)$$

where  $\Delta n(t)$  is the OKE-induced index of refraction and  $L$  is the length of the interaction region between the pump and probe inside the nonlinear medium. The total Jones matrix for the sample and balanced detector (see section 3.5.8) is then  $\mathbf{T}_{Detector}\mathbf{T}_{Sample}$ . With the probe initially (before sample) polarized along the x-direction, the Jones vector from the output of the system is [26]

$$\mathbf{T}_{Detector}\mathbf{T}_{Sample} \begin{bmatrix} 1 \\ 0 \end{bmatrix} = \begin{bmatrix} \cos \frac{\Gamma}{2} - \sin \frac{\Gamma}{2} \\ -i \cos \frac{\Gamma}{2} - i \sin \frac{\Gamma}{2} \end{bmatrix} \quad (3.6)$$

which produces a signal proportional to  $\sin \Gamma$  from the output of the detector.

### 3.3.3 Analysis of the OKE Signal

Figure 3.6 shows an example of an OKE signal, obtained from deionized (DI) water (results are given in more detail in chapter 4). The main peak centered around 1.85 ps is the coherent artifact. It is directly related to the instantaneous, electronic response of the material as the pump and probe temporally and spatially overlap within the sample. The magnitude of the peak depends on the second-order refractive index and the intensity of the pump. The third-order susceptibility can be extracted from the measurement, by comparing the magnitude of the peak to that of a known reference<sup>2</sup>.

The relaxation process can be observed in the asymmetry of the peak (water has a relatively short relaxation time, and is more clearly seen in the logarithmic plot shown in the inset). A second, much smaller, peak can be observed around 12 ps. The separation between the two peaks are 10.30 ps, which corresponds to a distance of 1.54 mm, as explained in section 3.2.2. However, since the wave travels through water, the effective distance traveled is the physical distance multiplied by the refractive index, which for water is 1.329 at 800 nm wavelength [28]. The effective distance is therefore 2.05 mm, which corresponds to precisely twice the thickness of the cuvette used to hold the water

<sup>2</sup>A reference is in principle not necessary, provided that the transfer functions of the detector and amplifier are known. This is however a complicated calculation, and is greatly simplified by the use of a reference.

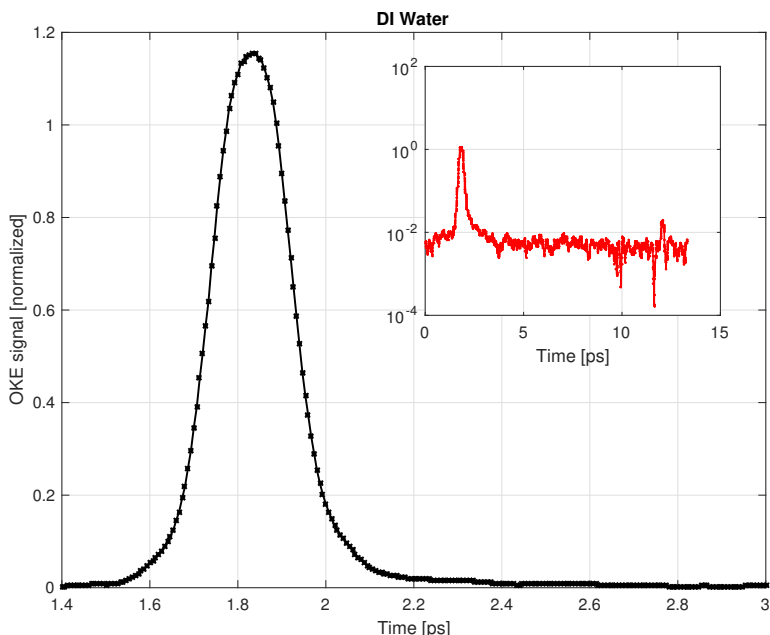


**Figure 3.6:** OKE signal from deionized (DI) water. The inset shows the full signal on a logarithmic scale. A second peak can be observed around 12 ps due to Fabry-Perot reflections.

sample. It can therefore be concluded that the second peak arises due to internal reflections (i.e. Fabry-Perot reflections) at material interfaces, such as from the cuvette with liquid samples, or thinfilm boundaries in solids (the effective traveled distance is twice the physical distance, since the reflected wave travels back and forth between the cuvette walls). The signal should therefore be cropped to remove the secondary peak before analyzing the signal. The samples that have been studied in this thesis have all been sufficiently thick, such that thermal equilibrium has been reached before secondary peaks have occurred. This might however present itself as an issue with thinner samples, or materials with long relaxation times.

As explained in section 2.5.5, the spectrum of the time-resolved OKE signal contains information about the vibrational and rotational modes of the molecules. This was illustrated in figure 2.16, where the imaginary part of the susceptibility was shown to have a peak centered around the transition frequency  $\Omega$  for a material with a single vibrational level. In practice, materials tend to have several resonances in close proximity, and the measured signal is therefore the sum of several peaks. Disentangling the peaks is a challenge, and made all the more complicated by the fact that they often do not display purely Gaussian or Lorentzian line shapes, but are observed as more complicated asymmetric functions, such as the antisymmetrized Gaussian or the Bucaro-Litovitz function [29].

McMorrow and Lotshaw devised a method to extract the Raman modes from the OKE signal. Following the derivation given in their 1988 paper [27], the transmitted OKE signal in a heterodyne-detection scheme is given by



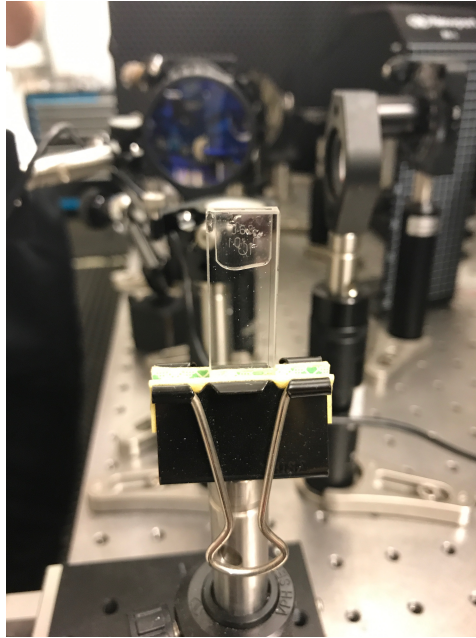


**Figure 3.7:** Cuvette with DI water used in the measurement presented in figure 3.6. The inner thickness is 1 mm, which corresponds to half of the effective distance traveled between the first and second peak.

$$T(\tau) = \int_{-\infty}^{\infty} I_{probe}(\tau - t) \{1 + \sin[\Gamma(t)]\} dt \quad (3.7)$$

where  $\tau$  is the pump-probe separation time, and  $\Gamma(t)$  is the phase delay described in the previous section, proportional to  $\Delta n(t)$ .

When the dynamic responses occur on separable time-scales, the second-order refractive index can be expressed as a superposition of the individual responses

$$\Delta n(t) = \sum_m \Delta n_m(t) \quad (3.8)$$

$$= \sum_m \int_{-\infty}^{\infty} I_{pump}(t') r_m(t - t') dt' \quad (3.9)$$

where  $r_m(t)$  is the  $m$ th contribution to the third-order response function  $R_{ijkl}(t)$ . Inserting (3.9) into (3.7) yields

$$T(\tau) = \sum_m \int_{-\infty}^{\infty} G_0^{(2)}(t) r_m(\tau - t) dt \quad (3.10)$$

where  $G_0^{(2)}(t)$  is the zero-background autocorrelation of the laser. In deriving the final equation, the constant term in the integral was dropped because it is not detected when

chopping the pump. Additionally, the sine term was simplified by the approximation  $\sin x \approx x$  for small angles.

The third-order nonlinear impulse response function can be separated into an instantaneous electronic contribution and several non-instantaneous nuclear contributions. If all optical frequencies lie well below any electronic absorption, the response function can be expressed as [30]

$$\Phi_{ijkl}(t) = \sigma_{ijkl}(t) + \Phi_{nuc}(t) \quad (3.11)$$

where  $\sigma_{ijkl}(t)$  is the purely electronic hyperpolarizability, and is instantaneous on the time-scale of the laser;

$$\sigma_{ijkl}(t) = b\delta(t) \quad (3.12)$$

where  $b$  is a scalar constant.  $\Phi_{ijkl}(t)$  is related to the third-order susceptibility  $\chi^{(3)}$  through the Fourier transform, and is a complex function in the time-domain

$$\Phi_{ijkl}(t) = \Phi_{ijkl}^{Re}(t) + i\Phi_{ijkl}^{Im}(t). \quad (3.13)$$

As derived by McMorro and Lotshaw [30], a heterodyne detection scheme can be made to produce a signal given by

$$T(\tau) = \int_{-\infty}^{\infty} G_0^{(2)}(\tau - t)\Phi_{ijkl}^{Re}(t) dt \quad (3.14)$$

which is simply the convolution of the autocorrelation function and the impulse response function

$$T(\tau) = G_0^{(2)}(\tau) * R_{ijkl}(\tau). \quad (3.15)$$

We define the function  $D_{ijkl}(\omega) = \mathcal{F}\{R_{ijkl}(t)\}$  to be the frequency-domain representation of the impulse response function, where  $\mathcal{F}\{f(t)\}$  represents the Fourier transform

$$\mathcal{F}\{f(t)\} = \int_{-\infty}^{\infty} f(t)e^{i\omega t} dt. \quad (3.16)$$

The duality between convolution in the time-domain and multiplication in the frequency-domain leads to the result

$$D_{ijkl}(\omega) = \mathcal{F}\{R_{ijkl}(t)\} \quad (3.17)$$

$$= \frac{\mathcal{F}\{G_0^{(2)}(t)\}\mathcal{F}\{R_{ijkl}(t)\}}{\mathcal{F}\{G_0^{(2)}(t)\}} \quad (3.18)$$

$$= \frac{\mathcal{F}\{T(t)\}}{\mathcal{F}\{G_0^{(2)}(t)\}}. \quad (3.19)$$

(3.19) is a highly applicable result, because both  $T(t)$  and  $G_0^{(2)}(t)$  are directly measurable in the experiment.  $G_0^{(2)}(t)$  is commonly referred to as the instrument function. Obtaining

an exact instrument function can be experimentally challenging, and a suitable alternative is to use a Gaussian curve fit for a select time-window of  $T(t)$  to approximate the function.

In summary, the detected OKE signal  $T(t)$  can be Fourier transformed and divided by the instrument function (i.e. the Fourier transform of the autocorrelation of the laser) to obtain the frequency-domain function  $D_{ijkl}(\omega)$ . The inverse Fourier transform of  $D_{ijkl}(\omega)$  yields the time-domain impulse response function with the electronic contribution deconvoluted. The real and imaginary parts of  $D_{ijkl}(\omega)$  should only contain the nuclear contributions, and as shown by [30], the resulting components are

$$\text{Im}\{D_{ijkl}(\omega)\} = \text{Im}\{\mathcal{F}\{R_{nuc}(t)\}\} \quad (3.20)$$

$$\text{Re}\{D_{ijkl}(\omega)\} = b + \text{Re}\{\mathcal{F}\{R_{nuc}(t)\}\}. \quad (3.21)$$

The Raman spectrum is therefore contained within the imaginary part of  $D_{ijkl}(\omega)$ .

### 3.3.4 The Third-Order Susceptibility

The third-order susceptibility is more easily obtained by comparing a results to a known reference, measured with the same experimental conditions. The third-order susceptibility of the unknown sample is related to the reference sample through the expression [31]

$$\chi_s^{(3)} = \chi_r^{(3)} \left(\frac{I_s}{I_r}\right)^{1/2} \left(\frac{I_{r,pump}}{I_{s,pump}}\right)^{3/2} \left(\frac{n_s}{n_r}\right)^2 \frac{\alpha L}{e^{-\alpha L/2}(1 - e^{-\alpha L})} \quad (3.22)$$

where  $I_s$  and  $I_r$  is the peak signal for sample and reference respectively,  $I_{s,pump}$  and  $I_{r,pump}$  is the pump power,  $n_s$  and  $n_r$  is the linear refractive index,  $\alpha$  is the absorbance and  $L$  is the length of the interaction region.

Since the third-order susceptibility depends strongly on the pump intensity, reflections occurring at interfaces of media with different refractive index must be taken into account. The transmitted pump power is scaled by a factor  $T = 1 - R$ . When the light is transmitted from air,  $R$  is given by [32]

$$R = \frac{(1 - n)^2 + \kappa^2}{(1 + n)^2 + \kappa^2} \quad (3.23)$$

where  $n$  is the refractive index of the medium, and  $\kappa$  is the reflection coefficient.

A topic that has not yet been addressed is which of the elements in the third-order susceptibility tensor that is probed by the measurement. The nonlinear polarization contributions from OKE can be found by resolving the summation in (2.74) with the pump and probe polarizations illustrated in figure 3.5. Due to symmetry considerations, 60 of the 81 tensor elements are zero in an isotropic medium, and it follows that the elements of the tensor where an index repeats an odd number of times must vanish. For more details on symmetry relations, see Boyd [5]. The resulting polarization contributions are

$$P_x^{(3)}(\omega_1) = \frac{3}{2} \epsilon_0 (\chi_{xxxx} E_x(\omega_2) E_x^*(\omega_2) E_x(\omega_1) + \chi_{xyyx} E_y(\omega_2) E_y^*(\omega_2) E_x(\omega_1)) \quad (3.24)$$

$$P_y^{(3)}(\omega_1) = \frac{3}{2} \epsilon_0 (\chi_{xyyx} E_x(\omega_2) E_y^*(\omega_2) E_x(\omega_1) + \chi_{yyxx} E_y(\omega_2) E_x^*(\omega_2) E_x(\omega_1)). \quad (3.25)$$

When the signal is measured along the y-direction, the measurement effectively probes two tensor elements, and the two cannot be separated. There are two ways to interpret this: either it can be assumed that the measurement is an average of the two tensor elements, or it can be assumed that the two elements are the same. The latter is known as *intrinsic permutation symmetry* (IPS). The interpretation is a matter of definition.

## 3.4 MOKE Spectroscopy

### 3.4.1 Introduction

MOKE spectroscopy is based on the longitudinal magneto-optical Kerr effect described in section 2.7. The detection of the Kerr rotation angle  $\theta_k$  is based on the scheme used in [33], but the crossed polarizers have been replaced with a balanced detector. Measurement of the Kerr ellipticity is not currently supported. Magnetization of the ferromagnetic sample is achieved by a neodymium magnet mounted to a translation stage. By varying the distance between the sample and magnet, the magnetic field strength is tuned.

The hysteresis of the ferromagnet can be mapped by varying the magnetic field strength. In this measurement, only the probe beam is in use, and a secondary chopper is used to provide a reference to the lock-in amplifier. This is explained in section 3.5.5. The pump is used to optically demagnetize the ferromagnet, and the pump-probe technique is used to measure the demagnetization and recovery transient.

### 3.4.2 Measurement

The experimental setup is based on the L-MOKE geometry, illustrated in figure 3.8. It is assumed that the magnetic field is parallel to the surface of the sample, such that no contribution exists from the polar and transverse MOKE, as well as from magneto-optical anisotropy, as discussed in section 2.7.5.

The first objective in designing the MOKE was to measure the magnetic hysteresis, as proposed by ???. If a hysteresis measurement is obtained by solely varying the magnetic field, the signal is guaranteed to originate purely in the magnetic response, and not in some other latent effect. Since ferromagnetic samples have hysteresis, the magnetic contribution should be reflected in the symmetry-breaking of the MOKE signal under reversal of the magnetic field.

The hysteresis measurement uses the probe beam directly to measure the magnetization. The signal is therefore independent on any time variable, and is in the form of a DC signal. The magnetic field used to magnetize the sample is the only factor that changes with time. Control of the magnetization is achieved by a neodymium magnet mounted to a

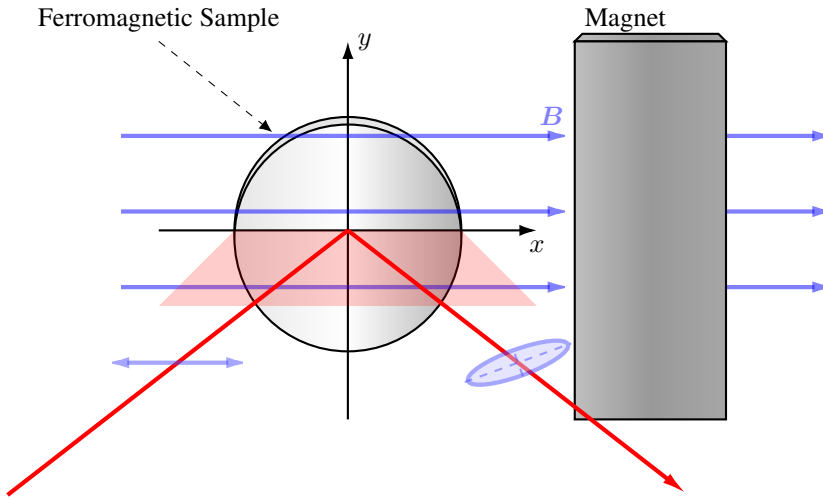


**Figure 3.8:** Experimental setup of MOKE (probe only). The magnet sits next to the sample and magnetizes the sample in the longitudinal direction. The magnetization of the sample is assumed to be locked completely in the longitudinal direction.

linear translation stage. Since the field strength diminishes with distance, the sample can be probed under different field strength by simply moving the magnet, and by rotating the magnet  $180^\circ$ , the direction of the field can be reversed. The magnetic flux density can be measured with a Gaussmeter (which utilizes the Hall effect) to calibrate the MOKE signal to the magnetic flux density.

The neodymium magnet was proposed as a first-iteration solution to the magnetic field issue, and the intention was to replace this with an electromagnet in the future. The current solution has lower accuracy and directivity than what could be achieved with an electromagnet. Another apparent problem is the inability to completely nullify the magnetic field, and smoothly reverse the direction. These issues are further addressed in section 5.3.2.

The MOKE angle  $\theta_k$  is measured with a balanced detector. Measuring the ellipticity is not supported at the time of writing. The signal therefore corresponds to the real part of the complex Voigt vector, which as shown in (2.160) is proportional to the magnetization  $\text{Re}\{\hat{\Theta}_k\} \propto M_x$ .

In order to measure the hysteresis, the sample must undergo a magnetic cycle. This is achieved by first saturating the sample in one direction, and then varying the field back down to zero. This ensures that the sample is left in a remanence state. From this point, the sample must be saturated in the opposite direction by reversing the direction of the field and ramping the field strength up to a maximum. Once saturated, the field must be reversed back to zero, to enter the remanence state in the opposite direction. The field should then be ramped to a maximum in the original direction and brought back to zero. This ensures complete mapping of the hysteresis cycle. The process is illustrated in figure 3.9. As previously mentioned, the magnetic flux density  $B$  is scanned by translating the neodymium magnet. Since the magnet has to be physically rotated in order to reverse the

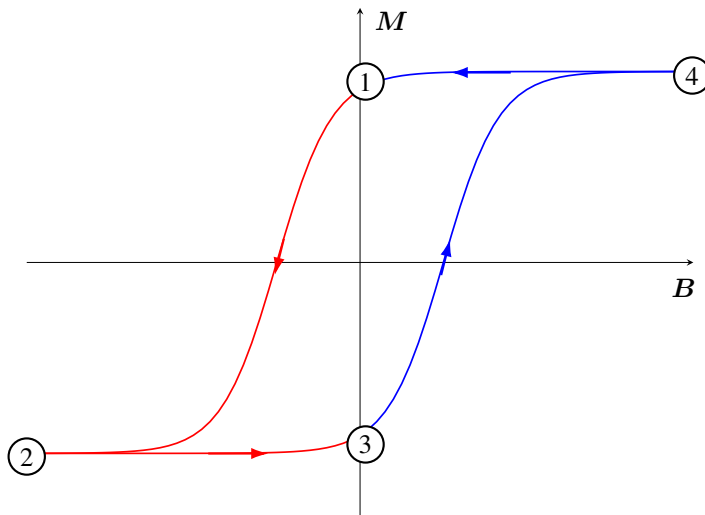


**Figure 3.9:** Procedure for magnetic cycling. The red curve shows the first half of the cycle, and the blue curve shows the second half. The sample must initially be saturated in one direction and then left in a remanence state (1). The field is then reversed and varied from zero (1) to saturation (2) and back to zero (3). The direction is then reversed again, and varied from zero (3) to saturation in the opposite direction (4) and back to zero (1). (1) and (3) marks the points where the magnet must be reversed, and (2) and (4) marks the saturation regions, which corresponds to the maximum backwards and forwards field strengths.

field, two scans are required for complete mapping. The two scans are illustrated by the red and blue curves in figure 3.9.

In order to calibrate the measured MOKE signal, the magnetic flux density must be measured in place of the sample, as shown in figure 3.11 a. This is achieved by removing the sample and installing a Hall effect sensor. A total of four scans is therefore necessary for each measurement; two scans to calibrate the magnetic flux density and two scans to measure the MOKE signal.

The hysteresis measurement is performed in the following steps:

1. The sample is placed in the sample holder.
2. The magnet is translated parallel to the sample surface from far away, until the sample is saturated along the longitudinal direction.
3. The magnet is translated back, and rotated  $180^\circ$
4. The magnet is stepped in small increments, along the full range of the motor.
5. Once fully stepped, the direction is reversed and the stepping is retraced in the backwards direction.
6. Once the magnet is back to the starting point, it is rotated  $180^\circ$ .

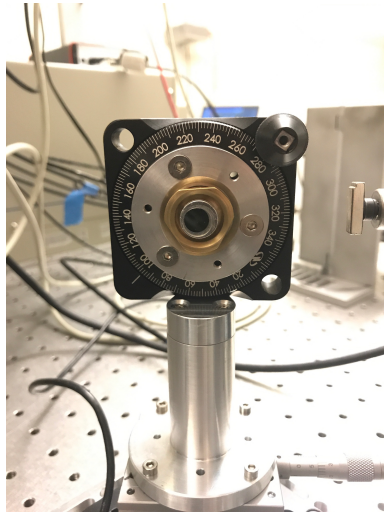


**Figure 3.10:** MOKE holder with permalloy sample. The magnet can be seen to the right.

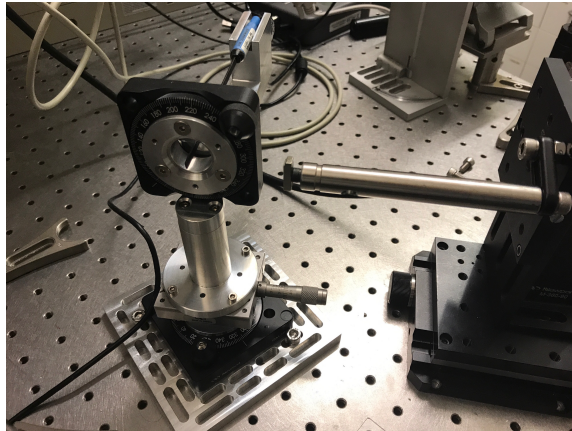
7. Steps 4 and 5 are repeated.
8. The sample is removed and replaced with the Hall probe. The sample holder has been made with a trace to align the Hall probe, such that it overlaps with where the sample would be.
9. Steps 4 to 7 are repeated with the Hall probe in place of the sample.

### 3.4.3 Time-Resolved MOKE Spectroscopy

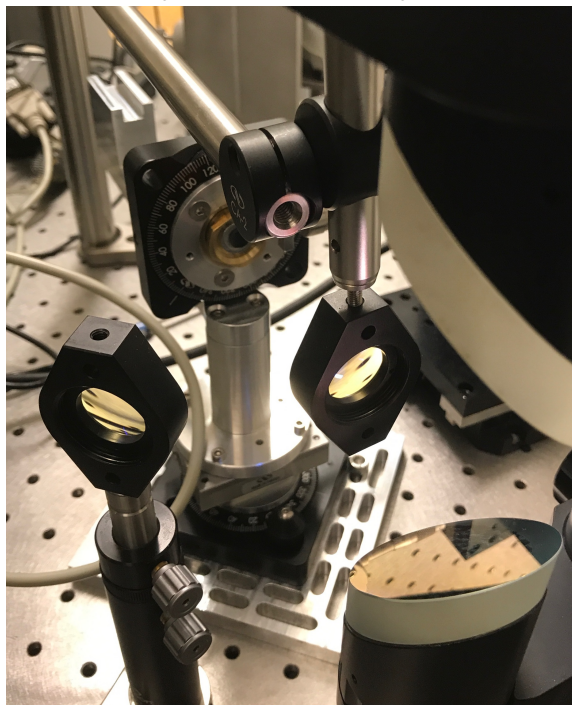
Up until now, MOKE has been discussed in terms of the probe beam only. When the pump is included, it is possible to achieve time-resolved measurements of the magnetization dynamics, i.e. time-resolved MOKE (TR-MOKE). The detection scheme is similar to OKE, but the mechanism behind the process is somewhat different; OKE is caused by the interaction of two beams, and it therefore makes less sense to view the contribution from each beam as separate. In MOKE however, the probe continuously measures the magnetization. The pump is included to optically demagnetize the medium, and the time-resolved signal is therefore the transient behavior of the demagnetization phase and recovery of the magnetization to the static field supplied by the magnet.

Figure 3.11b shows the sample holder with the pump aimed at the sample. The tilted mirrors shown to the right are used to bring the pump beam up into a higher plane and back down to the laser plane. This was designed to compensate for the extra distance added to the probe as it is shifted over to the MOKE sample holder, such that temporal overlap of the two beams is achievable within the scan range of the delay line.

The TR-MOKE signal can be divided into two contributions,  $\Delta\psi = \Delta\theta + \Delta b$ , where  $\Delta b$  represents pump-induced effects that are even in magnetization, such as optical Kerr



(a) MOKE holder with Hall effect probe installed for calibration. The magnet can be seen to the right.



(b) Setup for TR-MOKE spectroscopy. The pump is focused by a lens onto the sample. The angle of incidence is normal to the sample surface.

**Figure 3.11:** MOKE spectroscopy sample holder.



effect and other nonlinear effects.  $\Delta\theta$  represents the signal from magnetic effects, and can be isolated by plotting the difference [34]

$$\Delta\theta = \frac{\Delta\psi(M) - \Delta\psi(-M)}{2}. \quad (3.26)$$

## 3.5 The OKEMOKE System

### 3.5.1 Introduction

This section covers the technical details of the OKEMOKE system from the generation of the laser pulses to detection of the signal. An overview is given in the next section, followed by a detailed description of each segment in the consecutive sections.

### 3.5.2 Overview

The system is illustrated in figure 3.12. Additional mirrors and beam splitters are placed in between the laser source and the system, to provide a beam to a second THz system present in the laboratory. All mirrors, lenses, beam splitters, variable attenuators and beam stoppers are provided by Newport Instruments, and are high-end components specially chosen to match the laser source. Sample holders, stationary mirror holders and other mechanical constructions not specified are custom made parts, provided by a machine shop at the university. The rest of the components are listed in table 3.2.

### 3.5.3 The Laser Source

Laser light is provided by the Solstice Laser Amplification System from Spectra Physics [35], depicted in figure 3.13. The system contains two class IV laser sources: a *Mai Tai* mode-locked Ti:Sapphire seed laser, and an *Empower* Q-switched, frequency-doubled Nd:YLF pump laser, used to supply energy to the amplifier. The Solstice also contains a regenerative amplifier and a pulse stretcher/compressor. Low-power femtosecond pulses are generated by the mode-locked seed laser. The pulses are passed through a pulse stretcher to broaden the energy distribution in time. The stretched pulses are passed through a Ti:Sapphire rod pumped by the Q-switched laser, to amplify the pulse power. Stretching the pulses in time lowers the peak-power, which prevents damage to the crystal. The amplified pulses are then compressed to regain, as close as possible, the original pulse width. The system outputs pulses with a repetition rate of 1 kHz and an average power of 3.5 W. The width of each pulse is between 70 fs and 100 fs.

The temporal pulse width is closely related to the bandwidth. For Gaussian pulses, the pulse width and bandwidth obey the uncertainty relation

$$\Delta\nu\Delta t > 0.441 \quad (3.27)$$

where  $\Delta\nu$  is the bandwidth and  $\Delta t$  is the pulse width.

**Table 3.2:** Components of the OKEMOKE system.

Component	Part Name	Manufacturer
Laser source	Solstice Laser Amplification System	Spectra Physics
Detector	Autobalanced Detector ABL-NXT	Zomega Terahertz
Lock-in amplifier	SR830 DSP Lock-In Amplifier	Stanford Research Systems
Oscilloscope	DPO2014 Digital Phosphor Oscilloscope 100 MHz, 4-Ch, 1GS/s	Tektronix
Polarizers	10GL08AR.16 Glan-Laser Calcite Polarizer	Newport
Delay stage motor	M-ILS100CC Mid-Range Travel Linear Stage	Newport
Delay stage controller	ESP301 3-Axis Motion Controller and Driver	Newport
Primary chopper	MC2000 Optical Chopper System	Thorlabs
Secondary chopper	SR450 Chopper Controller	Stanford Research Systems
Gaussmeter	Model 5080 Gauss/Tesla meter	Pacific Scientific OEKO

### 3.5.4 Pump-Probe Generation

A 90/10 beam splitter is used to generate the pump and probe beams from the laser source. The beam splitter is a partially reflective mirror that reflects about 10% of the incident power and transmits 90%. The pump-probe generation is shown in figure 3.14. Both beams are passed through variable attenuators, to enable tuning of the beam power. The variable attenuators are thin sheets of material with spatially varying absorption. By moving an attenuator in relation to the beam, the degree of absorption, and consequently the transmitted power, can be adjusted. The average power of each beam can be measured with a power meter. It should be noted that, due to limitations in space, it is easier to measure the transmitted power after the beam is passed through the choppers (see next section). Since the duty cycle of the choppers is 50%, the measured power is half of the actual power. To obtain the actual power of each beam, the measured power should be multiplied by a factor of two, or measured with the choppers stopped.

The pump and probe are passed through linear glan-laser calcite polarizers with an

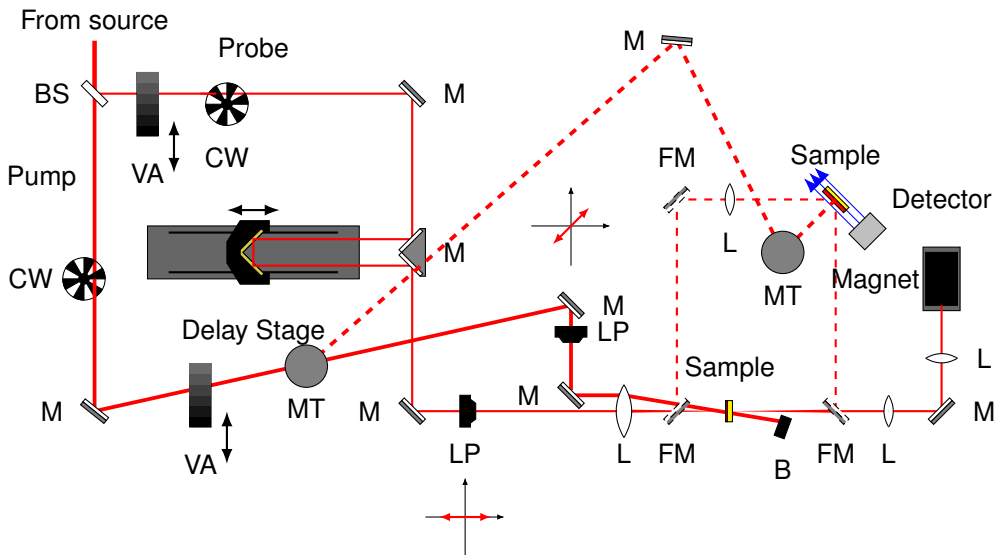


**Figure 3.12:** Illustration of the OKEMOKE system. Polarization states are indicated next to polarizers. The dashed line shows the trajectory of the beams when the flip mirrors and mirror towers are raised, and the solid line when the mirrors are lowered. The blue arrows illustrate the static magnetic flux density. **B:** Beam Stopper, **BS:** Beam Splitter, **CW:** Chopper Wheel, **FM:** Flip Mirror, **L:** Lens, **LP:** Linear Polarizer, **M:** Mirror, **MT:** Mirror Tower, **VA:** Variable Attenuator.

extinction ratio of  $10^{-5}$ . This provides a very clean and well defined polarization state. The polarization are oriented to produce the polarization shown in figure 3.5.

### 3.5.5 The Chopper Wheels

A chopper wheel is a rotating disk with alternating windows and shutters, that periodically interrupts the laser beam. This causes the detected signal to be modulated by a reference frequency. The measurement can be synchronized to the reference frequency by a lock-in amplifier to reject noise at other frequencies, which greatly improves the signal to noise-ratio. The lock-in amplifier is explained in detail in section 3.5.9.

The chopper wheel is connected to a chopper controller, which can be used to set the chopping frequency. The term *chopping frequency* refers here to the number of interruptions performed by the chopper per second, which differs from the rotational frequency of the chopper wheel, since there is more than one window on the disk. The chopper controller receives a signal synchronized to the chopping frequency, measured in the chopper wheel (typically by an optical encoder).

The *duty cycle* of the chopper is the ratio of the physical length of a window to the length of a full period, i.e. the length of a window plus the length of a shutter (alternatively, one may define it in terms of the shutter rather than the window). The chopper illustrated in figure 3.15 has a duty cycle of 50%.

The general idea behind the chopper wheel is to subtract the portion of the signal that

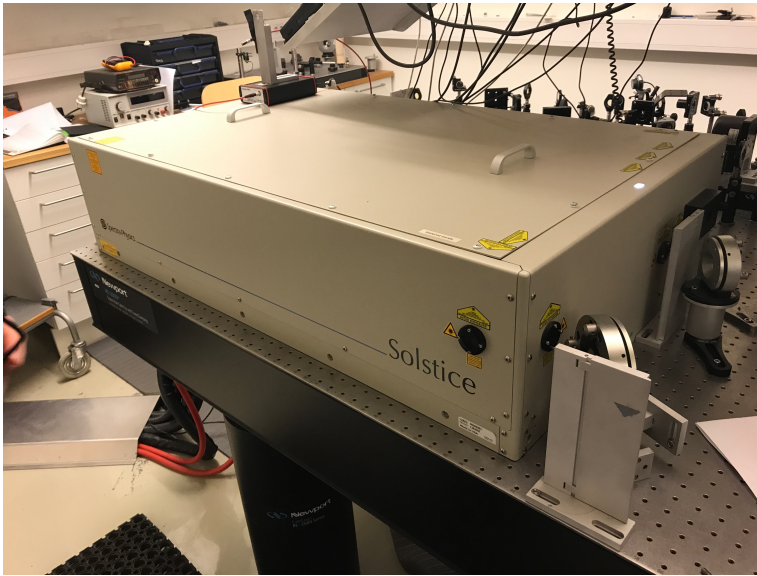


**Figure 3.13:** Solstice Laser Amplification System.

is measured when the laser is blocked by the shutters. When the pump beam is interrupted, the detected signal on the shutter flanks originates primarily from misalignments or imperfections in the system that prevents the probe signal from being completely extinguished, as well as from laser noise. In this scenario, the probe beam enters the detector unhindered, and should ideally produce no signal if the detector is calibrated for the unmodulated polarization state of the probe. This is in practice impossible to obtain, but by subtracting the portion of the signal taken on the shutter flanks from the portion obtained on the window flanks, the remaining part of the signal originates purely from the induced effect of the pump.

When the system is in MOKE mode, and used to measure hysteresis at thermal equilibrium, the probe must be blocked to avoid interference. In order to provide the reference signal, a secondary chopper has been installed in front of the probe beam. The secondary chopper modulates the probe beam, and the synchronized reference signal of the secondary chopper must be provided to the lock-in amplifier by interchanging the coaxial cables from the chopper controllers to the external reference input of the lock-in. When the probe is blocked on the shutter flanks, there should in principle be no light arriving at the detector. In this scenario, the only contribution to the detected signal is background noise. The SNR is improved by discarding this portion of the signal.

It is indeed possible to combine the two chopper wheels to further improve the SNR. The main source of noise rejected by the primary chopper stems from the imperfections in the system and the noise in the laser, but since every probe pulse is transmitted to the detector, any background noise follows with it. By also chopping the probe, the background noise can in principle be disentangled from the probe signal and laser noise, which in turn can be modulated by the primary chopper (i.e. the pump). If such a scheme is to

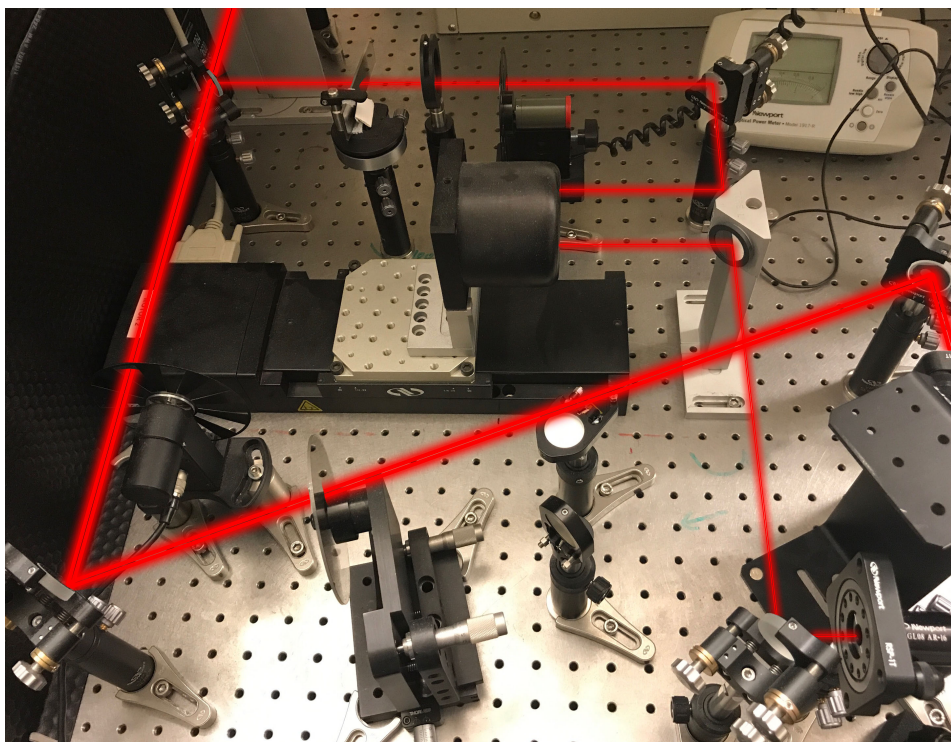


**Figure 3.14:** Generation of pump and probe beam. The probe is passed through a delay line, to adjust the temporal overlap.

be implemented, it seems reasonable to assume that the primary chopper should be run on half of the frequency of the secondary, which in turn should be close to half of the repetition rate of the laser. A pulse train would then encompass the following characteristics, assuming the pump and probe start off together: Signal (pump + probe)  $\Rightarrow$  background noise (no pump + no probe)  $\Rightarrow$  laser noise (no pump + probe)  $\Rightarrow$  background noise (no pump + no probe)  $\Rightarrow$  repeat. This possibility has however not been explored, and is left as a suggestion to future students who wish to improve the system.

The primary chopper is a Thorlabs MC2000, and the secondary is a Stanford Research Systems SR450. Both chopper wheels have a duty cycle of 50%. They are depicted in figure 3.16.

### 3.5.6 OKE/MOKE Mode Selection

OKE and MOKE spectroscopy utilize the same scheme to generate and detect pulses. They differ only in the way the pulses interact with the sample: OKE is done in transmission and MOKE is done in reflection, and under the presence of a magnetic field. The system therefore has two modes: OKE mode and MOKE mode. The modes are implemented by a series of flip mirrors, which, when in the upright position, bring the beams over to a parallel

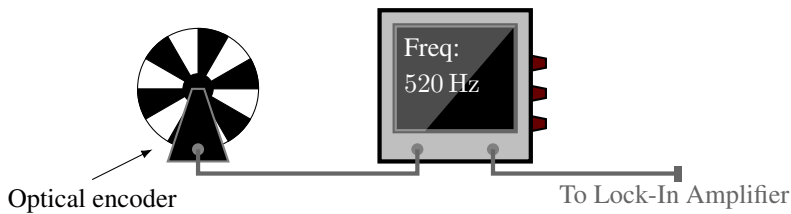
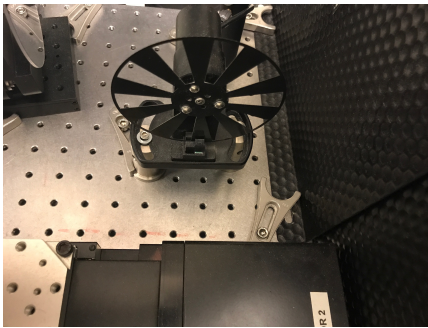
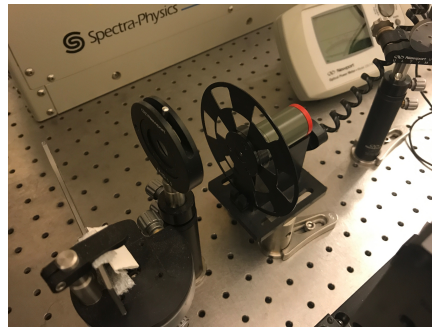


**Figure 3.15:** Optical chopper wheel, connected to chopper controller. The chopper controller is used to adjust and monitor the chopping frequency, and provides a reference signal to the lock-in amplifier. An optical encoder in the base of the chopper measures the chopping frequency.



(a) Primary chopper wheel (pump).



(b) Secondary chopper wheel (probe).

**Figure 3.16:** Thorlabs MC2000 and Stanford Research Systems SR450 chopper wheels, used to improve SNR.

setup and back again, to the detector. When all the mirrors are in the upright position, the system is in MOKE mode. The system was designed to be easily reconfigurable, since alignment of optics is a time-consuming process.

### 3.5.7 The Sample Holders

When the system is in OKE mode, the pump and probe are focused down to a spot by a lens, where they spatially overlap. This is illustrated in figure 3.5. After they pass through the sample, the pump is absorbed by a beam stopper. The probe is passed through a lens to collimate the beam, before it is passed through another lens with a short focal length and focused onto the aperture of the detector. Liquid samples can be poured into a thin cuvette, and solid samples can be taped to a piece of glass. The samples can then be clamped to the sample holder, which is mounted on a linear translation stage. The stage can be moved back and forth with high precision to fine-tune the alignment, such that the focal point of the beams overlap within the sample. Since the OKE measurement relies on a high degree of overlap between the beams, this alignment process is crucial for a good measurement. The spot-size of the beams is very small in the focal point of the lens, and the alignment should therefore be done with great care.

When the system is in MOKE mode, a series of flip mirrors are raised to bring the probe over to the other sample holder, and mirror towers are raised to bring the pump beam into an elevated plane, and then lowered to the original plane of the beam. The sample holder was custom made by a local machine shop at the university to allow a high degree of control over the measurement. A magnetic sample can be taped to a disk-shaped mount, originally used in electron microscopes. The sample can then be rotated a full  $360^\circ$ , which makes it possible to measure rotational symmetry properties of the sample. Furthermore, the sample holder can be translated back and forth along the  $45^\circ$  axis, to allow different parts of the sample to be examined. This makes it easier to locate local domains in the sample, as well as to observe changes in the measured signal from spatially varying optical coatings. The sample can be temporarily removed, to allow a magnetic Hall effect probe to be installed from the backside. The Hall effect probe can be used to measure the magnetic field where the sample would be, to calibrate the measurement. The magnetic field is supplied by a permanent neodymium magnet, which is mounted on a motorized translation stage next to the sample holder. The magnet can be moved back and forth to vary the strength of the magnetic field at the sample. The magnet can also be turned over to change the direction of the field. Before any MOKE measurement is done, a calibration should be performed with the Hall effect probe. The obtained MOKE signal can then be mapped to the measured magnetic field strength. The reflected MOKE probe is brought back to the same trajectory as the OKE probe, and the detection scheme is the same.

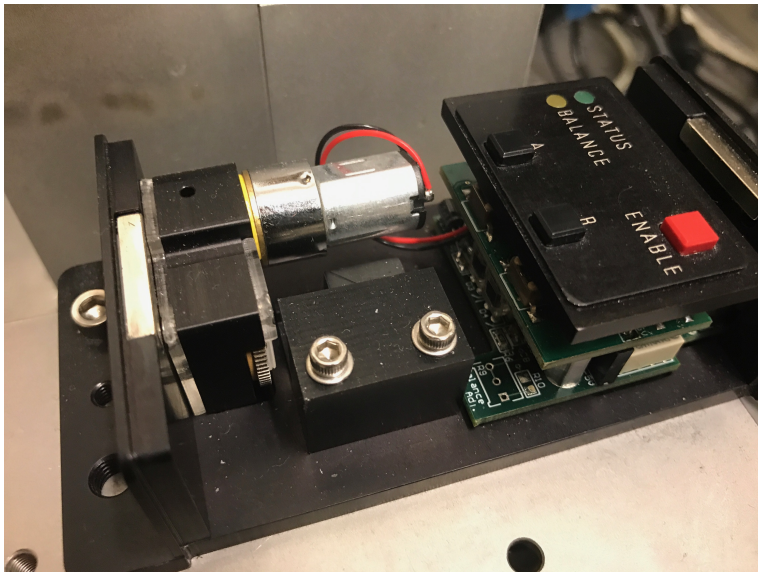


**Figure 3.17:** Balanced Detector with top lid removed. A motor sits next to the quarter wave plate, which allows the balance point to be shifted. The two photodiodes can be seen to the right.

### 3.5.8 Balanced Detection

A Zomega Terahertz ABL-NXT Autobalanced Detector is used to detect the polarization of the probe. The detector is shown in figure 3.17. This is a highly sensitive polarization detector, capable of detecting extremely small angles of rotation in the polarization state.

The probe enters the detector through a small aperture. From there, it is passed through a rotatable quarter wave plate (QWP) and a Wollaston prism. The Wollaston prism is a type of birefringent polarizer, made from two wedges of an anisotropic material with perpendicular optical axes [36]. The prism spatially separates the beam into two perpendicular components. Each of the two components is focused onto a photodiode which has a response that is quadratic in the amplitude of the field, and hence measures optical intensity. The difference in intensity is computed by the electronics in the detector, and transmitted as an analog signal through a coaxial cable. The cable is connected to a Tektronix DPO2014, 4 channel, 100 MHz, 1 GS/s oscilloscope and an Stanford Research Systems SR830 DSP lock-in amplifier.

A small motor in the detector can be used to rotate the QWP, and two buttons on the detector are used to increment or decrement the angle. The purpose of the QWP is to transform a linear polarization state into a circular one. Equation (2.32) can be applied to the Jones matrix for a wave plate, listed in table 2.3, with  $\Gamma = \pi/4$  (QWP). If the transformation angle is  $45^\circ$ , the similarity transformation is

$$\mathbf{T}_{QWP,45^\circ} = \mathbf{R}(45^\circ)\mathbf{T}_{WP}(\pi/4)\mathbf{R}(-45^\circ) \quad (3.28)$$

and the equivalent Jones matrix for the wave plate is

$$\mathbf{T}_{QWP,45^\circ} = \begin{bmatrix} 1 & -i \\ -i & 1 \end{bmatrix}. \quad (3.29)$$

Light polarized linearly along the x or y axis is transformed into circularly polarized light by the Jones matrix (3.29);

$$\begin{bmatrix} 1 & -i \\ -i & 1 \end{bmatrix} \begin{bmatrix} 1 \\ 0 \end{bmatrix} = \begin{bmatrix} 1 \\ -i \end{bmatrix}. \quad (3.30)$$

When the perpendicular components are separated by the Wollaston prism, and subtracted by the electronics, the output is zero;

$$\Delta I = I_{\parallel} - I_{\perp} = 0. \quad (3.31)$$

The detector can thus be zeroed by passing the probe directly to the detector (e.g. with the pump blocked), and by rotating the QWP until the signal drops to zero. This is referred to as the balance point. Any change in the polarization of the probe from the balance point results in a non-zero signal. The signal can be positive or negative, corresponding to clockwise or counter-clockwise rotation. This is thus a highly sensitive method for detecting rotation in the polarization state of the probe.

While the signal ideally should be zeroed at the balance point, it is in practice impossible to completely zero it out. The signal from the detector can be monitored on the



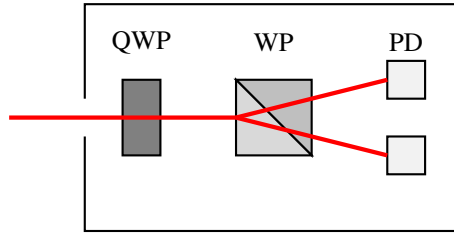


**Figure 3.18:** Illustration of balanced detector used to measure polarization of the probe. **QWP:** Quarter Wave Plate, **WP:** Wollaston Prism, **PD:** Photodiodes.

oscilloscope, and will typically appear as  $\sim 2\ \mu\text{s}$  pulses arriving with the chopping frequency. The pulse width of  $2\ \mu\text{s}$  stems from the impulse response of the photodiodes, since they clearly fail to follow the extremely short pulse width of the laser.

Since the fast axis of the wave plate is aligned along the polarization of the pump, the signal induced by the pump is placed into one polarization state, while the probe field gets evenly separated between both directions. After the polarization is separated by the Wollaston prism, one photodiode measures the square of the probe field, while the other measures the square of the sum of the probe field and the signal field. This is known as *heterodyne detection*, and the probe field is in this context referred to as the local oscillator. Subtraction of the measured values then yields

$$\Delta I \propto |E_{LO} + E_{sig}|^2 - |E_{LO}|^2. \quad (3.32)$$

The first term produces a signal with components at  $E_{LO}^2$ ,  $E_{sig}^2$  and  $2E_{LO}E_{sig}$ , while the second term removes the  $E_{LO}^2$  term from the first term.  $E_{sig}$  is significantly smaller than  $E_{LO}$ , and the term containing  $E_{sig}^2$  can therefore be neglected. The signal is thus approximately  $2E_{LO}E_{sig}$ , which is effectively proportional to  $E_{sig}$ .

### 3.5.9 Lock-In Detection

The AC voltage signal from the balanced detector must be converted to a DC signal before being transferred to a computer, where the magnitude of the DC signal is proportional to the AC signal amplitude. A Stanford Research Systems SR830 dual-phase lock-in amplifier is used to extract the magnitude of the signal, while rejecting noise on all other frequencies than the signal frequency. This is possible even if the signal is extremely small (in the nanovolts range), due to the narrow-band filtering performed by the phase-sensitive detectors (PSDs) of the SR830. The lock-in amplifier remarkably increases SNR, since the bandwidth of the filters is so small (down to 0.01 Hz!). The theory of operation presented in this section is taken from the SR830 manual [37].

Proper understanding of the lock-in detection technique is vital, because all measurement data comes directly from the lock-in amplifier. Furthermore, the relationship between measured data and the optical system is not necessarily straight-forward. Lock-in detection is the source of many practical considerations, some of which are discussed in section 3.6.

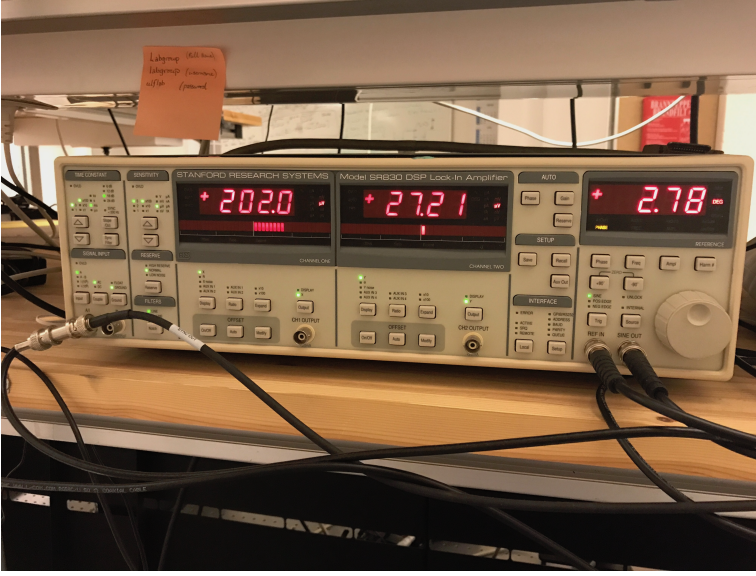


**Figure 3.19:** SR830 lock-in amplifier, showing x and y components of the measured signal (in microvolts).

A functional block diagram of the SR830 lock-in amplifier is shown in figure 3.20. The lock-in has one signal input, one reference input and multiple outputs corresponding to different signal formats. The reference input is used to generate a phase-locked sine-wave, using an internal waveform generator. Two PSDs  $90^\circ$  apart extract the X and Y-components of the signal, using low-pass filters with a bandwidth as low as 0.01 Hz. The data-outputs can be transferred to a computer using GPIB or RS-232.

Consider a voltage signal  $V_s(t)$  generated from the detector with a period given by  $T_s = \frac{2\pi}{\omega_s}$ , where  $\omega_s$  is the fundamental angular frequency of the signal. According to the Fourier theorem, the signal can be expressed as a sum of  $n$  sine waves at frequencies  $\omega_s, 2\omega_s, 3\omega_s, \dots, n\omega_s$ :

$$V_s(t) = V_{s1} \sin(\omega_s t) + V_{s2} \sin(2\omega_s t) + V_{s3} \sin(3\omega_s t) + \dots + V_{sn} \sin(n\omega_s t) + N(t) \quad (3.33)$$

where  $V_{s_n}$  is the amplitude component at the  $n$ th frequency, and  $N(t)$  is a noise signal. Figure 3.22 shows a plot of the signal, with fundamental frequency 1 kHz.

Multiplying  $V_s(t)$  with a sine function at some frequency  $\omega_r$ , with amplitude  $V_r$  and phase  $\theta_r$  yields for each term in the Fourier series

$$V_{s_n} \sin(n\omega_s t) V_r \sin(\omega_r t + \theta_r) = \frac{1}{2} V_{s_n} V_r \cos([n\omega_s - \omega_r] - \theta_r) - \frac{1}{2} V_{s_n} V_r \cos([n\omega_s + \omega_r] + \theta_r) \quad (3.34)$$

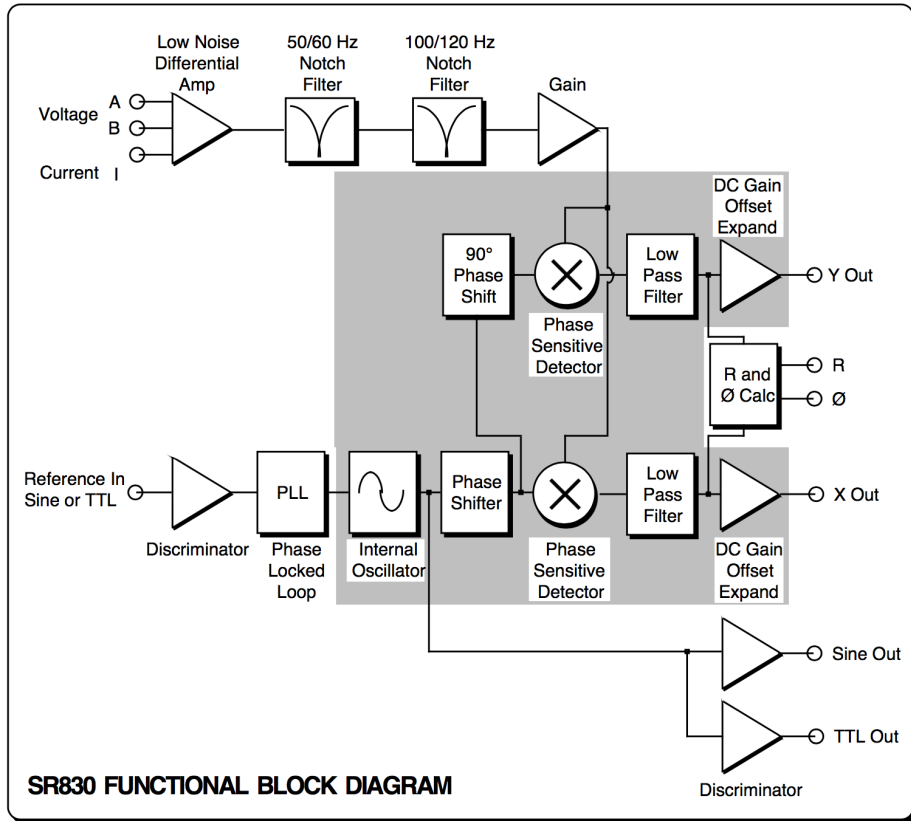


Figure 3.20: Functional block diagram of SR830 dual-phase lock-in amplifier, taken from [37].

i.e., a signal with one component at the sum frequency  $n\omega_s + \omega_r$  and one at the difference frequency  $n\omega_s - \omega_r$ . If the reference frequency is exactly the same as the fundamental frequency of the signal, i.e.  $\omega_r = \omega_s$ , the component in  $V_s(t)$  at frequency  $\omega_s$  gives rise to a DC component due to the difference frequency being 0, while all other components yield AC components at various other frequencies. Passing this signal through a very narrow-band low-pass filter makes it possible to extract only the DC component, corresponding to the signal at frequency  $\omega_s$ , while rejecting the noise outside of the filter bandwidth. Provided that the low-pass filter is sufficiently narrow in bandwidth, the only part of the signal still remaining (not including the remaining noise) is

$$V_{PSD1} = V_{s_1} V_r H(0) \cos \theta_r = V_{sig} \cos \theta_r \quad (3.35)$$

where  $H(0)$  is the transfer function of the low-pass filter at zero frequency. The output voltage is a DC signal proportional to the signal amplitude. This process is handled by the PSDs within the lock-in amplifier.

The lock-in amplifier requires a reference signal which is synchronized to the signal

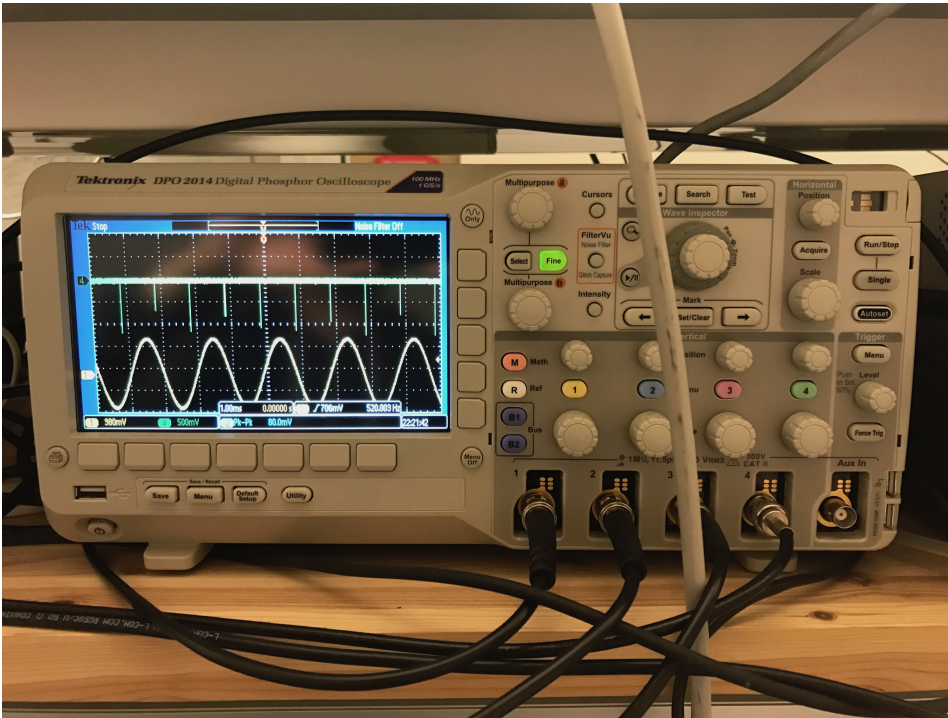


**Figure 3.21:** Tektronix DPO2014 Digital Phosphor Oscilloscope (100 MHz, 4-Ch, 1 GS/s), displaying signal from detector (green) and reference signal from lock-in (yellow).

frequency to correctly filter the signal. Since the chopper wheel (see section 3.5.5) periodically interrupts the laser beam, the fundamental frequency of the detected signal is brought down to the chopping frequency. The reference signal provided by the chopper controller can thus be connected directly to the reference input on the lock-in amplifier.

We consider the case where the chopping frequency is close to (but for practical purposes, not equal to) half of the laser repetition rate, with a duty cycle of 50%, and where the pump is modulated by the chopper. It then follows that the pump is alternately blocked by the shutters and transmitted through the windows of the chopper. The pump alters the propagation of the probe in some way, e.g. by causing refractive index changes in the interaction medium, as explained in section 3.2. Consequently, the probe sees an amplitude modulation with the same frequency as the chopping frequency. This causes the fundamental frequency of the AC signal generated by the detector to change from the laser repetition rate to the chopper frequency, i.e.  $\omega_s = \omega_{chop}$ . Figure 3.23 illustrates how the chopper, running at 520 Hz, modulates the pump induced interaction to change the fundamental frequency of the detector signal.

The phase angle  $\theta_r$  in (3.35) is the phase shift between the reference signal provided by the chopper and the laser modulation induced by the chopper (and not the individual laser pulses, as this phase changes indefinitely with time since the chopper frequency is not an integer multiple of the laser repetition rate). This is dependent on the alignment of the

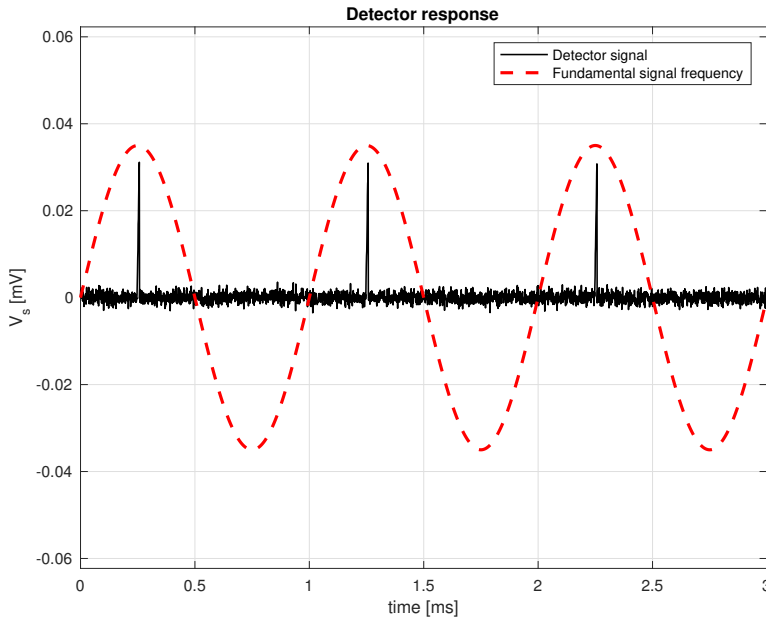


**Figure 3.22:** Simulated detector response with fundamental frequency of 1 kHz. The fundamental frequency is illustrated by the dashed line (amplitude not to scale). The noise is Gaussian distributed.

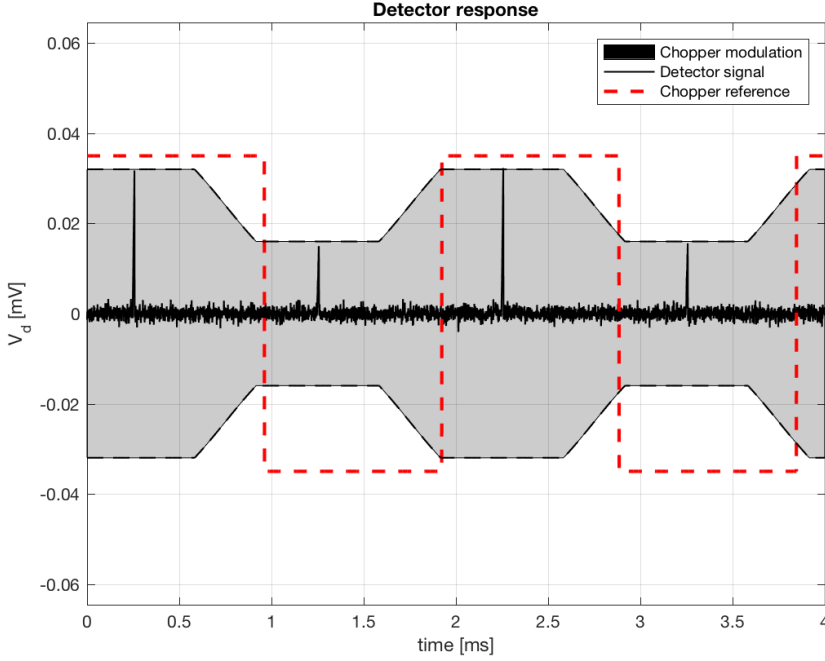
chopper, and does generally not contain any useful information about the measurement. The lock-in amplifier creates a sine wave locked to the chopper reference frequency using a phase-locked loop and an internal waveform generator.

Figure 3.24 shows the result after multiplication of the detected signal and the reference signal with (a) noise only (zero signal amplitude), (b) probe only (no pump modulation) and (c) pump and probe together. The signal in (c) is non-symmetric about the time axis, and the DC signal is lifted out of the noise level. This can be observed directly in figure 3.23, since the pulses that are amplified by the pump always follow a positive flank of the reference signal. In both (a) and (b), the signal is symmetric, and produces no DC signal. In the time-domain, the low-pass filtering process acts as a weighted average, since this is equivalent to a convolution with the filter-response function. The AC-components cancel out if the mean is taken with a sufficiently long time-constant, such that only the DC-component contributes to the signal.

It is desirable to remove the  $\theta_r$ -dependence at the output. This is accomplished by adding an additional phase-sensitive detector with a reference signal  $90^\circ$  out of phase with the reference input. The output of this PSD is

$$V_{PSD2} = V_{sig} \sin \theta_r. \quad (3.36)$$

The extra PSD makes the SR830 a dual-phase lock-in amplifier. The total output signal of the lock-in amplifier can be treated as a vector with  $V_{PSD1}$  as the X-component and  $V_{PSD2}$  as the Y-component;



**Figure 3.23:** Simulated detector response with chopping frequency of 520 Hz. The fundamental period of the detector signal is now nearly twice as long, due to the chopper. The shaded area shows the modulation of the signal induced by the pump (positive and negative halves correspond to clockwise and counter-clockwise depolarization of the probe - see section 3.5.5). Note that the exact shape of the modulation envelope depends on the optics.

$$\begin{aligned} X &= V_{sig} \cos \theta_r \\ Y &= V_{sig} \sin \theta_r. \end{aligned} \quad (3.37)$$

The signal magnitude may be found by computing the length of the vector

$$\begin{aligned} R &= \sqrt{X^2 + Y^2} \\ &= \sqrt{V_{sig}^2 \cos^2 \theta_r + V_{sig}^2 \sin^2 \theta_r} \\ &= |V_{sig}|. \end{aligned} \quad (3.38)$$

A shortcoming of this method is that only the absolute value of the signal magnitude is found. This generally means loss of signal information (such as loss of phase information, if lock-in is used for coherent measurements), and an alternative approach can be used: multiplying  $X$  by  $\cos \theta$  and  $Y$  by  $\sin \theta$  and adding the two together yields

$$S = X \cos \theta + Y \sin \theta = V_{sig} (\cos \theta_r \cos \theta + \sin \theta_r \sin \theta) \quad (3.39)$$

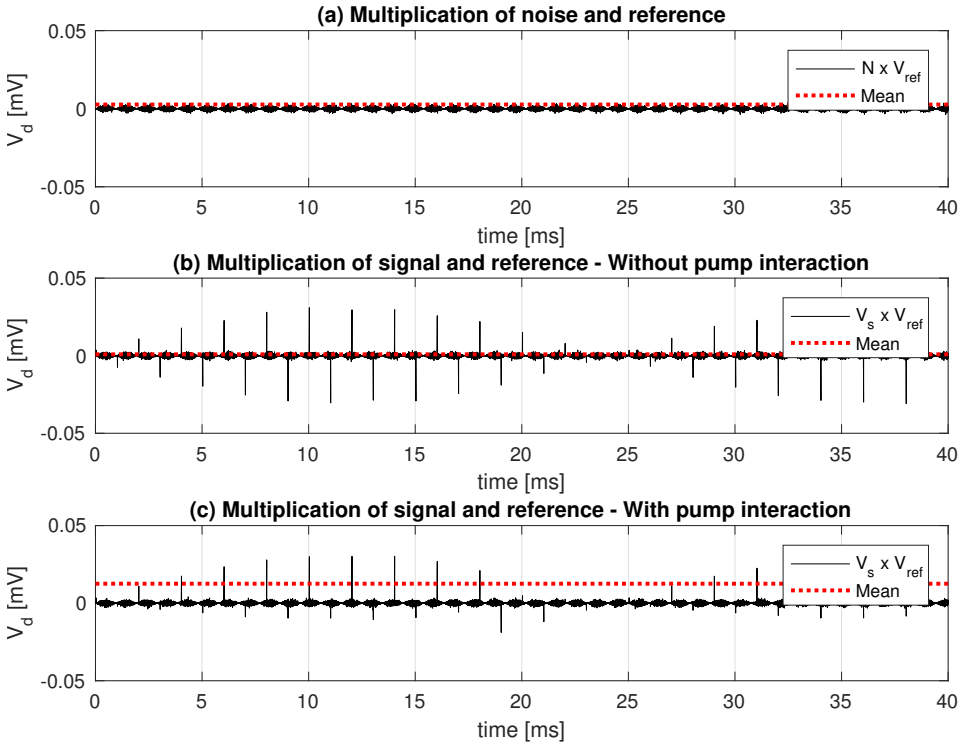


**Figure 3.24:** Result after signal and reference multiplication with (a) noise (b) probe (c) pump and probe. The DC component in (c) can be extracted with a low-pass filter.

where the factor containing the sines and cosines has its maximum when  $\theta = \theta_r$ . Iterating this expression with  $\theta$  varying from 0 to  $2\pi$  to find the maximum value of  $S$  yields

$$\begin{aligned} S_{max} &= V_{sig}(\cos^2 \theta_r + \sin^2 \theta_r) \\ &= V_{sig} \end{aligned} \quad (3.40)$$

and the signal magnitude is obtained.

The SR830 comes with a variety of settings. Two of particular interest are the sensitivity and the time-constant. The sensitivity determines the voltage resolution of the sampling, and the time-constant determines the integration time of the filtering. For a larger time-constant, more pulses are included in each measurement, and the measured signal becomes more stable. If the time-constant is low,  $V_{sig}$  varies over a larger interval, which corresponds to greater uncertainty.

The OKE signal shown in figure 3.6 is a plot of  $V_{sig}$  as a function of the pump probe delay  $\tau$ . For this particular measurement, the time-constant was 300 ms. Each sample point is therefore obtained from an average of 300 pulses. The time-constant can be increased to several seconds, in which case thousands of pulses are included in each sample point. The signal should therefore not be regarded as an instantaneous snapshot of the dynamics, but rather an average of many repeated measurements.

## 3.6 Practical Experimental Considerations

### 3.6.1 Introduction

This section covers some practical aspects of the measurements. The motivation behind this section is to highlight some experimental practicalities that are not so obvious, and document certain phenomena that have taken some time to figure out, with the hope that it may save future students some time and effort.

### 3.6.2 Separation of Signal and Noise

Since the SR830 lock-in amplifier has two phase-sensitive detectors, it is possible to separate the signal and noise into respective channels. It is possible to add an internal phase shift between the signal and reference. The voltage of each channel is then given by

$$X = V_{sig} \cos(\theta_r + \theta_l) \quad (3.41)$$

$$Y = V_{sig} \sin(\theta_r + \theta_l) \quad (3.42)$$

where  $\theta_l$  is the internal lock-in phase angle. If a large signal is transmitted to the detector (e.g. by being slightly away from the balance point),  $V_{sig}$  is large compared to the noise. The phase angle  $\theta_l$  can then be adjusted until one channel is maximized and the other is zeroed. If e.g.  $X$  is maximized, it follows that  $\theta_r + \theta_l = 0$ .  $X$  is then equal to  $V_{sig}$  multiplied by unity and  $Y$  equal to  $V_{sig}$  multiplied by zero. Whatever remains in  $Y$  is therefore noise, and unrelated to the signal. This procedure effectively separates the signal and the noise. The noise floor can be found by lowering  $V_{sig}$  until  $X = Y$ . Typically, the sensitivity of the lock-in has to be increased when  $V_{sig}$  is lowered for the noise to be measurable.

### 3.6.3 The Chopper-Reprate Mismatch

In reading section 3.5.9, it may be natural to wonder why the chopping frequency is set to 520 Hz, instead of 500 Hz, which would be an integer number times the chopping frequency. Mathematically, it would indeed make more sense to set the chopping frequency to an integer number of the laser frequency, as the frequency offset induces a periodic shift in the detected signal, since the laser hits slightly different parts of the chopper wheel on every cycle. This design choice is a matter of practicality. If the chopper wheel is run at exactly 500 Hz, the signal is detected flawlessly for long periods of time, but due to the mechanical jitter in the chopper, it occasionally induces a low-frequency error. This error is dominating on longer scans, and therefore corrupts the signal. By slightly offsetting the frequency of the chopping, the frequency of the error is lowered to something manageable. This scheme therefore introduces a small error in the signal in relatively short intervals, instead of a large error in long intervals, which is a justified trade-off.

The error in the signal originates in the chopper wheel. If we initially assume the chopping frequency to be 500 Hz, pulses from the 1 kHz reprate laser are alternately transmitted and interrupted. If the chopper frequency has a slight drift, then there will be a



periodic interval where two consecutive pulses hit the far-left and far-right portions of a shutter flank, and are therefore transmitted, completely or partially. When the frequency difference between the repate and chopping is low, this effect lingers for a long time. The result is that the detector signal is passed without modulation to the lock-in amplifier, which then produces zero signal.

The mismatch frequency can be calculated by comparing the ideal chopping period  $T'_{chop} = 2$  ms to the actual period  $T_{chop} = T'_{chop} + \Delta T$ , where  $\Delta T$  is the introduced frequency shift. It can then be concluded that every  $n$ th pulse introduces an error, where

$$n \left[ \left\lceil \frac{T_{chop}}{T_{rep}} \right\rceil T_{rep} - T_{chop} \right] = T_{rep} \quad (3.43)$$

which can be rearranged to

$$n^{-1} = \left\lceil \frac{T_{chop}}{T_{rep}} \right\rceil - \frac{T_{chop}}{T_{rep}} \quad (3.44)$$

$$= \left\lceil \frac{f_{rep}}{f_{chop}} \right\rceil - \frac{f_{rep}}{f_{chop}}. \quad (3.45)$$

The brackets  $\lceil x \rceil$  is the ceiling function, which denotes rounding up to nearest integer. If  $\Delta T = 0.05$  s, i.e. a frequency shift of 20 Hz, then  $n = 13$ . That is, every 13th pulse enters the detector with an error.

### 3.6.4 Anti-Reflection Coating

The Kerr angle induced by MOKE is typically very small (on the order of microradians), and optical coating can be applied to the samples to enhance the signal. Figure 3.25 shows the samples used to experimentally test the MOKE system. The samples were made from permalloy ( $\text{Ni}_{0.8}\text{Fe}_{0.2}$ ) grown on fused silica ( $\text{SiO}_2$ ) with a film thickness of about 40 nm. An optical coating of zirconium dioxide ( $\text{ZrO}_2$ ) has been applied to the surface of the samples, to allow multiple reflections to interfere constructively. A rainbow-like pattern can be seen in some of the samples, because the film was grown in a wedge shape. This makes it simpler to find regions in the film with constructive interference, since the sample can be translated parallel to the interface plane by the MOKE sample holder. This type of optical coating is usually referred to as anti-reflection (AR) coating, but in this context the interference is constructive (rather than destructive) for the wavelength of the laser.

### 3.6.5 Kerr Defocusing

The spatial intensity profile of the laser is not uniformly distributed across the spot size, but follows a Gaussian distribution<sup>3</sup>. The intensity is highest in the center of the spot, and decays radially. Since the intensity is inhomogeneous, it follows that the effective refractive index becomes inhomogeneous as well, due to the intensity-dependent refractive index (IDRI) discussed in section 2.4.6. According to (2.84), the second-order refractive

<sup>3</sup>The profile is not perfectly Gaussian, but has an  $M^2$  factor close to unity.

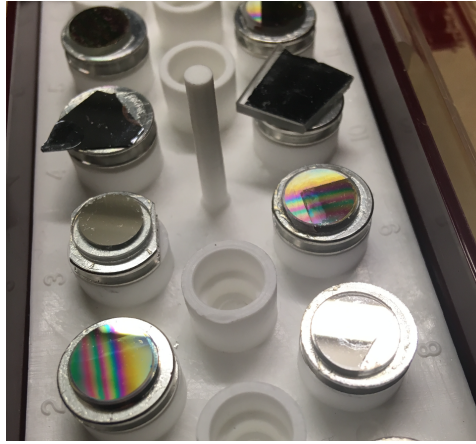


**Figure 3.25:** Samples of permalloy with optical coating

index is proportional to the intensity of the pump. This effectively causes the medium to behave as a lens for the pump, which can be observed as a broadening of the spot size in the transmitted beam. This is known as Kerr focusing or Kerr defocusing [6] and is illustrated in figure 3.26.

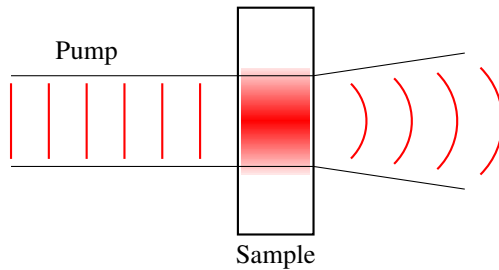


**Figure 3.26:** Illustration of the Kerr defocusing effect. The gradient illustrates the beam intensity profile, which is proportional to the second-order index of refraction.

When the intensity of the pump is too high, the spot size is broadened to the extent that the pump strays into the collimating lens before the detector (see figure 3.12). When this occurs, the probe is overshadowed by the stray light from the pump, and the measurement becomes unreliable. This sets the upper limit the pump intensity<sup>4</sup>. Since IDRI depends on the third-order susceptibility, which is material-specific, the upper limit varies in different materials. Kerr focusing (instead of defocusing) may be observed in some materials. The limiting distance then depends on the effective focal length of the material and the intensity. When the pump power is above the defocusing limit, the OKE signal splits into two peaks due to the high intensity at the main peak.

<sup>4</sup>Note that this is specific to this experimental setup. The limit could have been increased by e.g. increasing the angle of incidence between the pump and the probe. The remaining available space is however limited.



# Results

## 4.1 Bandwidth of the Laser

During the course of the project work, the laser power has been measured frequently. The Solstice system is robust over time, and little drift has been observed. In early stages, the power was measured to be 3.3 W, and was later increased to 3.5 W after maintenance. The bandwidth of the amplified laser is presented in figure 4.1a. The bandwidth was measured with a spectrometer, and the average power was measured with a power meter. The graph in figure 4.1a has been normalized such that the integral of the spectral power is equal to the average power measured with the spectrometer by choosing an appropriate constant  $A$  such that

$$A \int_{-\infty}^{\infty} p(\lambda) d\lambda = \langle P \rangle_{t,\lambda}. \quad (4.1)$$

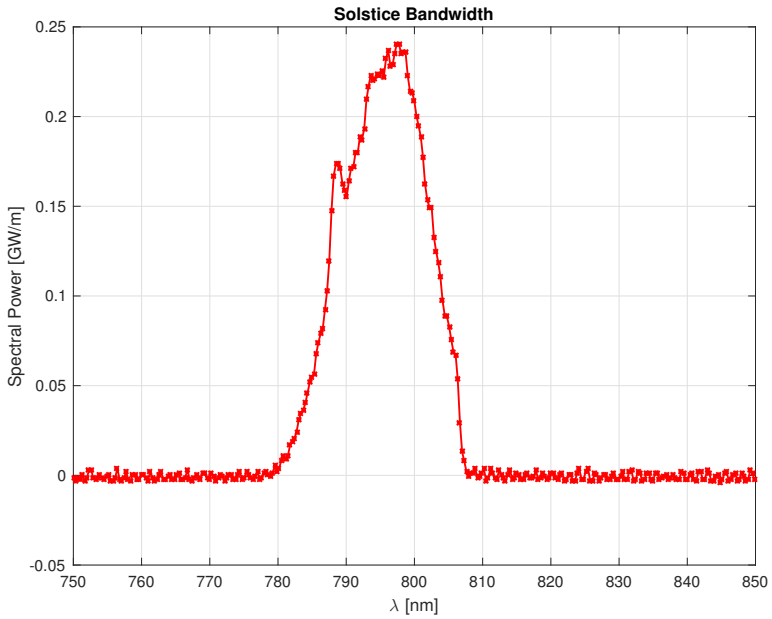
The bandwidth of the Mai Tai seed-laser is presented in figure 4.1b. The graph has been normalized with a similar procedure, using 330 mW for the average power.

The laser light from Solstice is shared between the OKEMOKE system and a second THz system in the Ultrafast Optics Laboratory. The majority of the power (around 90 %) is directed to the THz system, since it requires a great deal of optical power to generate plasma from air.

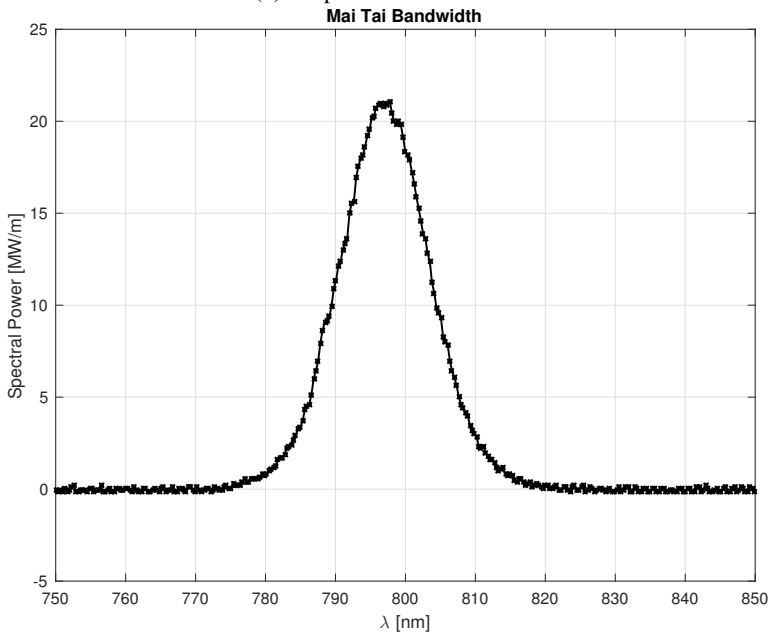
## 4.2 OKE Spectroscopy

### 4.2.1 Overview

In order to extract accurate data from unknown (i.e. not previously characterized) materials, it is necessary to calibrate the measurements with a known reference. Deionized water and acetone has been used to provide reference measurements for the Raman spectrum and the third-order susceptibility tensor elements respectively. Iron-doped zinc sulfide samples have been characterized based on these reference measurements.



(a) Amplified Solstice laser.



(b) Mode-locked Mai Tai laser.

**Figure 4.1:** Bandwidth of the lasers.

This section presents some essential data obtained directly from OKE spectroscopy. Each measurement is presented with a table containing the measurement parameters for the laser, and the lock-in amplifier. The measured laser power is subject to uncertainty on the order of  $\pm 10\%$ . The following post processing steps have been performed on the raw data in MATLAB:

1.  $V_{sig}$  has been extracted from the  $X$  and  $Y$  components of the lock-in amplifier, following the procedure explained in section 3.5.9.
2. The signal has been mirrored left-to-right, because the scanning was done in reverse.
3. The signal has been shifted in time, such that the first sample occurs at  $t = 0$ .
4. The signal has been normalized, by dividing the signal by the peak-value.
5. The signal has been shifted vertically, such that the background noise is centered around 0.

In summary, the following samples have been characterized:

- Deionized water  $H_2O$
- Acetone  $(CH_3)_2CO$
- Iron-doped zinc sulfide  $Fe:ZnS$  thinfilms on Sapphire  $Al_2O_3$  substrate

### 4.2.2 Deionized Water - $H_2O$

OKE spectroscopy on water provides a good calibration of the system, since absorption peaks of water are well-documented in the literature [29]. The primary motivation behind this measurement was to obtain a calibrated instrument function, which could be used to extract Raman spectra of unknown materials.

**Table 4.1:** Experimental parameters for DI water.

Probe power	100 $\mu W$
Pump power	700 $\mu W$
Time-constant	300 ms
Sensitivity	1 mV
Step-length	1 $\mu m$
Number of scans	5

### 4.2.3 Acetone - $(CH_3)_2CO$

Like water, acetone was measured in order to calibrate the system. The third-order susceptibility  $\chi^{(3)}$  of acetone is well-documented, and a procedure exist to calculate  $\chi^{(3)}$  from

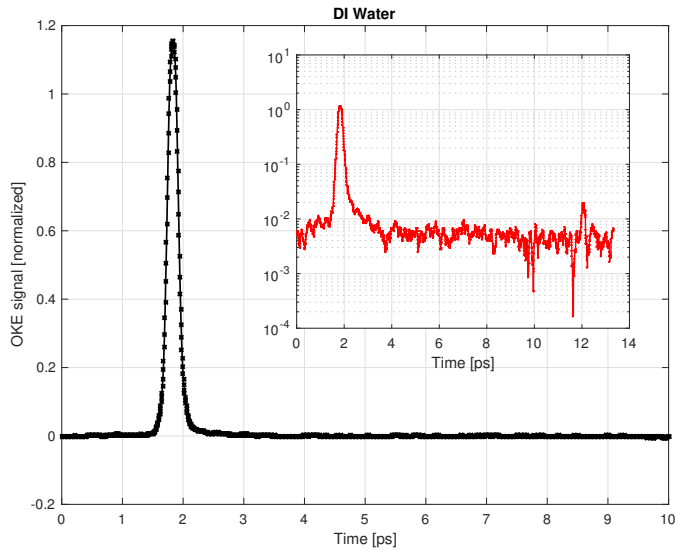


**Figure 4.2:** OKE signal from deionized (DI) water. The inset shows the full signal on a logarithmic scale.

the OKE signal of an unknown sample, based on a known reference. Further details are given in chapter 5.

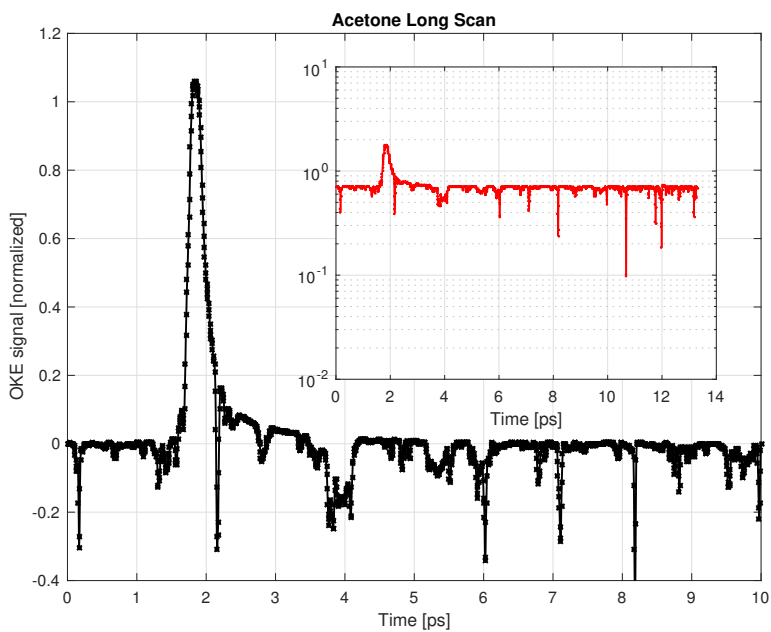
Due to the high vapor pressure, acetone evaporates rather quickly, which made it difficult to run many consecutive scans with high resolution. Two scans were therefore performed: one with long scan range and one with short range, centered around the peak. The  $\chi^{(3)}$  calibration process only utilizes the peak value of the signal, so the short range scan is of greater interest. The long scan is presented in figure 4.3a and the short in figure 4.3b. Both measurements were done with the same experimental parameters.

**Table 4.2:** Experimental parameters for acetone.

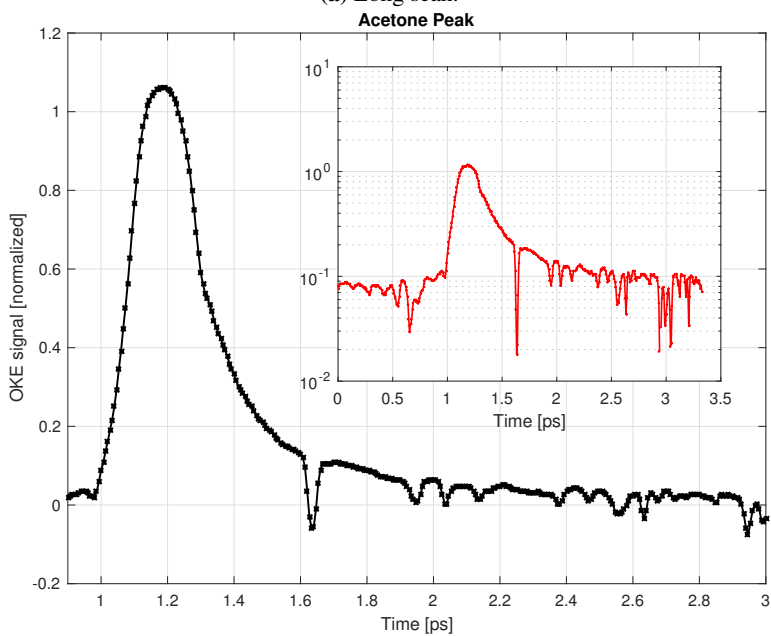
Probe power	100 $\mu$ W
Pump power	700 $\mu$ W
Time-constant	300 ms
Sensitivity	1 mV
Step-length	1 $\mu$ m
Number of scans	5

#### 4.2.4 Iron-Doped Zinc Sulfide on Sapphire Substrate - Fe:ZnS/Al<sub>2</sub>O<sub>3</sub>

On request from another group at the Physics Department, OKE spectroscopy was performed on a series of samples made from sapphire substrate, coated with zinc sulfide and doped with varying amounts of iron. The motivation behind this was to study possible



(a) Long scan.



(b) Scan centered around the peak.

**Figure 4.3:** OKE signal from acetone. The inset shows the full signal on a logarithmic scale..



candidate compositions for Q-switch layers in laser applications. The samples had film-thickness ranging from  $0.5\ \mu\text{m}$  to  $4.5\ \mu\text{m}$ , and iron contents ranging from 2% to 9%. Some were also doped with trace amounts of chromium and cobalt. The measurement was carried out with  $0.5\ \text{mW}$  pump power, to see if results were in agreement with previously measured values obtained with  $10\ \text{mW}$  and  $2\ \text{mW}$ .

Because the pump power was kept low, dynamic range was limited to 100-200 for these measurements, even when averaged over multiple scans. The low dynamic range was caused by both the low angle of rotation from OKE, and also the need to keep the probe power down, because it should be significantly lower than the pump power (preferably by a factor of 5-10), as to not cause self-induced modulation or cross-coupling with the pump. Additionally, the transparency of the samples varied strongly with iron content. Samples with more than 6% iron could not be measured reliably, since too much power had to be added to the probe.

A measurement performed on sample EK086-3 with a film-thickness of  $3.3\ \mu\text{m}$  and iron concentration of 6.0% is shown in figure 4.4. The dynamic range of this measurement was 130.

**Table 4.3:** Experimental parameters for sample EK086-3.

Probe power	$100\ \mu\text{W}$
Pump power	$500\ \mu\text{W}$
Time-constant	100 ms
Sensitivity	$0.5\ \text{mV}$
Step-length	$1\ \mu\text{m}$
Number of scans	5

### 4.2.5 OKE Signal vs Pump Power

The OKE response of DI water has been measured with different values for the pump power, shown in figure 4.5. Theory predicts a linear relationship between the rotation angle and intensity of the pump. Assuming the angles to be small, the signal peak should consequently be linear in the pump intensity as well. The dark noise is expected to remain constant with pump power, since the noise region is measured prior to pump-probe overlap. The measurement does however indicate an overall increase in dark noise with increasing pump power. This is discussed in further detail in chapter 5.

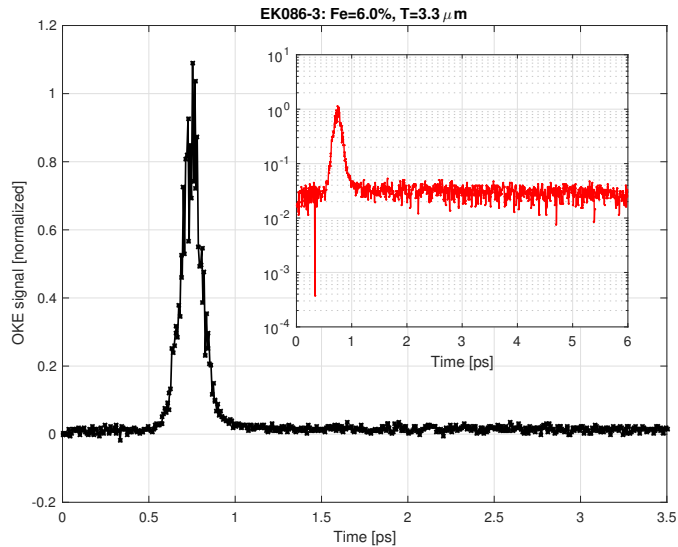


**Figure 4.4:** OKE signal from sample EK086-3. Film-thickness: 3.3  $\mu\text{m}$ , iron concentration: 6.0 %.

## 4.3 MOKE Spectroscopy

### 4.3.1 Overview

MOKE spectroscopy has been performed on thin samples of permalloy  $\text{Ni}_{0.8}\text{Fe}_{0.2}$  with a thickness of about 40 nm, grown on fused silica  $\text{SiO}_2$ , and coated with zirconium dioxide  $\text{ZrO}_2$ . The hysteresis has been measured through magnetic cycling of the ferromagnetic medium. Optical demagnetization and recovery transients have also been measured.

### 4.3.2 Hysteresis of Permalloy - $\text{Ni}_{0.8}\text{Fe}_{0.2}$

The hysteresis of permalloy was measured with MOKE. The main motivation for this measurement was to experimentally verify that the measured signal is attributed solely to the magnetization of the medium. The theory given in section 2.6.3 predicts how the hysteresis of a ferromagnetic sample should behave. Permalloy is an alloy of 80 % nickel and 20 % iron, and is a ferromagnetic material. It was chosen for its prominent magneto-optical response.

The procedure presented in section 3.4 was used to obtain the hysteresis curve, through a single magnetic cycle. The magnetic flux density was increased by moving the magnet closer to the sample with a motorized translation stage, and then decreased by moving the magnet back again. The magnet was then rotated 180°, such that the north pole and south pole switched place, and the procedure was repeated. The magnetic flux density along the x-direction of the magnetic cycle was measured with a Gaussmeter, and the raw data is presented in figure 4.6. The x-axis shows the distance traveled by the magnet in mm, where zero is in reference to saturation of the permalloy sample. The negative portion of the distance-axis indicates that the magnet was moving closer to the sample from far

away, and the positive portion indicates that the magnet was moving back again. This is also illustrated by the arrows, which show the direction of the magnetic cycle. The black and red curves correspond respectively to the north and south pole of the magnet pointing towards the sample. The green line in the center indicates the point where the direction of travel was reversed. Clearly, the flux density is symmetric about the mirror point. Both directions were nevertheless measured.

The instrument used to measure the magnetic flux density has a resolution of 0.1 mT, and the magnet was stepped with a resolution of 25  $\mu\text{m}$ . In the region where the magnetic flux density was measured, the field only changes by around 1 mT, and the curve is therefore ziggurat-shaped.

The MOKE rotation angle  $\theta_k$  is presented in figure 4.7. The measurement was obtained with the magnetic cycling given in figure 4.6. The original units of mV from the lock-in detector have been normalized in reference to the north pole curve.

### 4.3.3 Ultrafast Demagnetization and Recovery of Permalloy

In the final stages of the project work, it was attempted to obtain a time-resolved measurement of MOKE on permalloy. The pump was used to optically demagnetize the medium, and the probe measured the demagnetization phase and recovery transient back to equilibrium. The result is presented in figure 4.8. The figure shows curves for two antiparallel directions of the magnetic flux density, labeled by the north and south pole of the magnet. A phase shift can be observed between the curves, indicating that dynamic process has a contribution from the magnetization. This is further discussed in chapter 5. The scan range is significantly longer than previous OKE results, because the magnetic transient is much slower. The full range of the translation stage was utilized for the scan, and it is believed that the recovery of the magnetization went on for some time after the scan ended. The temporal overlap of pump and probe is thought to occur around  $-130$  ps, but is difficult to locate exactly due to the lack of a sharp transition in the signal.

A measurement without pump is shown in figure 4.9. The first 100 ps have an artifact with repeats over multiple scans, and is believed to be caused by misalignment induced by the translation stage, due to the length of the scan. This region is therefore believed to be unreliable. Comparing figures 4.8 and 4.9, it is apparent that the region before the pump-probe overlap is overshadowed by probe noise.

**Table 4.4:** Experimental parameters for permalloy.

Probe power	500 $\mu\text{W}$
Pump power	2000 $\mu\text{W}$
Time-constant	300 ms
Sensitivity	0.5 mV
Step-length	250 $\mu\text{m}$
Number of scans	5

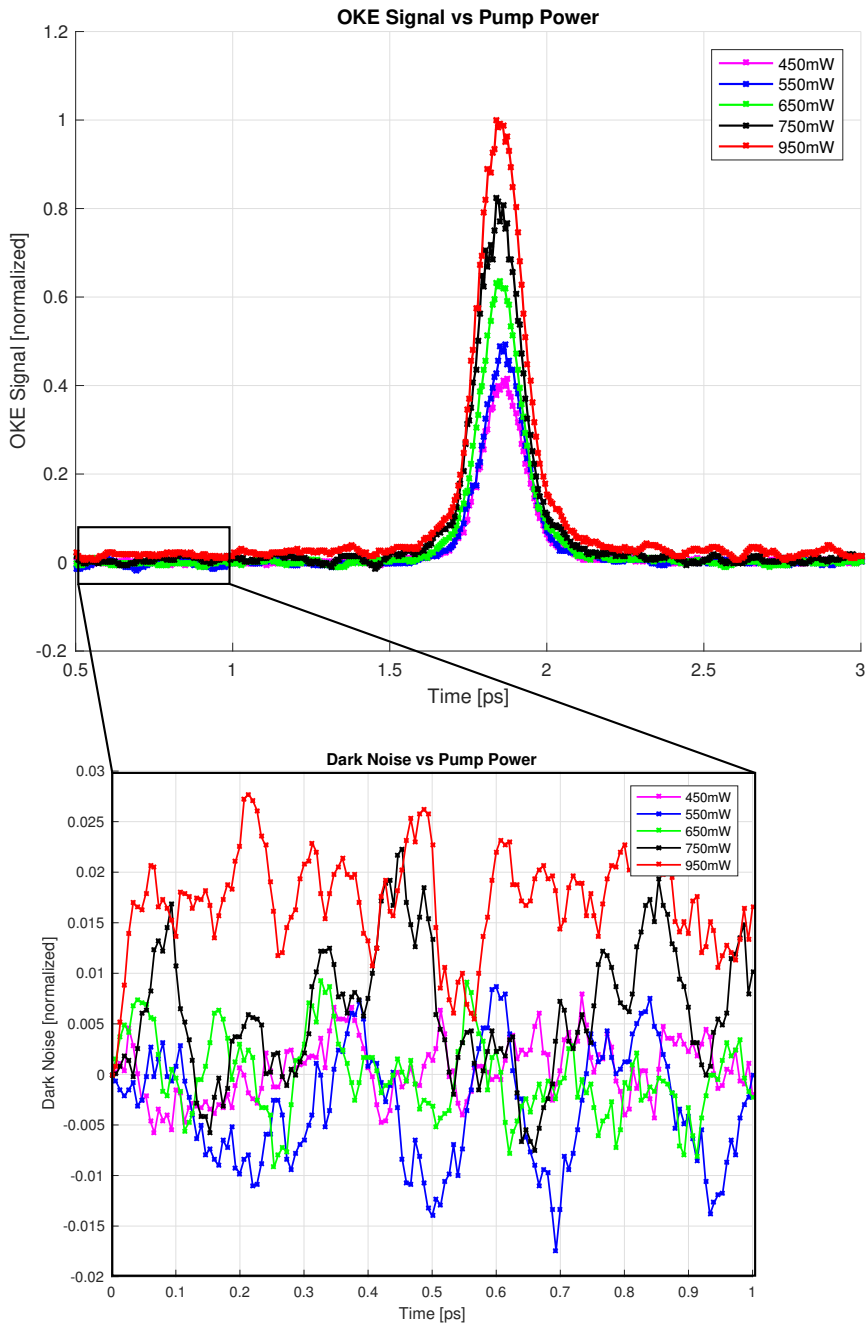


**Figure 4.5:** OKE peak signal and dark noise for different pump powers.

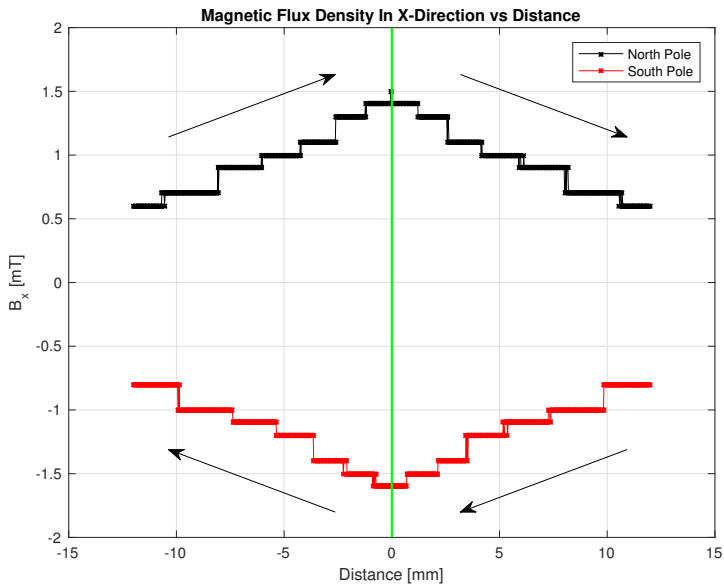


**Figure 4.6:** Raw data of the magnetic flux density along the x-direction of the sample, used to measure hysteresis in MOKE spectroscopy. The arrows indicate the direction of the magnetic cycle. The negative portion of the distance-axis indicate that the magnet was moving towards the sample, and the positive portion indicates that it was moving away from the sample.

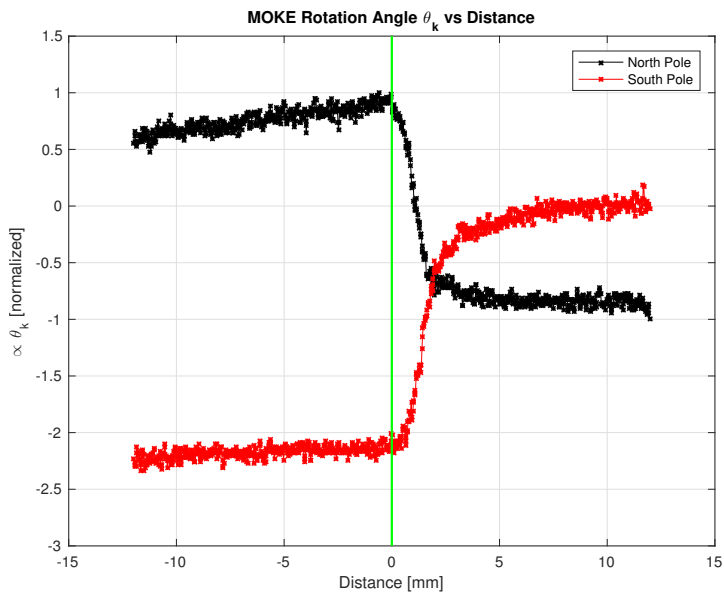


**Figure 4.7:** Raw MOKE signal, obtained with longitudinal MOKE spectroscopy. The asymmetry around the mirror point (illustrated by the green line) indicates a permanent reversal of the magnetization.

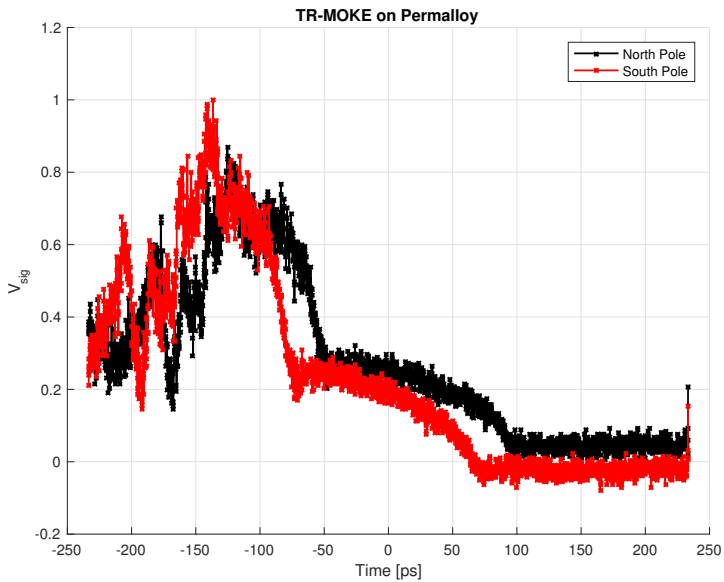


**Figure 4.8:** Raw data from time-resolved MOKE spectroscopy. The full range of the translation stage was used for the measurement.

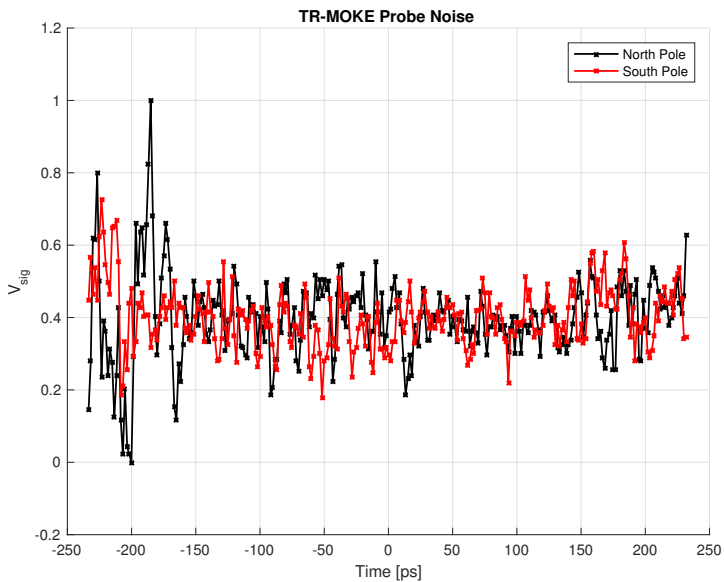


**Figure 4.9:** Time-domain noise measurement on TR-MOKE from probe only. The first 100 ps have noise correlated across multiple scans, and is believed to originate in a slight shift in the probe alignment from the translation stage.



# Analysis

## 5.1 Bandwidth Limit vs Nyquist Limit

The pump-probe measurements presented in chapter 4 were carried out with a step-length of 1  $\mu\text{m}$ , which corresponds to a delay of  $\Delta\tau = 6.7$  fs. The sampling frequency is therefore  $F_s = 1/\Delta\tau = 150$  THz, and Nyquist frequency is  $F_N = F_s/2 = 75$  THz. The Nyquist frequency sets the upper limit for obtainable spectral information, which in this case is 75 THz.

The spectral information obtained from time-resolved measurement can at the same time not exceed the bandwidth of the laser, because there are no available photons there. Since the laser is pulsed with ultrashort temporal width, the bandwidth is relatively large. Instead of a single virtual state available for Raman resonance, as illustrated in figure 2.14, a band of states are created, which greatly increases the probability of Raman resonance occurring. This is illustrated in figure 5.1. Since the stimulated Raman effect originates in the mixing of photons at the laser and Stokes frequency, both frequencies must necessarily have a large enough population in the laser bandwidth to excite an appreciable number of states. The highest mode that can be excited from the ground state must therefore be lower than the bandwidth, i.e.  $\Omega < \Delta\nu$ .

The optical bandwidth of the laser is given by [38]

$$\Delta\nu = \frac{c_0}{\lambda_c^2} \Delta\lambda \tag{5.1}$$

where  $c_0$  is the speed of light,  $\lambda_c$  is the central wavelength and  $\Delta\lambda$  is the linewidth. Several possible definitions exist for the linewidth, and the full-width at half maximum (FWHM) is commonly used. However, since this is a nonlinear effect, the FWHM is not necessarily the best metric. Since the profile of the linewidth of the Solstice is sharply defined, we will take the linewidth to be 30 nm (see figure 4.1). The central wavelength is 800 nm, and the bandwidth is therefore 14.1 THz.

The optical bandwidth is significantly smaller than the Nyquist frequency, i.e.  $\Delta\nu < F_N$ , and the measurement is therefore bandwidth-limited. Spectral data obtained from



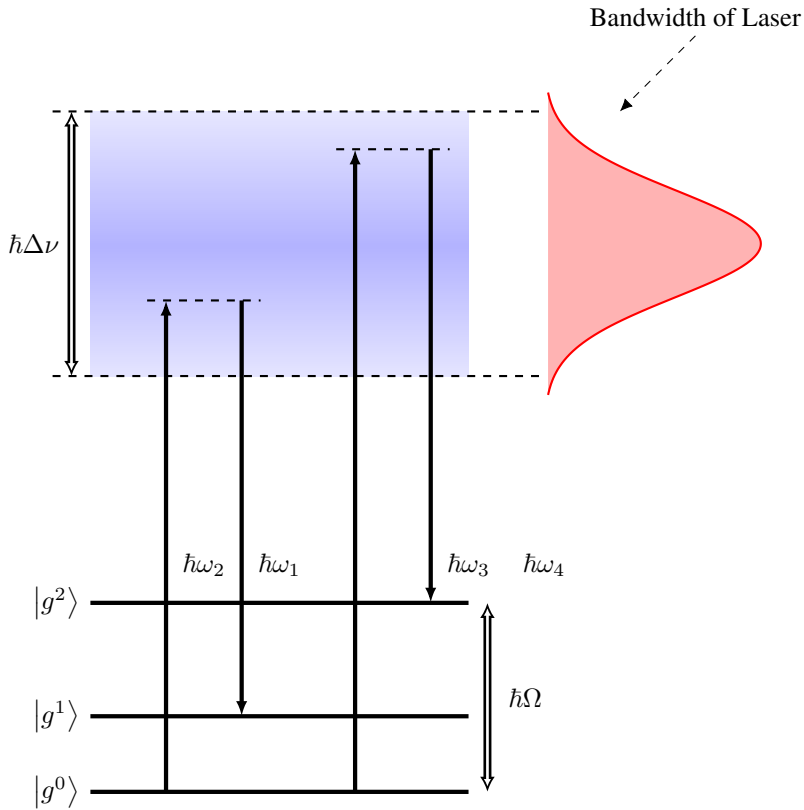


**Figure 5.1:** Broadband Raman resonance, with two modes excited. Frequencies  $\omega_1$ ,  $\omega_2$ ,  $\omega_3$  and  $\omega_4$  must be contained within the bandwidth in order to excite the two modes. The highest frequency that can be excited must fulfill the criteria  $\Omega < \Delta\nu$ .

time-resolved spectroscopy above 14 THz can not be trusted to contain physically valid information and have been discarded in the analysis.

## 5.2 Analysis of OKE Data

### 5.2.1 Overview

In this section, results from OKE measurements are analyzed. The instrument function is addressed in detail in section 5.2.2. The analysis is based on the derivations given in section 3.3.3, and the results presented in section 4.2.

## 5.2.2 The Instrument Function

The OKE signal can be separated into two different time-scales: the instantaneous electronic response and the non-instantaneous nuclear response. The electronic response in the time-domain is termed the instrument function  $G_0^{(2)}$ . As discussed in section 3.3.3, the spectrum of the OKE signal should be divided by the spectrum of the instrument function in order to isolate the nuclear response and obtain the Raman spectrum. Choosing a suitable instrument function is therefore paramount. Possible methods of obtaining an instrument function include curve-fitting, measuring the auto-correlation of the laser source and measuring the OKE response through a reference medium (such as the cuvette for liquid samples). The main issue with the latter two methods is accurately overlapping the measured instrument function with the measured OKE signal. As it turns out, the calculation of the Raman spectrum is extremely sensitive to the alignment of the two functions. A type of curve-fitting has therefore been performed, where the instrument function has been constructed from measurements of an OKE signal, instead of through a separate measurement. This has produced reliable results which, to a satisfying degree, conforms with results obtained by others [29].

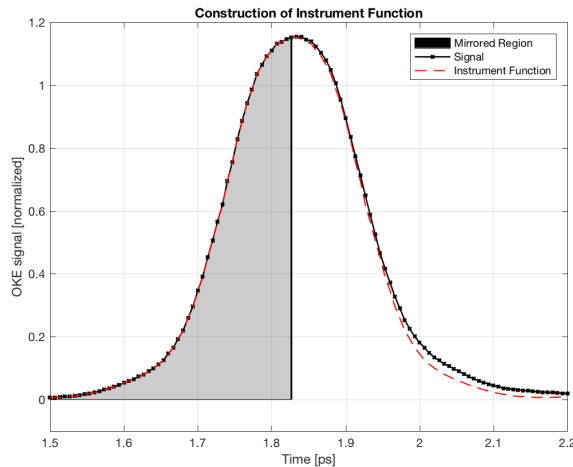


**Figure 5.2:** Construction of instrument function (dashed curve) from measured signal on DI water (black curve). The shaded region was mirrored around a point close to the peak. The black line indicates the mirror point.

The instrument function was created from the measurement on DI water presented in figure 4.2. It was constructed by cropping the signal from before the peak and up until somewhere near the peak. This segment was then mirrored around the upper limit, and the remaining portions were zero-padded. Since the electronic response is instantaneous on the time-scale of the laser, it stands to reason that it is the dominating contribution in this very early region of the signal. This signal should also be symmetric around the peak, because it is mathematically given by the autocorrelation of two Gaussians. The idea behind this procedure was to reflect both the rapid response-time and symmetry of the instrument

function. The procedure is illustrated in figure 5.2, and again on a logarithmic scale in figure 5.3. The constructed instrument function was used to calculate the Raman spectrum of water, and the calculated results were compared to results from the literature. Initially, the maximum point of the peak was chosen as the mirror point, but this did not produce the desired result. The instrument function was therefore adjusted one sample to the left or right in an iterative process, until the results were in agreement with the literature. As it turns out, even very subtle changes to the instrument function has a great impact on the resulting spectrum, and iterative adjustments were therefore required. Several attempts were made to curve-fit the instrument function to a Gaussian curve, since the laser has a temporal profile close to that of a Gaussian. This was done in hopes of creating a cleaner tail-off of the instrument function, but did not end up producing the correct results. The idea was therefore eventually abandoned.

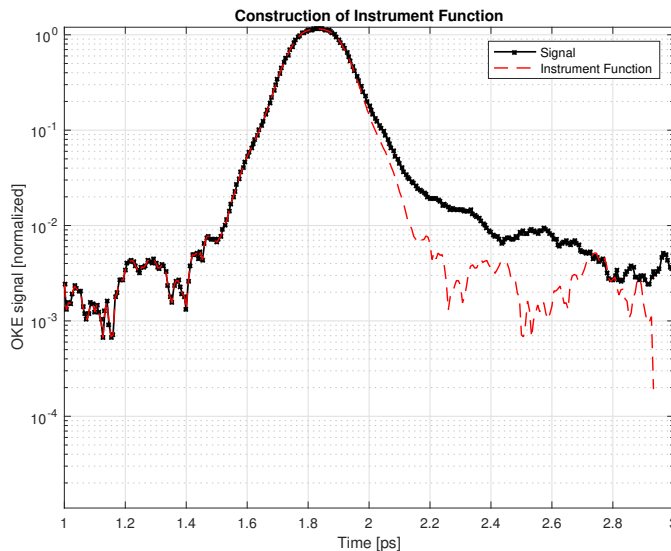


**Figure 5.3:** Logarithmic plot of signal and instrument function.

Both signals were Fourier transformed with the fast Fourier transform algorithm. According to the shift theorem of the Fourier transform, a shift in the time-domain from  $t$  to  $t - a$  corresponds to multiplication by a factor  $e^{-i2\pi f a}$  in the transformed signal, i.e.

$$\mathcal{F}\{g(t - a)\} = e^{-i2\pi f a} G(f). \quad (5.2)$$

In order to avoid ringing in the spectra from the shifting, both signals were cropped such that the first sample was located at the peak. The cropped signals are presented in figure 5.4. The imaginary part of the spectra are shown in figure 5.5. A slight frequency shift was introduced to achieve better overlap in the frequency-domain. The shifting was another parameter that was iteratively adjusted in the process.

The resulting Raman spectrum for water is presented in figure 5.6. Some smoothing has been performed on the experimental data to reduce ripple. Water is reported to have

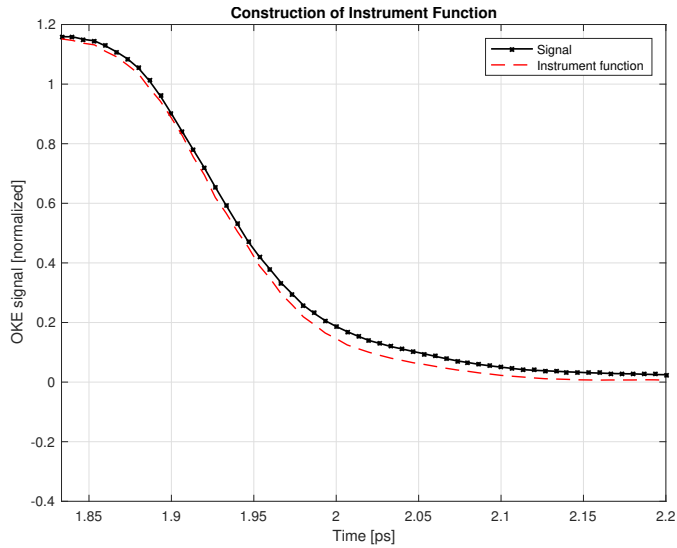


**Figure 5.4:** Signal and instrument function after cropping. Only the initial part of the signal is shown - the full signals extend out to 11 ps.

transition peaks at wavenumbers  $45 \text{ cm}^{-1}$ ,  $175 \text{ cm}^{-1}$  and  $400 \text{ cm}^{-1}$  [29], which corresponds to frequencies of 1.35 THz, 5.25 THz and 12.0 THz. These values were used in a curve-fit in order to test the quality of the instrument function. The curve-fitted signals are shown as dashed lines in figure 5.6. The curve-fitting was based on the assumption that the 12 THz mode is resolvable with a bandwidth of 14 THz. It is however possible that the optical power is insufficient to excite a measurable response at this frequency, in which case the instrument function is less valid.

As pointed out in section 3.3.3, the transitions are often not purely Gaussian, but behave according to more complicated functions. A better fit can be achieved for the lower frequency mode by replacing one Gaussian with the Bucaro-Litovitz (BL) function

$$I_{BL} = A_{BL} \omega^\alpha e^{-\omega/\omega_{BL}}. \quad (5.3)$$

The higher-order modes can similarly be improved by introducing a slight asymmetry in the Gaussian profile (e.g. by asymmetrized Gaussian (AG) functions). This does however require some insight into the specific mechanism of the medium, in order to make physical sense. Another issue that arises when the lower frequency mode is asymmetrized is that the 5.25 THz mode is suppressed in the curve-fit process. In order to preserve this mode, restrictions must be asserted in the curve-fitting process. This requires more detailed modeling of the molecular behavior, and is outside of the scope of this thesis. The curve-fitting has instead been done with three Gaussians, at the expense of preciseness.

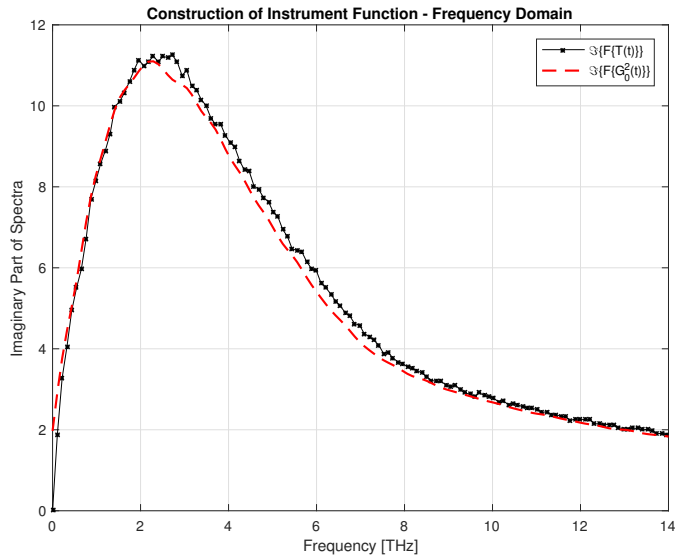


**Figure 5.5:** Imaginary part of spectra. A slight frequency shift has been introduced to improve the overlap of the signals in the frequency-domain.

**Table 5.1:** Third-order susceptibilities for iron-doped zinc sulfide samples. Values are given in esu units. Previous data for sample EK040-3 was not available.

Sample	Description		$\chi^{(3)}$ [esu, $10^{-13}$ ]	
			Pump Power	
	Doping	Thickness	2 mW	0.5 mW
EK088-4	Fe=2-3 %	4.5 $\mu\text{m}$	117.2	127.6
EK086-3	Fe=6.0 %	3.3 $\mu\text{m}$	215.1	166.7
EK086-4	Fe=6.0 %	3.2 $\mu\text{m}$	214.8	273.5
EK040-3	Fe=9.0 %	3.5 $\mu\text{m}$	-	503.4

### 5.2.3 The Third-Order Susceptibility

The third-order susceptibility of several samples iron-doped zinc sulfide was measured, using acetone as a reference sample. The values were calculated using the procedure presented in section 3.3.4. The linear refractive index, absorption and thickness of the samples were provided by another group who did prior measurements on the same samples. The calculated values were compared to previously measured values with less pump power, and it was found that previous measurements were satisfactory. Results are presented in table 5.1. Samples with too high absorption or too much surface roughness were found unreliable for measurement, and have been excluded here.

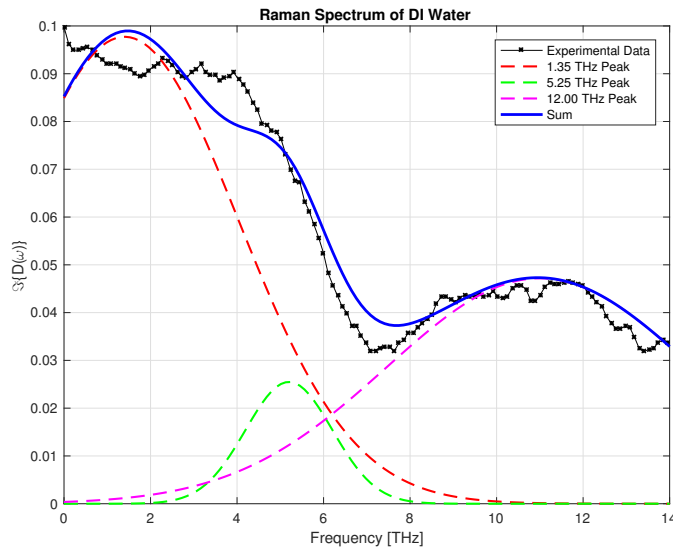


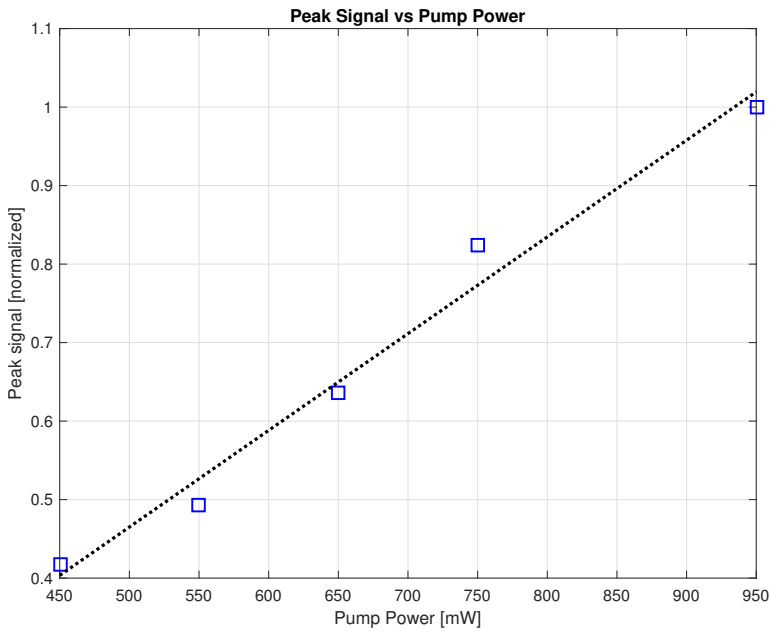
**Figure 5.6:** Raman spectrum of DI water. Experimental data has been fitted to a sum of three Gaussians centered around theoretical transition frequencies.

## 5.2.4 Dark Noise and Dynamic Range

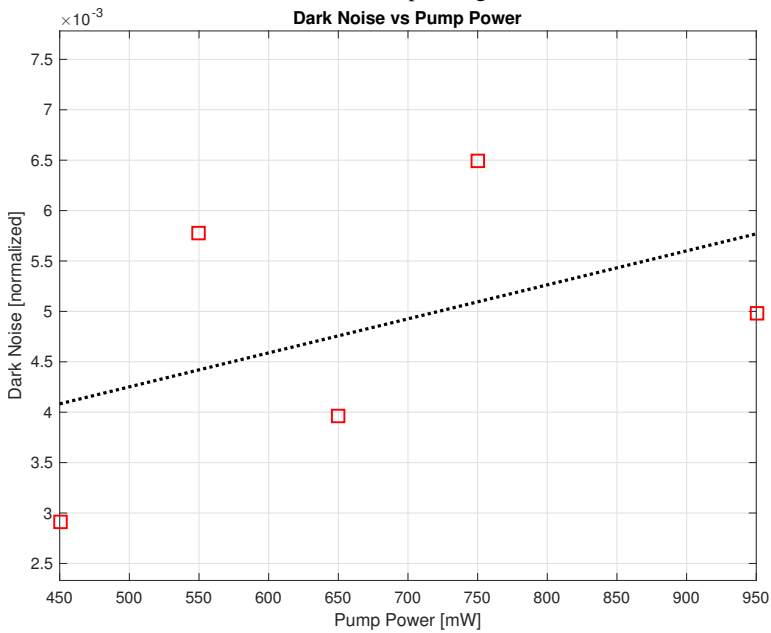
The dark noise was shown in figure 4.5, measured on DI water. According to theory, the rotation angle is proportional to the the pump intensity (and thus the power). Assuming the angle is small, the signal is approximately proportional to the angle, and the peak signal should therefore be proportional to the intensity. The dependency is shown in figure 5.7a, and conforms well with theory. Note that the power on the horizontal axis is the average power, not the peak power.

The dark noise was defined in chapter 3 as the ratio of the peak signal to the standard deviation of the dark noise. The term *dark noise* is analogous to its counterpart in spectrometers, and is the signal measured when no light enters the detector. In pump-probe spectroscopy, the dark noise is defined as the signal in the region before there is temporal overlap between pump and probe. It is therefore not truly *dark* in the same sense as with spectrometers, but the same principle applies. Since the dark noise is measured before the probe is depolarized by the pump, it should ideally be independent of the pump power. This is however not the case, as can be seen in figure 5.7b. There is an overall increase in noise as the pump power is increased. This is unlikely to be an effect of the depolarization, but rather from stray light following the probe signal to the detector. As mentioned in section 3.6.5, scattering of the pump increases with pump intensity. Even though the pump is delayed significantly in relation to the probe on the time-scale of the laser, the deciding factor is the integration time of the detector, which is on the order of  $\mu\text{s}$ . The increase in noise is therefore presumably caused by the scattering of the pump, and the long integration time of the detector.

The dynamic range is plotted against pump power in figure 5.8. Both signal peak and noise were normalized with the same reference, so the numerical value of the dynamic



(a) Normalized peak signal.



(b) Standard deviation of the dark noise.

**Figure 5.7:** Dependence of signal peak and dark noise on pump power, measured with OKE spectroscopy on DI water.

range is the same as for raw data (i.e. calculated with units of mV). The dynamic range of this measurement series ranges from around 80 to 200, which is rather low. The dynamic range can however be increased significantly by repeated scans, since the noise averages out while the signal is lifted up. The other results presented in section 4.2 have been measured with repeated scans, and have DR ranging from 400 to 1000 (except for the measurements on zinc sulfide films which were closer to 100-200). Since DR is directly proportional to the peak signal, it is not only a metric of the signal quality, but also the signal itself. Two hypothetical samples with the same transparency but different third-order nonlinear response functions would create the same amount of dark noise in the detector, but have different DR. The standard deviation of the noise can also be artificially lowered by reducing the sensitivity of the lock-in amplifier, such that the noise distribution falls below the discretization intervals. In that case, the DR can be made arbitrarily high, although clearly at the expense of signal quality and resolution.

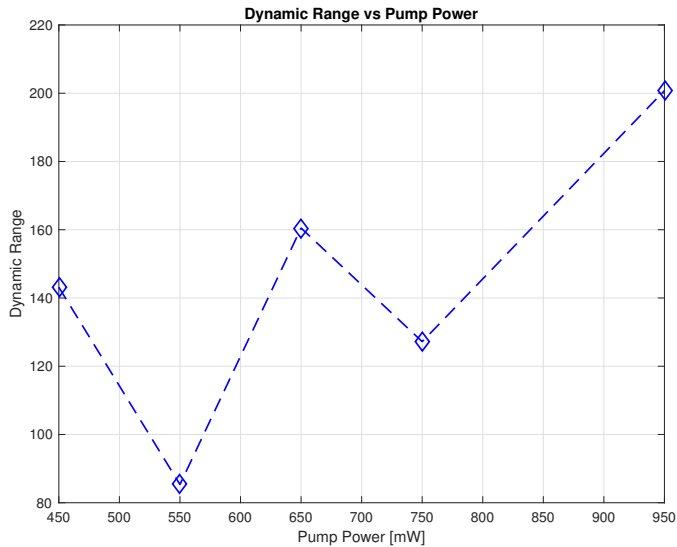


**Figure 5.8:** Dynamic range plotted against pump power of single-scan measurements.

## 5.3 Analysis of MOKE Data

### 5.3.1 Overview

In this section, the MOKE data presented in section 4.3 is analyzed. The hysteresis of permalloy has been plotted, based on direct measurements of the rotational angle of the probe, and calibration curved for the magnetic flux density. The measurement was carried out to evaluate the possibility of using magneto-optical Kerr effect for detection of magnetization. Optical demagnetization of permalloy has also been performed, and the recovery transient has been measured.



### 5.3.2 Hysteresis

The magnetic cycling used to measure the hysteresis was shown in figure 4.6. The Gaussmeter had a resolution of 0.1 mT, and the magnet was stepped with a resolution of 25  $\mu\text{m}$ . As a result, the calibration curve for the magnetization was ziggurat-shaped, which severely limits the resolution of the hysteresis curve. In order to overcome the low resolution, the magnetic field has been curve fitted to an exponential decay, which has been observed when the magnet has been stepped closer to the sensor (where the magnetic flux density, and thereby the spatial resolution is higher). The fitted data is shown in figure 5.9.

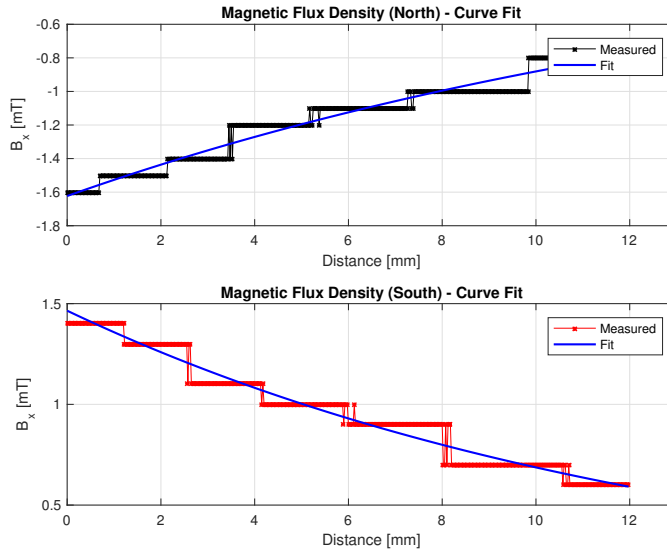


**Figure 5.9:** Magnetic flux density of the north pole and south pole of the magnet, measurement and fit.

Since the magnetic field is supplied by a permanent magnet, the range of available flux density is limited entirely by the strength of the permanent magnet and the range of the motor used to step the magnet. The range was chosen to include the coercive field  $B_c$ , and to be high enough to achieve saturation. This range was chosen, because it provides the required data points to calculate the coercivity of the sample. This came at the expense of not being able to completely zero the magnetic field. As shown in figure 4.6, the magnetic field never reaches zero, because the translation stage is out of range. The sensitivity of the Gaussmeter was also a limiting factor. Because of this, only the fringes of the hysteresis were measured.

The result is presented in figure 5.11, and the coercive field was measured to be  $1.43 \text{ mT} \pm 0.2 \text{ mT}$ . The uncertainty stems primarily from the resolution and offset of the calibration curve, but some uncertainty is also introduced in the curve fitting. This measurement proves beyond doubt that the signal originates in magneto-optical effects. It is however unclear whether the signal could be attributed to the longitudinal MOKE alone, or if polar/transverse effects were a contributing factor. Magneto-optical anisotropy is an additional source of uncertainty, however the signal was not found to change significantly

when the sample was rotated. The primary source of uncertainty is the magnet, which restricts the control on the field. The hysteresis also appears to have an unexpected tilt, which is likely to be caused by imperfections in the alignment of the magnetic field.

### 5.3.3 Time-Resolved MOKE

A phase-shift of about 100 ps can be observed between the two signals presented in figure 4.8. The exact origin of the phase-shift is unknown, but it is believed to originate in magnetic pinning of the magnetization from the underlying  $\text{SiO}_2$  layer on which the  $\text{Ni}_{0.8}\text{Fe}_{0.2}$  film was grown. The magnetic contribution in the signal was extracted, using the procedure given in section 3.4.3. The signal difference obtained with the two antiparallel alignments of the magnetization is presented in figure 5.10. The plot shows a distinct ringing, which is believed to originate in magnetic precession induced by the demagnetization of the pump, as observed by others [39]. This transient was however not studied in detail due to time-limitations in the project, and is left as a suggestion to further development.

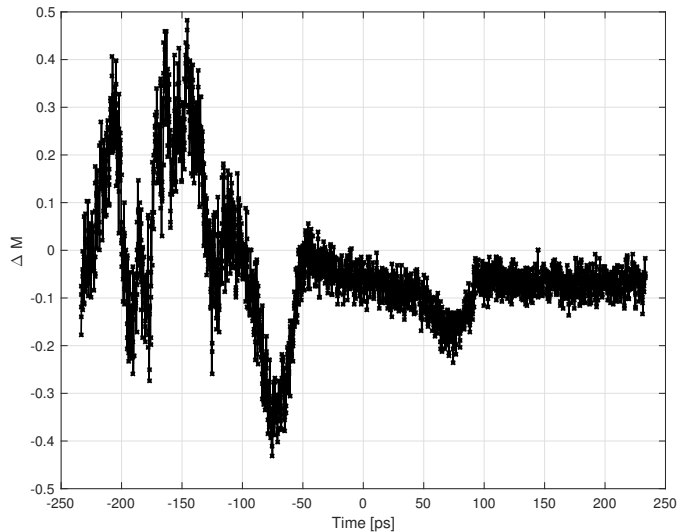
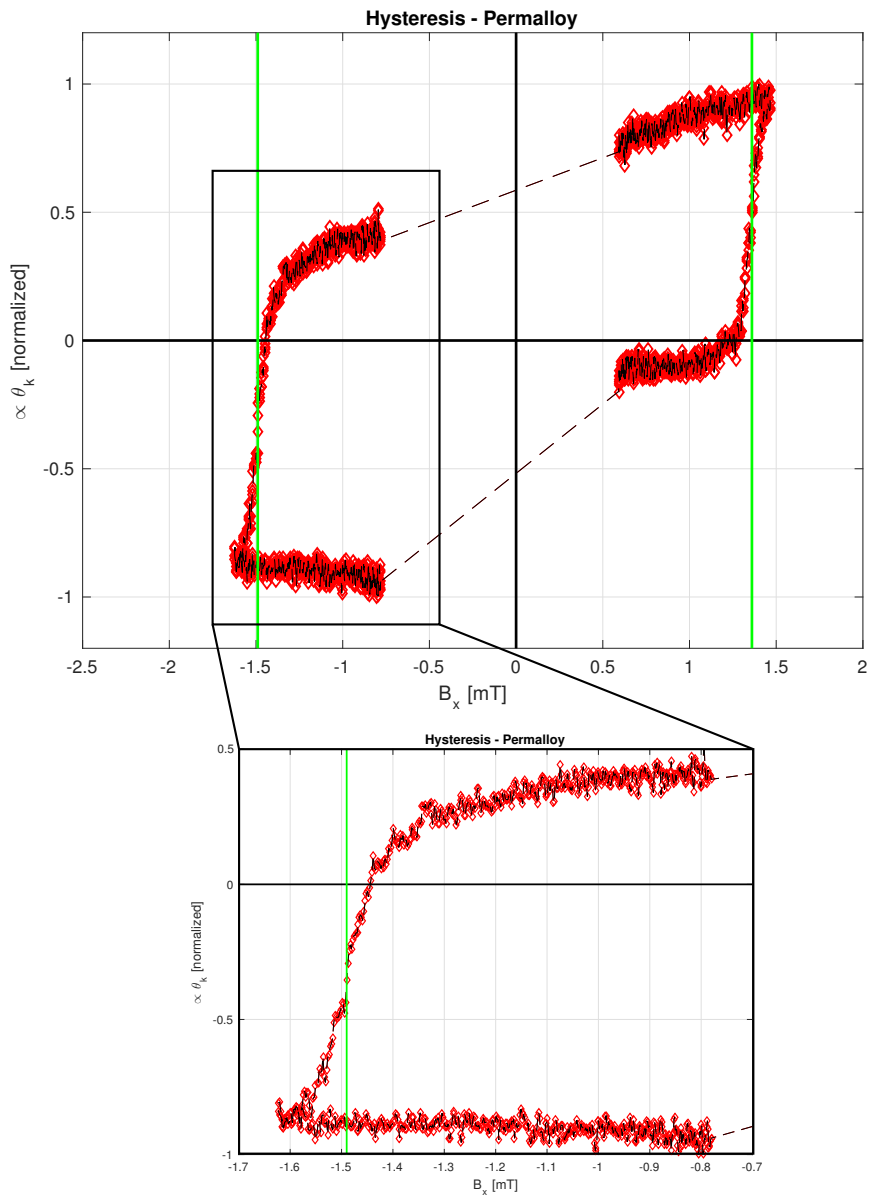


Figure 5.10: TR-MOKE signal of permalloy.



**Figure 5.11:** Hysteresis measurement of permalloy. The hysteresis was measured to be  $1.43 \text{ mT} \pm 0.2 \text{ mT}$ , indicated by the green lines. Only fringes have been measured due to restrictions in available magnetic flux density.

# Conclusion

## 6.1 Concluding Remarks

The purpose of this masters project was to create an optical measurement system to experimentally verify the feasibility of using nonlinear and magneto-optical spectroscopy to measure dynamic processes in condensed matter. The system was built as an expansion to an existing system, capable of performing OKE spectroscopy. A series of improvements were done to the system, including improvements of the lock-in technique with optical choppers to better extract the signal from the noise, and detailed analysis of the OKE data. OKE spectroscopy was tested by performing measurements on deionized water and acetone. The third-order susceptibility of iron-doped zinc sulfide films on fused silica substrate was calculated from measurements on the films and reference measurements on acetone. A Raman spectrum of deionized water was also obtained, by constructing an instrument function from the measured data. The purpose of the instrument function was to isolate the electronic response from the nuclear. The bandwidth of the laser was measured to be 14 THz, and it was speculated that vibrational modes as high as 12 THz could be resolved from measurements on water.

The optical system was also expanded to include magneto-optical measurements. The longitudinal magneto-optical Kerr effect was studied on thinfilms of permalloy grown on fused silica. Permalloy is a ferromagnetic medium which was chosen for its prominent magneto-optical response. A hysteresis measurement was obtained through continuous monitoring of the MOKE response as the magnetization of the medium was cycled. The measured signal was asymmetric in the magnetization, and dependent on the history of the magnetization. The hysteresis measurement proves that MOKE is indeed a feasible approach to non-invasive, ultrafast measurements of the magnetization, attainable with the laser system available in the Ultrafast Optics Laboratory. An attempt was made to optically demagnetize permalloy with a pump beam, and monitor the demagnetization phase and recovery transient. The time-resolved signal was shown to have a magnetization-dependent phase-shift. The origin of the phase-shift and magnetization transient was not explored in detail, but is believed to originate in magnetic pinning between the film and substrate. The

time-resolved MOKE measurement was thus inconclusive.

## 6.2 Further Work

This masters project represents a significant first step towards the goal of creating an ultrafast measurement system capable of resolving dynamical processes related to magnetic properties of perovskite oxides. There is however much to be done before this goal is fully realized. One of the most limiting factors encountered in MOKE measurements was the lack control over the magnetization process. The magnetic flux density was supplied by a permanent magnet, which granted poor control of both direction and magnitude of the field. In future work, an electromagnet should replace the permanent magnet, and more sensitive instruments should be used to measure the magnetic flux density. An electromagnet would grant the ability to perform fast and accurate measurements of the hysteresis, which would enable a much more detailed and efficient analysis of the magnetic behavior during time-resolved scans of demagnetization and recovery. The current solution was also limited by not being able to completely nullify the external magnetic field. This made coercivity measurements less accurate, due to potential errors in the calibration, which are otherwise undetectable. Incorporating an electromagnet seems to the author to be the natural next step in the development process.

There are many ways to improve the resolution and magnitude of the MOKE signal. Anti-reflection coatings and more sophisticated arrangements of the chopper wheels were mentioned in chapter 3 as ways to improve the signal. These solutions were only partially explored in this project, and could very well be taken up by someone else in the future. Throughout the course of the project, many attempts were made to perform MOKE spectroscopy on lanthanum strontium manganite, which is the primary motivation for the project. No signal could however be measured that was correlated with the magnetization, and it is speculated that this was simply due to the low magnitude of the signal. Further improvements in the signal-to-noise ratio and detection scheme is therefore believed to be necessary before the ultimate goal can be reached.

The MOKE sample holder was constructed with the ability to fully rotate samples, while keeping the magnetic field static. The idea behind this design choice was to enable measurements of magneto-optical anisotropy, and possibly other types of anisotropy as well. Measurements on anisotropy reveals information about symmetry, and is an additional area of interest when it comes to magnetic perovskites. This does however require that the previously mentioned improvements to the system are in place, and is therefore something to consider a bit further into the future.

The experimental part of OKE spectroscopy has been very successful, and data obtained in the time-domain conforms well with measurements performed by others. The frequency-domain analysis was however somewhat lacking, due to the high sensitivity of the calculation process. The Raman spectrum obtained in the analysis was based on time-resolved measurements on deionized water. Water is actually a very difficult medium to work with, due to the rapid decay in the relaxation process. It was chosen for its high availability and extensive documentation. Liquids such as carbon disulfide ( $\text{CS}_2$ ) and chloroform ( $\text{CHCl}_3$ ) have significantly slower relaxation, and are much more suitable for this type of characterization. The initial plan for the project was to use said liquids to test the

capabilities of the system. This was however abandoned due the difficulty in getting the right permission, since both carbon disulfide and chloroform represent a significant health hazard to humans, even without exposure to laser light.



# Bibliography

- [1] Neil H. E. Weste and David Money. Harris. *Integrated circuit design*. Pearson, 2011.
- [2] H. Esmailzadeh, E. Blem, R. St. Amant, K. Sankaralingam, and D. Burger. Dark silicon and the end of multicore scaling. *IEEE Micro*, 32(3):122134, 2012.
- [3] Bernd Hoefflinger. Itrs 2028 - international roadmap of semiconductors. *The Frontiers Collection CHIPS 2020 VOL. 2*, page 143148, 2015.
- [4] William W. Parson. *Modern Optical Spectroscopy With Exercises and Examples from Biophysics and Biochemistry*. Springer Berlin, 2016.
- [5] Robert W. Boyd. *Nonlinear Optics*. Elsevier, Acad. Press, 3 edition, 2011.
- [6] Geoffrey New. *Introduction to nonlinear optics*. Cambridge Univ Press, 2014.
- [7] E. Dagotto. Complexity in strongly correlated electronic systems. *Science*, 309(5732):257262, Aug 2005.
- [8] Štefan Višňovský. *Optics in magnetic multilayers and nanostructures*. CRC Press, 2006.
- [9] Andrei Tokmakoff. Mit department of chemistry notes 2009 - 11. nonlinear spectroscopy.
- [10] Jin Au Kong. *Electromagnetic wave theory*. Wiley, 2 edition, 1990.
- [11] Bahaa E. A. Saleh and Malvin Carl. Teich. *Fundamentals of photonics*. Wiley-Interscience, 3 edition, 2009.
- [12] Wikimedia. [https://upload.wikimedia.org/wikipedia/commons/b/ba/John\\_Kerr\\_%28physicist%29.jpg](https://upload.wikimedia.org/wikipedia/commons/b/ba/John_Kerr_%28physicist%29.jpg). Accessed: 14.07.17.
- [13] Jon Ander Arregi, Patricia Riego, and Andreas Berger. What is the longitudinal magneto-optical kerr effect? *Journal of Physics D: Applied Physics*, 50(3), Sep 2016.



- 
- [14] Rohit P. Prasankumar and Antoinette J. Taylor. *Optical techniques for solid-state materials characterization*. CRC Press/Taylor & Francis Group, 2012.
- [15] Richard H. Pantell and Harold E. Puthoff. *Fundamentals of quantum electronics*. Wiley, 1969.
- [16] Paul N. Butcher and David Cotter. *The elements of nonlinear optics*. Cambridge Univ. Press, 1990.
- [17] L. D. Ziegler, R. Fan, A. E. Desrosiers, and N. F. Scherer. Femtosecond polarization spectroscopy: A density matrix description. *The Journal of Chemical Physics*, 100(3):18231839, 1994.
- [18] Christian W. Freudiger, Maarten B. J. Roeffaers, Xu Zhang, Brian G. Saar, Wei Min, and X. Sunney Xie. Optical heterodyne-detected raman-induced kerr effect (ohd-rike) microscopy. *The Journal of Physical Chemistry B*, 115(18):55745581, Dec 2011.
- [19] Nicolaas Bloembergen. *Nonlinear optics: a lecture note and reprint series*. W. A. Benjamin, Inc., 1977.
- [20] William D. Callister and David G. Rethwisch. *Materials science and engineering: SI version*. Wiley, 9 edition, 2015.
- [21] Yayoi Takamura, Erik Folven, Jonathan B. R. Shu, Karl R. Lukes, Binzhi Li, Andreas Scholl, Anthony T. Young, Scott T. Retterer, Thomas Tybell, Jostein K. Grepstad, and et al. Spin-flop coupling and exchange bias in embedded complex oxide micromagnets. *Physical Review Letters*, 111(10), Mar 2013.
- [22] Ilie Elian Radu. *Ultrafast Electron, Lattice and Spin Dynamics on Rare-Earth Metal Surfaces investigated with linear and nonlinear optical techniques*. PhD thesis, 2006.
- [23] Multiphoton nanophotonics - magneto-optics, tutorial 1-15. <http://people.bath.ac.uk/vkv23/English/RechercheT0.htm>. Accessed: 16.08.17.
- [24] Peter M. Oppeneer. Lecture notes: Theory of magneto-optics, uppsala university.
- [25] Ibsen photonics technical note: Signal-to-noise ratio and dynamic range definitions. <https://ibsen.com/wp-content/uploads/Tech-Note-The-Signal-to-Noise-Ratio-SNR-and-Dynamic-Range-DR.pdf>. Accessed: 27.08.17.
- [26] Gerard Giraud, Charles M. Gordon, Ian R. Dunkin, and Klaas Wynne. The effects of anion and cation substitution on the ultrafast solvent dynamics of ionic liquids: A time-resolved optical kerr-effect spectroscopic study. *The Journal of Chemical Physics*, 119(1):464477, 2003.
- [27] D. Mcmorrow, W.t. Lotshaw, and G.a. Kenney-Wallace. Femtosecond optical kerr studies on the origin of the nonlinear responses in simple liquids. *IEEE Journal of Quantum Electronics*, 24(2):443454, 1988.

- 
- [28] refractiveindex.info, water. <https://refractiveindex.info/?shelf=main&book=H2O&page=Hale>. Accessed: 31.07.17.
- [29] Kamila Mazur. *Ultrafast Dynamics of Water in Aqueous Solutions Studied Through Ultrafast Optical Kerr Effect*. PhD thesis, 2011.
- [30] Dale Mcmorrow and William T. Lotshaw. Intermolecular dynamics in acetonitrile probed with femtosecond fourier-transform raman spectroscopy. *The Journal of Physical Chemistry*, 95(25):1039510406, 1991.
- [31] Ping Yuan, Zongju Xia, Y.h. Zou, Ling Quiu, Jifeng Shen, Yuquan Shen, and Huijun Xu. Ultrafast optical kerr effect of phthalocyanine. *Chemical Physics Letters*, 224(1-2):101105, 1994.
- [32] Øystein Johannes Bergsagel. Ultrafast spectroscopic studies of ferroelectric batio<sub>3</sub> thin-films on srtio<sub>3</sub>. *Norwegian University of Science and Technology, Department of Electronics and Telecommunications*, 2016.
- [33] D. A. Allwood, Gang Xiong, M. D. Cooke, and R. P. Cowburn. Magneto-optical kerr effect analysis of magnetic nanostructures. *Journal of Physics D: Applied Physics*, 36, Sep 2003.
- [34] I Razdolski, A Alekhin, U Martens, D Brstel, D Diesing, M Mnzenberg, U Boven-siepen, and A Melnikov. Analysis of the time-resolved magneto-optical kerr effect for ultrafast magnetization dynamics in ferromagnetic thin films. *Journal of Physics: Condensed Matter*, 29(17):174002, 2017.
- [35] *Solstice, One-Box Ultrafast Amplifier System User's Manual*. Spectra-Physics.
- [36] David S. Kliger and James W. Lewis. *Polarized Light in Optics and Spectroscopy*. Elsevier Science, 2012.
- [37] *MODEL SR830 DSP Lock-In Amplifier User's Manual*. Stanford Research Systems, 2011.
- [38] Rp photonics encyclopedia - bandwidth. <https://www.rp-photonics.com/bandwidth.html>. Accessed: 27.08.17.
- [39] C. S. Goncalves, A. S. Silva, D. Navas, M. Miranda, F. Silva, H. Crespo, and D. S. Schmool. A dual-colour architecture for pump-probe spectroscopy of ultrafast magnetization dynamics in the sub-10-femtosecond range. *Scientific Reports*, 6(1), 2016.
- [40] David K. Cheng. *Field and wave electromagnetics*. Pearson Education Limited, 2 edition, 2014.

---

---

---

---

# Appendices



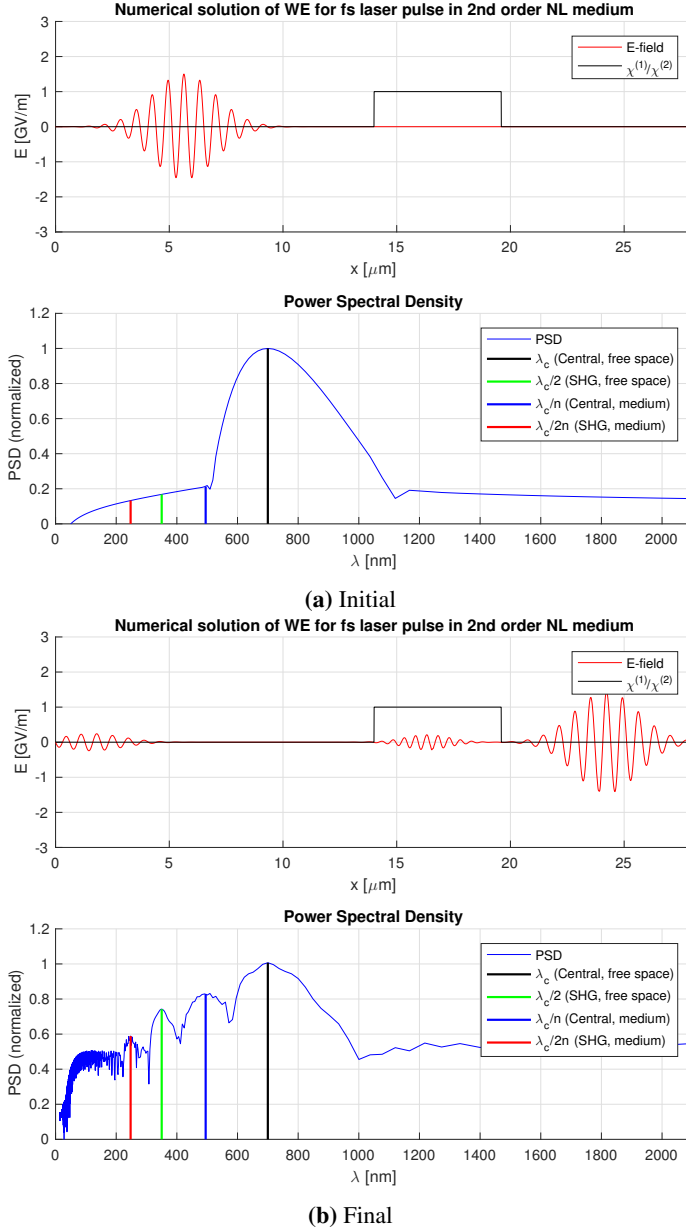
## Numerical Solution of the Nonlinear Wave Equation

Figure A.1 shows the result of a MATLAB script that was written to solve the nonlinear wave equation. Figure A.1a shows the initial electric field as a femtosecond Gaussian wave-packet, with a central wavelength of  $\lambda_c = 700$  nm. The medium has  $\chi^{(1)} = 1$  and  $\chi^{(2)} = 1 \times 10^{-12}$  (third-order susceptibility is not included).

Figure A.1b shows the wave after some time (enough for the wave to propagate through the medium). The green line in the power spectral density shows a component at 350 nm which originates in  $\chi^{(2)}$ . The blue and red lines show components at  $\lambda_c/n$  and  $\lambda_c/2n$  respectively, from residual fields within the medium due to reflection. A component can be seen at  $\lambda = 0$  due to optical rectification. The strength of this component is weak because most of the wave-packet has left the medium, and unlike the second-harmonic, the DC-component can not follow the beam in free space (DC fields do not propagate).

The nonlinear wave equation was solved using the Crank-Nicolson method and the 1st Born approximation. The CLF condition was applied for numerical stability. The figure is intended to illustrate how some fundamental nonlinear properties arise directly from the nonlinear wave equation, and may contain numerical errors.





**Figure A.1:** Solution of the nonlinear wave equation, based on the Crank-Nicolson method (central time, central space) and the 1st Born approximation, with the CLF condition for numerical stability. The initial electric field is a femtosecond Gaussian wave-packet with central frequency  $\lambda_c = 700$  nm. A second-harmonic component at  $\lambda_c/2$  can be seen in the final power spectral density, due to the nonlinear interaction. Additional component arise at  $\lambda_c/n$  and  $\lambda_c/2n$  due to residual reflected light within the medium, and a component arises at  $\lambda = 0$  due to optical rectification (although this is rather weak because the majority of the wave has left the medium). The figure is only indented for illustrative purposes, and may contain numerical errors.

## The Density Matrix

This appendix introduces the notion of the density matrix, which enables transitions between the quantum mechanical formalism and the equations of motion associated with a particular experiment. While the density matrix approach is entirely equivalent to the more familiar treatment of state vectors, it offers advantages when treating systems with *mixed states* rather than pure states, i.e. when all members of an ensemble of atoms occupy more than one quantum state. The theory closely follows the first few chapters of Pantell and Putoff [15].

We initially consider an unperturbed system, for which there exists a set of states  $|\Phi_k\rangle$  that are solutions to the Schrödinger equation with the unperturbed Hamiltonian

$$\hat{H}_0 |\Phi_k\rangle = i\hbar \frac{\partial |\Phi_k\rangle}{\partial t} \quad (\text{B.1})$$

where the subscript  $k$  denotes the quantum state. The states  $|\Phi_k\rangle$  can be expressed in terms of a complete set of time-independent orthonormal states  $|u_k\rangle$  that satisfy the time-independent Schrödinger equation

$$\hat{H}_0 |u_k\rangle = E |u_k\rangle. \quad (\text{B.2})$$

(B.1) then has solutions on the form

$$|\Phi_k\rangle = a_k(t) |u_k\rangle. \quad (\text{B.3})$$

Inserting (B.3) into (B.1) yields

$$\hat{H}_0 |\Phi_k\rangle = a_k(t) \hat{H}_0 |u_k\rangle = i\hbar \frac{\partial a_k}{\partial t} |u_k\rangle \quad (\text{B.4})$$

and by substituting (B.2) for  $\hat{H}_0 |u_k\rangle$  we get

$$\frac{\partial a_k}{\partial t} = -\frac{i}{\hbar} E_k a_k(t) \quad (\text{B.5})$$

which has solutions

---


$$a_k(t) = a_k(0)e^{-i\omega_k t} \quad (\text{B.6})$$

where  $\omega_k = E_k/\hbar$ . It follows that  $|\Phi_k\rangle$  has solutions (ignoring the arbitrary phase factor)

$$|\Phi_k\rangle = e^{-i\omega_k t} |u_k\rangle. \quad (\text{B.7})$$

The system may be in a state that is not an eigenstate, but a linear combination of eigenstates  $|\psi\rangle$ ;

$$|\psi\rangle = \sum_k c_k |\Phi_k\rangle = \sum_k c_k e^{-i\omega_k t} |u_k\rangle \quad (\text{B.8})$$

where  $|c_k|^2$  is the probability of finding the system in state  $k$ . When the system is unperturbed, the expansion coefficients  $c_k$  are independent of time, and the sum of all coefficients squared adds up to unity, because the system must be in one of its eigenstates upon measurement.

The product of a bra and a ket  $\langle u|v\rangle$ , termed the inner product, is a scalar. However, the product of a ket and a bra  $|u\rangle\langle v|$ , termed the outer product, is an operator, and may be expanded in terms of the set of operators  $|u_i\rangle\langle u_j|$

$$\hat{A} = \sum_{ij} A_{ij} |u_i\rangle\langle u_j| \quad (\text{B.9})$$

where  $A_{ij}$  are elements of a 2nd rank tensor that correspond to

$$A_{ij} = \langle u_i|\hat{A}|u_j\rangle. \quad (\text{B.10})$$

Since operators that correspond to observables are Hermitian, the complex conjugate of an element in the operator matrix is  $A_{ij} = A_{ji}^*$ .

The state described by  $|\psi\rangle$  may be considered a pure state. The coefficients  $c_k$  that describe the probability distribution in terms of its eigenstates did not arise from lack of knowledge of the system, but rather from the nature of the quantum mechanical measurement process. If we consider a system of two groups of harmonic oscillators, the states describing each group is

$$|\psi_a(t_0)\rangle = \sum_k a_k |u_k\rangle \quad (\text{B.11})$$

$$|\psi_b(t_0)\rangle = \sum_k b_k |u_k\rangle \quad (\text{B.12})$$

where  $|\psi_a(t_0)\rangle$  is the state vector for one group and  $|\psi_b(t_0)\rangle$  is the state vector for the other. The expectation values for an operator are then given by

$$\langle A_a \rangle = \langle \psi_a(t_0)|\hat{A}|\psi_a(t_0)\rangle \quad (\text{B.13})$$

$$\langle A_b \rangle = \langle \psi_b(t_0)|\hat{A}|\psi_b(t_0)\rangle. \quad (\text{B.14})$$

---

This can be considered a mixed state. A particle may be in either of the two states  $|\psi_a\rangle$  and  $|\psi_b\rangle$ , and statistical analysis must be applied to evaluate the probabilities of measuring either state. If  $N_a$  oscillators in state  $|\psi_a(t_0)\rangle$  are mixed with  $N_b$  oscillators in state  $|\psi_b(t_0)\rangle$ , the expectation value for an operator for the mixed state is

$$\langle A \rangle = p_a \langle \psi_a(t_0) | \hat{A} | \psi_a(t_0) \rangle + p_b \langle \psi_b(t_0) | \hat{A} | \psi_b(t_0) \rangle \quad (\text{B.15})$$

provided the groups do not interact with each other. The probability coefficients  $p_a = N_a/(N_a + N_b)$  and  $p_b = N_b/(N_a + N_b)$  are the probabilities that the system is characterized by  $|\psi_a\rangle$  and  $|\psi_b\rangle$  respectively. The expectation value for the entire system is then

$$\langle A \rangle = \sum_n p_n \langle \psi_n | \hat{A} | \psi_n \rangle. \quad (\text{B.16})$$

Inserting the diagonal elements of (B.10), i.e.  $i = j = k$ , (B.16) can be rewritten as

$$\langle A \rangle = \sum_{n,k} p_n \langle \psi_n | \hat{A} | u_k \rangle \langle u_k | \psi_n \rangle \quad (\text{B.17})$$

$$= \sum_{n,k} p_n \langle u_k | \psi_n \rangle \langle \psi_n | \hat{A} | u_k \rangle \quad (\text{B.18})$$

$$= \sum_k \langle u_k | \rho \hat{A} | u_k \rangle \quad (\text{B.19})$$

where

$$\rho \equiv \sum_n p_n |\psi_n\rangle \langle \psi_n| \quad (\text{B.20})$$

is the density operator, or the density matrix.

The density matrix has the following properties:

1. The expectation value of an operator  $\hat{A}$  is found by the *trace* of the matrix product of the density matrix and the operator

$$\langle A \rangle = \text{Tr}(\hat{A}\rho) \quad (\text{B.21})$$

The trace is the sum of diagonal elements, i.e.

$$\langle A \rangle = \sum_{n,m} A_{mn} \rho_{nm}. \quad (\text{B.22})$$

2. The density matrix evolves in time according to

$$i\hbar \frac{\partial \rho}{\partial t} = [\hat{H}, \rho] \quad (\text{B.23})$$

where the right-hand side denotes the commutator of the Hamiltonian and the density matrix.

---

3. The density matrix is Hermitian

$$\rho_{ij} = \rho_{ji}^*. \quad (\text{B.24})$$

4. The density matrix is normalized

$$\text{Tr}(\rho) = 1. \quad (\text{B.25})$$

# Lorentz Model of Magneto-Optical Interactions

This appendix provides a classical derivation of the permittivity tensor for a magnetized medium, based on the Lorenz force equation. The derivation was motivated by the apparent lack of a detailed introduction to magneto-optics in most literature. Instead, the dielectric tensor for a magnetized medium is often presented as the basis for the magneto-optical effects. This appendix is based on the exercise suggested Jin Kong in [10], and may be prone to errors. A classical treatment of magneto-optics is ultimately inadequate<sup>1</sup>, as magneto-optics is strongly connected to both quantum mechanical and relativistic effects. It is nevertheless possible to derive a qualitative model, which provides a certain degree of intuition for the directional dependence of the interaction process. It is assumed throughout this appendix that materials are both optically and magnetically isotropic.

We initially consider a single electron in a static magnetic field

$$\mathbf{B}(t) = \mathbf{B}_0$$

driven by a time-harmonic electric field

$$\mathbf{E}(t) = \tilde{\mathbf{E}}_0 e^{-i\omega t}$$

where the spatial dependence is contracted in the amplitude, denoted by the tilde sign. The velocity of the electron is time-harmonic, with frequency  $\omega$

$$\mathbf{v}(t) = \tilde{\mathbf{v}}_0 e^{-i\omega t}.$$

The equation of motion for the electron is the Lorenz force equation

$$\mathbf{F} = m \frac{d\mathbf{v}}{dt} = q\mathbf{E} + q\mathbf{v} \times \mathbf{B}. \tag{C.1}$$

---

<sup>1</sup>The classical model is e.g. not adequate to predict any material-specific properties. These generally require consideration of the spin density of states and crystalline symmetry properties.

---

The time-dependence can be factored out to obtain

$$-i\omega m \tilde{\mathbf{v}}_0 = q \tilde{\mathbf{E}}_0 + q \tilde{\mathbf{v}}_0 \times \mathbf{B}_0 \quad (\text{C.2})$$

(C.2) can be dot-multiplied by  $\mathbf{B}_0$  to obtain

$$-i\omega m \mathbf{B}_0 \cdot \tilde{\mathbf{v}}_0 = q \mathbf{B}_0 \cdot \tilde{\mathbf{E}}_0 + q \mathbf{B}_0 \cdot (\tilde{\mathbf{v}}_0 \times \mathbf{B}_0) \quad (\text{C.3})$$

where the last term is found to be zero by the vector identity  $\mathbf{A} \cdot (\mathbf{B} \times \mathbf{C}) = \mathbf{B} \cdot (\mathbf{C} \times \mathbf{A})$  (the scalar triple product);

$$\mathbf{B}_0 \cdot (\tilde{\mathbf{v}}_0 \times \mathbf{B}_0) = \tilde{\mathbf{v}}_0 \cdot (\mathbf{B}_0 \times \mathbf{B}_0) = 0. \quad (\text{C.4})$$

The result is therefore

$$\boxed{\mathbf{B}_0 \cdot \tilde{\mathbf{v}}_0 = \frac{-q}{i\omega m} \mathbf{B}_0 \cdot \tilde{\mathbf{E}}_0.} \quad (\text{C.5})$$

(C.2) can be cross-multiplied by  $\mathbf{B}_0$  from the left to obtain

$$-i\omega m \mathbf{B}_0 \times \tilde{\mathbf{v}}_0 = q \mathbf{B}_0 \times \tilde{\mathbf{E}}_0 + q \mathbf{B}_0 \times (\tilde{\mathbf{v}}_0 \times \mathbf{B}_0). \quad (\text{C.6})$$

(C.6) is simplified by the vector identity  $\mathbf{A} \times (\mathbf{B} \times \mathbf{C}) = (\mathbf{A} \cdot \mathbf{C})\mathbf{B} - (\mathbf{A} \cdot \mathbf{B})\mathbf{C}$  (the vector triple product);

$$-i\omega m \mathbf{B}_0 \times \tilde{\mathbf{v}}_0 = q \mathbf{B}_0 \times \tilde{\mathbf{E}}_0 + q(\mathbf{B}_0 \cdot \mathbf{B}_0)\tilde{\mathbf{v}}_0 - q(\mathbf{B}_0 \cdot \tilde{\mathbf{v}}_0)\mathbf{B}_0. \quad (\text{C.7})$$

Inserting (C.5) for  $\mathbf{B}_0 \cdot \tilde{\mathbf{v}}_0$  in (C.7) yields

$$-i\omega m \left( \frac{i\omega m}{q} \tilde{\mathbf{v}}_0 + \tilde{\mathbf{E}}_0 \right) = q \mathbf{B}_0 \times \tilde{\mathbf{E}}_0 + q(\mathbf{B}_0 \cdot \mathbf{B}_0)\tilde{\mathbf{v}}_0 - q \left( \frac{-q}{i\omega m} \mathbf{B}_0 \cdot \tilde{\mathbf{E}}_0 \right) \mathbf{B}_0. \quad (\text{C.8})$$

(C.8) can be rearranged to get the terms containing  $\tilde{\mathbf{v}}_0$  on the left-hand side and the terms containing  $\tilde{\mathbf{E}}_0$  on the right-hand side. Multiplying the equation by  $\frac{q^2}{m^2}$  yields

$$\left( \omega^2 - \frac{q^2}{m^2} (\mathbf{B}_0 \cdot \mathbf{B}_0) \right) q \tilde{\mathbf{v}}_0 = \frac{q^3}{m^2} \mathbf{B}_0 \times \tilde{\mathbf{E}}_0 - i \frac{1}{\omega} \left( \frac{q^4}{m^3} \mathbf{B}_0 \cdot \tilde{\mathbf{E}}_0 \right) \mathbf{B}_0 + i\omega \frac{q^2}{m} \tilde{\mathbf{E}}_0. \quad (\text{C.9})$$

The electron current density is readily obtained by multiplying (C.9) by the electron number density  $N$  (number of electrons per  $\text{m}^3$ ) and the charge of a single electron  $q$ ;  $\mathbf{J}_b = Nq\mathbf{v}_0$ . The notation can be simplified by introducing the cyclotron frequency

$$\omega_c = \frac{q}{m} B_0 \quad (\text{C.10})$$

and the plasma frequency

$$\omega_p = \sqrt{\frac{Nq^2}{m\epsilon_0}}. \quad (\text{C.11})$$

(C.9) then simplifies to

$$(\omega^2 - \omega_c^2) Nq\tilde{\mathbf{v}}_0 = -i\omega\epsilon_0 \left[ i\frac{\omega_p^2}{\omega}\boldsymbol{\omega}_c \times \tilde{\mathbf{E}}_0 + \frac{\omega_p^2}{\omega^2}\boldsymbol{\omega}_c (\boldsymbol{\omega}_c \cdot \tilde{\mathbf{E}}_0) - \omega_p^2\tilde{\mathbf{E}}_0 \right] \quad (\text{C.12})$$

which yields an expression for the current density

$$\begin{aligned} \tilde{\mathbf{J}}_b &= Nq\tilde{\mathbf{v}}_0 \\ &= -i\omega\epsilon_0 \left[ i\frac{\omega_p^2}{\omega(\omega^2 - \omega_c^2)}\boldsymbol{\omega}_c \times \tilde{\mathbf{E}}_0 \right. \\ &\quad \left. + \frac{\omega_p^2}{\omega^2(\omega^2 - \omega_c^2)}\boldsymbol{\omega}_c (\boldsymbol{\omega}_c \cdot \tilde{\mathbf{E}}_0) \right. \\ &\quad \left. - \frac{\omega_p^2}{(\omega^2 - \omega_c^2)}\tilde{\mathbf{E}}_0 \right]. \end{aligned} \quad (\text{C.13})$$

The subscript  $b$  in  $\tilde{\mathbf{J}}_b$  indicates that the current density corresponds to a bound current, as opposed to a free current  $\mathbf{J}_f$ . The total current density is  $\mathbf{J} = \mathbf{J}_f + \mathbf{J}_b$ , and Ampere's law can be expressed in terms of  $\mathbf{E}$  and  $\mathbf{B}$  as

$$\nabla \times \mathbf{B} = \mu_0\mathbf{J}_f + \mu_0\mathbf{J}_b + \mu_0\epsilon_0 \frac{d\mathbf{E}}{dt}. \quad (\text{C.14})$$

The charge density is similarly expressed as  $\rho = \rho_f + \rho_b$ , and Gauss' law takes on the form

$$\nabla \cdot \mathbf{E} = \frac{1}{\epsilon_0}\rho_f + \frac{1}{\epsilon_0}\rho_b. \quad (\text{C.15})$$

Electrical charge is a conserved quantity, and any change in the total charge density  $\rho$  with respect to time must be accompanied by a divergence in the total current density  $\mathbf{J}$

$$\frac{d\rho}{dt} = -\nabla \cdot \mathbf{J} \quad (\text{C.16})$$

(where the negative sign appears because current flow and electron flow are inversely defined). Separating the free and bound contributions yields

$$\frac{d\rho_f}{dt} = -\nabla \cdot \mathbf{J}_f \quad (\text{C.17})$$

$$\frac{d\rho_b}{dt} = -\nabla \cdot \mathbf{J}_b. \quad (\text{C.18})$$

Note that (C.17) and (C.18) could have been derived by taking the divergence of (C.14) and inserting (C.15) for  $\nabla \cdot \mathbf{E}$  and comparing the free and bound terms of the charge and current densities.

If the time-harmonic electric field is removed, (C.2) reduces to



---


$$m \frac{d\mathbf{v}}{dt} = q\mathbf{v} \times \mathbf{B} \quad (\text{C.19})$$

indicating that the Lorentz force always acts perpendicular to the velocity. In this case, the electrons take on circular orbits with orbital radius

$$r = \frac{mv}{qB} \quad (\text{C.20})$$

and rotational angular frequency

$$\omega_c = \frac{v}{r} = \frac{q}{m} B \quad (\text{C.21})$$

which is the cyclotron frequency. The circulating electrons form closed loops of bound currents, which can be described by the magnetization vector [40]

$$\mathbf{M} = \lim_{\Delta v \rightarrow 0} \frac{\sum_{k=1}^{n\Delta v} \mathbf{m}_k}{\Delta v} \quad (\text{C.22})$$

where the magnetic dipole moments  $\mathbf{m}_k$  arise from individual electrons moving in closed loops such that

$$\mathbf{m} = IS\hat{\mathbf{a}} \quad (\text{C.23})$$

where  $I$  is the current carried by the loop and  $S$  is the area of the loop. This contribution to the current density can be seen by separating the bound current density into two contributions, one from the electrical dipoles and one from the magnetic dipoles, such that

$$\mathbf{J}_b = \mathbf{J}_p + \mathbf{J}_m \quad (\text{C.24})$$

$$\mathbf{J}_b = \frac{d\mathbf{P}}{dt} + \nabla \times \mathbf{M} \quad (\text{C.25})$$

where the last relation can be found by taking the curl of (C.14).

For a ferromagnetic material, the magnetic susceptibility depends on the history of the applied  $\mathbf{H}$  field. This causes the static  $\mathbf{B}$  field introduced in (C.2) to never completely vanish, since even in the absence of  $\mathbf{H}$ , the magnetic flux density is still  $\mathbf{B} = \mu_0 \mathbf{M}_r$  where  $\mathbf{M}_r$  is the remanence field. Similarly, when  $\mathbf{B}$  is sufficiently strong, the magnetization saturates, and the magnetization is unaffected by further increase in the externally applied field strength. The static  $\mathbf{B}$  is therefore limited by the material hysteresis properties. In paramagnetic and diamagnetic materials, the net magnetization tends to vanish, because the magnetic ordering is low.

By separating out the free charge density, Gauss' law can be expressed in terms of the  $\mathbf{D}$  field

$$\nabla \cdot \mathbf{D} = \rho_f. \quad (\text{C.26})$$

(C.26) can be differentiated with time to obtain

$$\nabla \cdot \frac{d\mathbf{D}}{dt} = \frac{d\rho_f}{dt} = -\nabla \cdot \mathbf{J}_f \quad (\text{C.27})$$

which yields

$$\boxed{i\omega\nabla \cdot \tilde{\mathbf{D}}_0 = \nabla \cdot \tilde{\mathbf{J}}_f.} \quad (\text{C.28})$$

Taking the divergence of (C.14) yields

$$\nabla \cdot \mathbf{J}_f + \nabla \cdot \mathbf{J}_b + \epsilon_0 \nabla \cdot \frac{d\mathbf{E}}{dt} = 0. \quad (\text{C.29})$$

Factoring out the time-dependence and inserting (C.28) into (C.29) gives

$$\nabla \cdot (i\omega\tilde{\mathbf{D}}_0) = \nabla \cdot (i\omega\epsilon_0\tilde{\mathbf{E}}_0 - \tilde{\mathbf{J}}_b) \quad (\text{C.30})$$

i.e.,

$$i\omega\tilde{\mathbf{D}}_0 = i\omega\epsilon_0\tilde{\mathbf{E}}_0 - \tilde{\mathbf{J}}_b. \quad (\text{C.31})$$

Inserting (C.13) for  $\tilde{\mathbf{J}}_b$  gives

$$\tilde{\mathbf{D}}_0 = \epsilon_0\tilde{\mathbf{E}}_0 + \epsilon_0\hat{O}_{MO}\tilde{\mathbf{E}}_0 = \epsilon_0(1 + \hat{O}_{MO})\tilde{\mathbf{E}}_0 \quad (\text{C.32})$$

such that

$$\boxed{\begin{aligned} \tilde{\mathbf{D}}_0 &= \epsilon\tilde{\mathbf{E}}_0 \\ \epsilon &= \epsilon_0(1 + \hat{O}_{MO}) \end{aligned}} \quad (\text{C.33})$$

where an operator  $\hat{O}_{MO}$  has been defined to account for the magneto-optical interaction. The magneto-optical interaction operator is defined as

$$\boxed{\hat{O}_{MO} = i\frac{\omega_p^2}{\omega(\omega^2 - \omega_c^2)}\boldsymbol{\omega}_c \times + \frac{\omega_p^2}{\omega^2(\omega^2 - \omega_c^2)}\boldsymbol{\omega}_c\boldsymbol{\omega}_c \cdot - \frac{\omega_p^2}{(\omega^2 - \omega_c^2)}} \quad (\text{C.34})$$

Note that the operator is dimensionless, such that  $\hat{O}_{MO}\tilde{\mathbf{E}}_0$  has the same units as  $\tilde{\mathbf{E}}_0$ . The necessity to define epsilon in terms of an operator arises from the dot and cross products with the electric field.

We can gain some confidence in the result by observing that in the limit  $\mathbf{B}_0 = 0$ , i.e.  $\boldsymbol{\omega}_c = 0$ , the operator is reduced to

$$\hat{O}_{MO} = -\frac{\omega_p^2}{\omega^2} \quad (\text{C.35})$$

and the traditional (non-magnetic) result for  $\epsilon$  is restored;

$$\epsilon = \epsilon_0 \left( 1 - \frac{\omega_p^2}{\omega^2} \right). \quad (\text{C.36})$$

The permittivity can be expressed on tensor form as

---


$$\begin{bmatrix} D_x \\ D_y \\ D_z \end{bmatrix} = \begin{bmatrix} \epsilon_{xx} & \epsilon_{xy} & \epsilon_{xz} \\ \epsilon_{yx} & \epsilon_{yy} & \epsilon_{yz} \\ \epsilon_{zx} & \epsilon_{zy} & \epsilon_{zz} \end{bmatrix} \begin{bmatrix} E_x \\ E_y \\ E_z \end{bmatrix}. \quad (\text{C.37})$$

The elements of the tensor depends on the direction and strength of the magnetic flux density. If  $\mathbf{B}$  is aligned along the z-direction, and  $\mathbf{E}$  has an arbitrary polarization, (C.33) can be written fully out as

$$\begin{aligned} \begin{bmatrix} D_x \\ D_y \\ D_z \end{bmatrix} &= \epsilon_0 \begin{bmatrix} E_x \\ E_y \\ E_z \end{bmatrix} + i\epsilon_0 \frac{\omega_c \omega_p^2}{\omega(\omega^2 - \omega_c^2)} \begin{bmatrix} -E_y \\ E_x \\ 0 \end{bmatrix} \\ &+ \epsilon_0 \frac{\omega_c^2 \omega_p^2}{\omega^2(\omega^2 - \omega_c^2)} \begin{bmatrix} 0 \\ 0 \\ E_z \end{bmatrix} - \epsilon_0 \frac{\omega_p^2}{(\omega^2 - \omega_c^2)} \begin{bmatrix} E_x \\ E_y \\ E_z \end{bmatrix} \end{aligned} \quad (\text{C.38})$$

which can be represented in a matrix form as

$$\begin{aligned} \epsilon_{M_z} &= \begin{bmatrix} \epsilon_1 & \epsilon_3 & 0 \\ -\epsilon_3 & \epsilon_1 & 0 \\ 0 & 0 & \epsilon_2 \end{bmatrix} \\ \epsilon_1 &= \epsilon_0 \left( 1 - \frac{\omega_p^2}{\omega^2 - \omega_c^2} \right) \\ \epsilon_2 &= \epsilon_0 \left( 1 - \frac{\omega_p^2}{\omega^2} \right) \\ \epsilon_3 &= \epsilon_0 \left( \frac{-i\omega_p^2}{\omega(\omega^2 - \omega_c^2)} \omega_c \right). \end{aligned} \quad (\text{C.39})$$

Similarly, if  $\mathbf{B}$  is aligned along the x-direction, the tensor takes on the form

$$\epsilon_{M_x} = \begin{bmatrix} \epsilon_2 & 0 & 0 \\ 0 & \epsilon_1 & \epsilon_3 \\ 0 & -\epsilon_3 & \epsilon_1 \end{bmatrix} \quad (\text{C.40})$$

and along the y-direction

$$\epsilon_{M_y} = \begin{bmatrix} \epsilon_1 & 0 & -\epsilon_3 \\ 0 & \epsilon_2 & 0 \\ \epsilon_3 & 0 & \epsilon_1 \end{bmatrix} \quad (\text{C.41})$$

where the expressions for  $\epsilon_1$ ,  $\epsilon_2$  and  $\epsilon_3$  remains unchanged. Since (C.34) is linear, the general form of  $\epsilon$  with arbitrary direction of magnetization is simply  $\epsilon_{M_x} + \epsilon_{M_y} + \epsilon_{M_z}$ ;

$$\epsilon_{MO} = \begin{bmatrix} \epsilon_{xx} & \epsilon_{xy} & -\epsilon_{xz} \\ -\epsilon_{xy} & \epsilon_{xx} & \epsilon_{yz} \\ \epsilon_{xz} & -\epsilon_{yz} & \epsilon_{xx} \end{bmatrix} \quad (\text{C.42})$$


---

---

where  $\epsilon_{xx} = 2\epsilon_1 + \epsilon_2$ .